MODELING ORGANIC REACTIVITY AND PHOTOPHYSICAL PROCESSES: DFT APPLICATIONS OF AZA-HETEROCYCLIC COMPOUNDS AND ORGANIC SENSITIZERS

by

Esma Birsen Boydaş

B.S., Integrated BS&MS Program in Teaching Chemistry, Boğaziçi University, 2016

Submitted to the Institute for Graduate Studies in
Science and Engineering in partial fulfillment of
the requirements for the degree of
Master of Science

Graduate Program in Chemistry
Boğaziçi University
2018

ACKNOWLEDGEMENTS

It has been almost four years since I first received a key to the CCBG lab, and became part of a journey full of sweat, tears (yes) and mostly joy. Hands down I have had the most wonderful supervisor, who did her best to support, encourage and inspire me to succeed. All thanks to her, we are finally seeing the light at the end of the tunnel. I owe Assoc. Prof. Saron Catak, a big, big debt of gratitude for everything.

It has been an honour and pleasure for me to be a student of Prof. Viktorya Aviyente, and I would like to thank her for guidance and encouragement in my master studies.

I would like to thank the members of my committee, Prof. İlknur Doğan and Prof. Alimet Özen for their valuable advices and comments. Also, I am grateful for the very pleasant and peaceful environment during my defense seminar.

I am profoundly grateful to Prof. Veronique Van Speybroeck from Universiteit Gent, for allowing me a part of Center for Molecular Modeling as a Visiting Researcher. I acknowledge Prof. Antonio Monari from University of Lorraine, for his advices and scientific guidance during my visits in Theory-Modeling-Simulation Lab in Nancy.

I acknowledge the TÜBİTAK graduate scholarship for the project 115Z863, and TÜBİTAK ULAKBİM High Performance Computing Center for computational resources.

Many special thanks go to all the former and current members of the Computational Chemistry and Biochemistry Research Group (CCBG) for their friendship. Gamze Tanrıver, you have truly been my rescuer, and biggest support throughout my master's. KB 313B is definitely not the same without you. Semiha Kevser Bali, you are my beet, bear and battlestar galactica. Thank you for making my life easier.

Dr. Dietmar Hertsen, without doubt you are a unique person, whom I enjoyed working with. Thank you for answering at least 3000 of my questions. I sincerely wish you the best, and I am positive that you will be excellent at anything you do.

I would like to thank my best friend, and the second-best team captain of Bogazici University Women's Volleyball Team, Hazal Tuğçe Şenol, for being my four leaf clover. May pineapple pizza be our one and only disagreement in life. I would also like to thank my roommate, and the third-best team captain of Bogazici University Women's Volleyball Team, Berna Özdemir from Sivas district, for being my anti social butterfly. You are hard to find, but lucky to have.

Needless to say, I am much beholden to my family for supporting me sentimentally throughout writing this thesis and my life in general.

ABSTRACT

MODELING ORGANIC REACTIVITY AND PHOTOPHYSICAL PROCESSES: DFT APPLICATIONS OF AZA-HETEROCYCLIC COMPOUNDS AND ORGANIC SENSITIZERS

This study is composed of two main components, involving Density Functional Theory investigations in terms of small organic reactions and organic dye-semiconductor systems.

In the first part, ring-expansion reactions of 1-azoniabicyclo[n.1.0]alkanes have been modeled to endeavor the mechanistic aspects of two competitive pathways. Several nucleophiles and their regioselectivity are scrutinized in terms of different level of theories and solvation methods. As starting bicyclic structures, 1-azoniabicyclo[3.1.0] hexane and 1-azoniabicyclo[4.1.0]heptane ions have been used, while the computational work of the latter has been done the first time in the literature.

In the second part, the aim of the study was to probe the effective modeling of isolated sensitizers and dye@semiconductor interfaces in Dye-sensitized Solar Cells (DSSCs). Density functional theory (DFT) and Time-Dependent Density functional theory (TDDFT) calculations have been performed to elucidate the absorption and charge transfer in sensitizers and dye-to-semiconductor electron injection process. Density of states (DOS) have been analyzed by means of two main approaches: i) single dye@SC model, ii) dye@SC model with periodic boundary conditions. In addition to periodicity, effects of solvation, inclusion of non-covalent interactions and different DFT functionals have been tested within the framework of organic dyes.

ÖZET

ORGANIK REAKTİVİTE VE FOTOFİZİKSEL ÖZELLİKLERİN MODELLENMESİ: AZA-HETEROSİKLİK BİLEŞİKLER VE ORGANİK BOYALAR ÜZERİNE DFT UYGULAMALARI

İki bölümden oluşan bu çalışmada, Yoğunluk fonksiyoneli teorisi kullanılarak küçük organik reaksiyonlar, organik boyalar ve titanyum dioksit yarı iletken sistemleri incelendi.

İlk bölümde, 1-azoniabisiklo[n.1.0]alkan sistemlerinin halka genişleme tepkimeleri incelendi. Bu çalışmada, literatürdeki deneysel çalışmalarda bulunan nükleofiller kullanılarak, bu nükleofillerin bölgesel seçicilik özellikleri analiz edildi ve çalışmada farklı çözücü modellerine yer verilerek bu modeller karşılaştırmalı olarak tetkik edildi.

İkinci bölümde, boyaya duyarlı güneş pillerindeki bağımsız boya, ve boya-yarı iletken arayüzünün hesapsal modellenmesi üzerine çalışıldı. Yoğunluk Fonksiyoneli Teorisi (DFT) ve Zaman bağımlı Yoğunluk Fonksiyoneli Teorisi (TDDFT) hesaplamaları yapılarak, güneş pillerindeki ilk basamak olan absorpsiyon ve yük transferi incelendi. Elektronik durum yoğunluğu ele alınırken iki ayrı yaklaşım kullanıldı. Bunlar i) tekil boya@yarı iletken yüzeyi, ii) periyodik hesaplamalar olarak belirlendi. Hesaplamalarda aynı zamanda çözücü etkisi, dispersiyon düzeltmeleri, ve farklı DFT fonksiyonelleri de test edilerek rapor edildi.

TABLE OF CONTENTS

LIST OF FIGURES

LIST OF TABLES

LIST OF SYMBOLS

$E^{\ddagger}$	Electronic activation energy
$E_c[\rho]$	Correlation energy
E_F	Fermi energy
$E_x[\rho]$	Exchange energy
H	Hamiltonian operator
$J[\rho]$	Coulomb energy
J_{sc}	Short circuit current
P_0	Ground state matrix
P_x	Excited state matrix
$T[\rho]$	Kinetic energy of interacting electrons
$V_{ext}(r)$	External potential
V_{KS}	Kohn-Sham potential
V_{oc}	Open circuit potential
V_{xc}	Exchange-correlation potential
ΔE_{dist}	Distortion energy
ΔE_{int}	Interaction energy
ΔE_x	Becke's gradient correction
$\Delta G^{\ddagger}$	Gibbs free energy of activation
ΔG_{rxn}	Gibbs free energy of reaction
$\Delta G_{solvation}$	Solvation free energy
Γ	Detachment density matrix
Λ	Attachment density matrix
$\rho(r)$	Electron density
ϕ_s	Quantitative topological descriptor
Ψ	Many electron wavefunction

LIST OF ACRONYMS/ABBREVIATIONS

ADF	Amsterdam Density Functional
ASM	Activation-Strain model
B3LYP	Becke-3-parameter Lee-Yang-Par functional
BMK	Boese-Martin for kinetics
CAM-B3LYP	Coulomb attenuated method
CB	Conduction band
C-PCM	Conductor-like polarizable continuum model
COSMO	Conductor-like screening model
DFT	Density functional theory
DOS	Density of states
DSSC	Dye sensitized solar cell
EDG	Electron donating group
EWG	Electron withdrawing group
FMO	Frontier molecular orbital
FWHM	Full width at half maximum
GGA	Generalized gradient approximation
GTO	Gaussian type orbital
HF	Hartree-Fock theory
HOMO	Highest occupied molecular orbital
IEF-PCM	Integral equation formalism polarizable continuum model
IRC	Intrinsic reaction coordinate
LDA	Local density approximation
LUMO	Lowest unoccupied molecular orbital
M06-2X	Hybrid meta exchange-correlation functional
NTO	Natural transition orbitals
PBC	Periodic boundary conditions
PBE	Perdew-Burke-Ernzerhof functional
PCM	Polarizable Continuum Model

PDOS	Projected density of states
SC	Semi conductor
SCF	Self consistent field
STO	Slater type orbital
TD-DFT	Time dependent density functional theory
TS	Transition state
VASP	Vienna Ab Initio Simulation Package

1. INTRODUCTION

Computational chemistry principally deals with computation of molecular electronic structures and properties of chemical reactions, within a numerical method appropriately well advanced that it can be automated for utilization on a computer. By virtue of designed mathematical methods, very few elements of chemistry can be computed exactly, but nearly every aspect of chemistry can be described in a qualitative or approximate scheme.

The biggest misconception about computational chemistry is to expect any computed number to be exact. Even though the exact application of the theoretical methods is not usually possible, a qualitative computation and estimation can give useful insight into the chemical problem. In addition to the basic physical processes concerning energy storage, corrosion and phase changes, molecular modeling also consists of simulations to identify active sites on a protein molecule that are most likely to interact with a new drug molecule.

The motivation behind the desire to develop a practical method of applying quantum mechanics to complex systems resulted in Density Functional Theory. Although its origins were in physics, the applications are now broadened to chemistry, biology and minerology. The founding father of DFT, Walter Kohn, was awarded with a Nobel Prize in Chemistry in 1998, and the applications of DF calculations had begun to increase exponentially ever since.

This thesis employs the most widely used quantum mechanical method, Density Functional Theory (DFT), and encapsulates distinctive subfields namely, organic reactions and photophysical processes in organic dyes. The first chapter of this work consists of a mechanistic study of ring-opening reactions of bicyclic aziridinium ions. Bicyclic aziridinium ions are obtained by a nucleophilic attack of the ring nitrogen to an electron-deficient carbon and the removal of an appropriate leaving group.

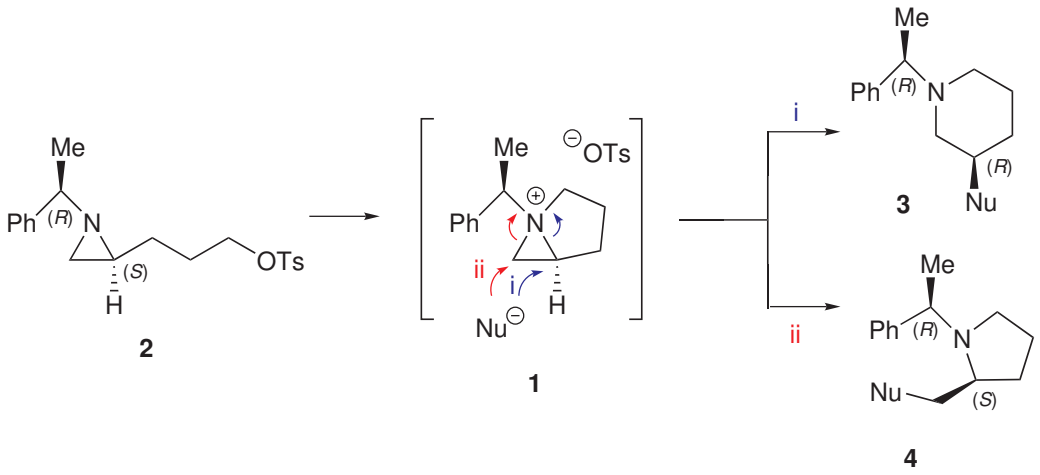

Figure 1.1. Schematic representation of the first reaction mechanism studied in Part I.

Preparation of 1-azoniabicyclo[3.1.0]hexane tosylate is shown in Figure 1.1. After the bicyclic intermediate 1 is formed, two different products piperidine-derivatives 3 and pyrrolidines-derivatives 4 are obtained depending on the attack site preferred by the applied nucleophile. If more hindered path i is preferred, piperidine product is formed. Less hindered path ii leads to pyrrolidine product. This nucleophilic substitution is studied experimentally by Ji *et al.* [1].

Another similar reaction mechanism was proposed by Choi *et al.* [2]. In this work, 1-azoniabicyclo[4.1.0]heptane tosylate was succesfully synthesized in a stable form. The ring-expansion of this bicyclic intermediate again yielded two different products: piperidines 7 and azepanes 8, as shown in Figure 1.2.

In the first part of this thesis, regioselectivity in ring-expansion reactions of bicyclic aziridinium ions is investigated. The results of this work have been published in Organic & Biomolecular Chemistry, early in this year [3]. A thorough analysis of transition state structures have been established, by means of activation-strain model and bond elongation percentages. The effects of solvation have been taken into account by both implicit and explicit solvent environment, and comparatively analyzed.

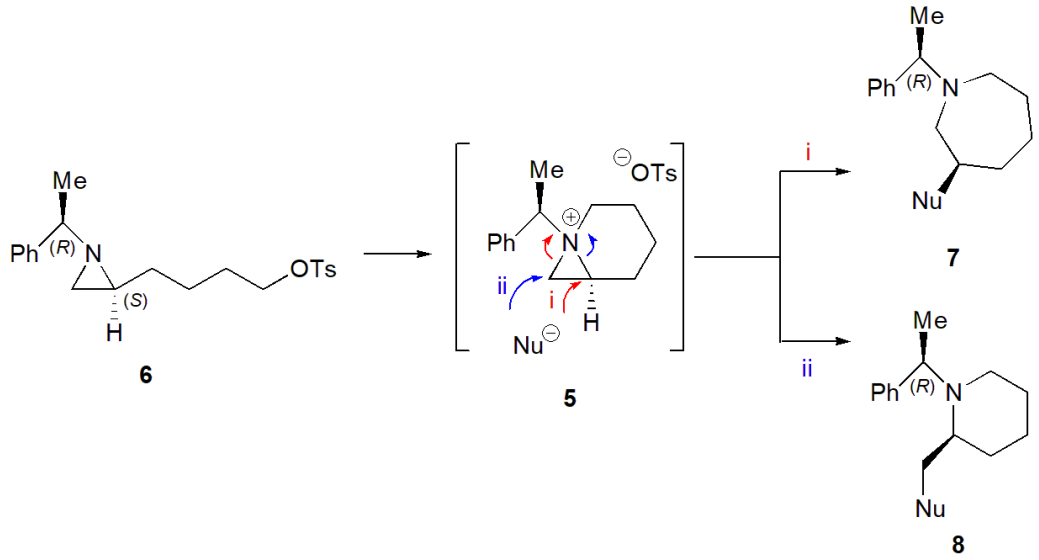

Figure 1.2. Schematic representation of the second reaction mechanism studied in Part I.

In the second part, two recently synthesized organic dyes in Dye-sensitized Solar Cells have been probed, to achieve a deeper theoretical understanding upon cell mechanism. These organic dyes are shown in Figure 1.3 [4]. Initially, a thorough analysis has been performed on isolated dye molecules. Absorption spectra of the dyes have been reproduced by TD-DFT level of theory. Natural Transition Orbitals have been produced and scrutinized. A study on isolated dye molecules has been published in Theoretical Chemistry Accounts, in 2017 [5]. In addition to the investigations on stand-alone dye molecules, the dyes have been anchored onto the titanium dioxide (101) surface, to model the electronic coupling between the dye and semiconductor.

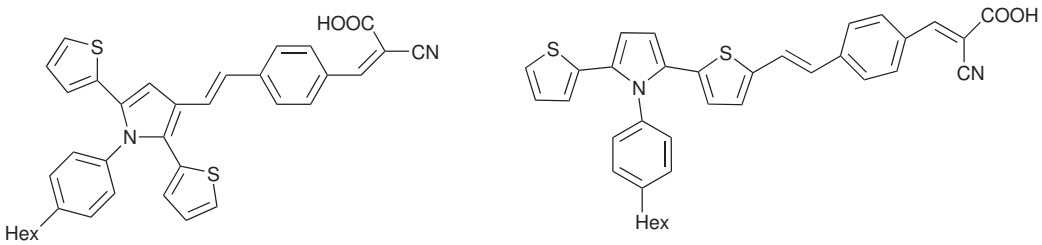

Figure 1.3. Structures of organic dyes studied in Part II [4].

The applications of Density Functional Theory to chemical problems have become crucial. In addition to rationalizing practical observations in synthetic organic chemistry, extensive studies of DFT are needed to thrive the predictive power of theoretical calculations. Being spread over different subfields, this work is intended to depict the potential scope and applications of DFT.

2. METHODOLOGY

2.1. Theoretical Background

The primary concern of quantum chemistry is the behavior of electrons under the electromagnetic field that stems from nuclear charges. In contrast to classical mechanics which renders the systems by specifying the positions and velocities, quantum mechanics habituates a complex mathematical vector called the wave function to represent physical systems. In theory, the quantum mechanical wavefunction contains all the information about a given system. All properties of a system can be described by the Schrödinger equation, which especially plays a paramount role in physics:

$$H\psi = E\psi \tag{2.1}$$

where H represents Hamiltonian operator, E denotes the total energy of the system and ψ corresponds to the wave function which predicts emprically and accurately the probability of events or the outcome. The Hamiltonian operator consists of all potential and kinetic energy terms:

$$H = -\sum_I \frac{\hbar^2}{2m_I}\nabla_I^2 - \sum_i \frac{\hbar^2}{2m_e}\nabla_i^2 - \sum_i \sum_I \frac{e^2 Z_I}{r_{iI}} + \sum_{i<j} \frac{e^2}{r_{ij}} + \sum_{I<J} \frac{e^2 Z_I Z_J}{r_{IJ}} \tag{2.2}$$

where the first and second term represent the kinetic energy of the nuclei and electrons, respectively. The potential energies arise from Coulomb interactions of nucleus-electron (U_{Ii}), electron-electron (U_{ij}), and nucleus-nucleus (U_{IJ}) are also represented as shown in Equation 2.2.

Named after its founding fathers, Max Born and Robert Oppenheimer, the Born-Oppenheimer (BO) approximation seperates the motion of the nuclei and the motion of the electrons within an atom. Due to the fact that the mass of atomic nucleus is much larger than the electrons, the acceleration of the electrons will be much larger.

Consecutively, electrons are much more responsive to forces around them, while the nuclei are not. Thus, the positions of nuclei can be considered as "frozen" and the terms connected with nuclei can be eliminated. As a result, Hamiltonian operator becomes:

$$H_{el} = E_I^{kin} + U_{Ii} + U_{ij} \tag{2.3}$$

The Schrödinger equation with respect to Born-Oppenheimer approximation is thus defined as,

$$(H_{el} + V_{nn})\psi_{el} = E_{el}\psi_{el} \tag{2.4}$$

where V_{nn} is the nuclear-nuclear repulsion energy constant, and the eigenvalue E_{el} is called the electronic energy.

Schrödinger's equation points out the wave-like properties of matter and it is considered as one of the greatest achievements of 20^{th} century. It can identify nearly all properties of systems, however it is tremendously complicated to solve. The exact solution can only be obtained for a few systems, like particle in a box, the hydrogen atom and the hydrogen molecule ion. For the solution of all the other systems, the variational method can be used. In Equation 2.1, multiplying both sides by ψ gives:

$$\psi H \psi = \psi E \psi \tag{2.5}$$

For many electron systems, integration of both sides in a volume ($d\tau$) yields:

$$E = \frac{\int \psi H \psi d\tau}{\int \psi^2 d\tau} \tag{2.6}$$

When the Hamiltonian operator is exact, energy calculated from Equation 2.6 will also be exact. In Hamiltonian term, each interaction term decreases the energy. Once an approximate energy is obtained, the calculation will be repeated by modifying the

Hamiltonian. The determination of the energy value close to the exact one comprises a minimization step of calculated energy. This principle is called variational method which is considered to be one of the most useful tools for finding approximate solutions for the Schrödinger equation.

Presently, Density Functional Theory is considered as the most proficient and promising approach to compute the electronic structure of matter. As stated before this thesis is composed of two different chapters, and DFT is utilized in both parts.

2.2. Density Functional Theory

The foundations of Density Functional Theory are laid on Hohenberg-Kohn Existence Theorem, which proposes that Hamiltonian of a system can be formed if the density of the corresponding system is known, and thus Schrödinger equation can be solved to obtain energy. According to Hohenberg and Kohn, the potential of the nuclei is the only external potential V(r) affecting the electrons of the system, and this potential is determined by the electron density ρ(r):

$$\rho(r) : N \int ... \int |\Psi(r_1, r_2, ...r_n)|^2 dr_1 dr_2 ... dr_n \tag{2.7}$$

where r_{i} represents coordinates of the electrons. The real electron density is evaluated variationally, as it is done in Molecular Orbital Theory. According to Hohenberg-Kohn Variational Theorem, any electron density other than real one, will give rise to a higher energy than the ground state energy. The ground state electronic energy is a function of electron density function, which implies the "functional" part of DFT, and is represented as:

$$E[\rho(r)] = \int V(r)\rho(r)dr + T[\rho(r)] + V_{ee}[\rho(r)] \tag{2.8}$$

To make use of Equation 2.8, Kohn and Sham presented the concept of a reference system of noninteracting electrons. Thus, the electronic energy can be rewritten as:

$$E[\rho(r)] = \int V(r)\rho(r)d(r) + T_{ni}[\rho(r)] + J[\rho(r)] + E_{xc}[\rho(r)] \tag{2.9}$$

with J[ρ] denoting the coulomb energy, $T_{ni}[\rho]$ being the kinetic energy of the non-interacting electrons and $E_{xc}[\rho]$ referring to the exchange-correlation energy functional. The exchange-correlation functional is designated as the sum of an exchange functional $E_X[\rho]$ and a correlation functional $E_C[\rho]$, although it contains also a kinetic energy term arising from the kinetic energy difference between the interacting and non-interacting electron systems. The kinetic energy term, being the measure of the freedom, and exchange-correlation energy, describing the change of opposite spin electrons (defining extra freedom to an electron), are the favorable energy contributions. The Coulomb energy term describes the unfavorable electron-electron repulsion energy and therefore disfavors the total electronic energy.

The wavefunctions of this system can be depicted as a Slater determinant of one-elecron functions, thus the electron density can be represented as:

$$\rho(r) = \sum_{i=1}^{N} < \chi_i|\chi_i > \tag{2.10}$$

Kohn-Sham orbitals are established by solving the Kohn-Sham equations.

$$h_i^{KS}\chi_i = \varepsilon_i\chi_i \tag{2.11}$$

where the Kohn-Sham Hamiltonian $\hbar_i$, is defined as:

$$h_i^{KS} = -\frac{\nabla^2}{2} - \sum_{k}^{M} \frac{Z_k}{|r_i - r_k|} + \int \frac{\rho(r)}{r_{ij}}dr + V_{xc} \tag{2.12}$$

In Equation 2.12, V_{xc} is the exchange-correlation potential and is related to exchange correlation energy by:

$$V_{xc} = \frac{\delta E_{xc}}{\delta \rho} \tag{2.13}$$

where V_{xc} is divided into two parts: an exchange functional and a correlation functional:

$$E_{xc}[\rho] = E_x[\rho] + E_c[\rho] \tag{2.14}$$

The exchange term is related to the interactions between the electrons of same spin, whereas the correlation term is associated with the interactions between the electrons of opposite spin. The exchange-correlation energy is the only unknown term in Equation 2.9.

2.3. Functionals

The shortfall of DFT is that, the exact functionals for exchange-correlation term are not known apart from free electron gas. The reason why there are so many different DFT methods is that, there are many ways to approximate the exchange-correlation term. One of the many methods to determine the unknown E_{XC} is the Local Density Approximation (LDA). According to LDA, the electron density of a system is assumed to be same in each site, as a uniform electron gas. However, the constant value of the electron density is not in agreement with the rapid variation of densities in a molecule. To overcome this issue, Generalized gradient approximation (GGA) methods [6] take into account the nonhomogenous nature of the electron density, by postulating the exchange and correlation energies dependent on density gradient, as can be seen in Equation 2.15:

$$E_{xc}^{GGA}[n] = \int drn(r)\epsilon_{xc}(n(r), |\nabla n(r)|) \tag{2.15}$$

Hybrid density functional methods are alternative approaches that combine GGA method with a percentage of exact functionals. The most well-known example of hybrid density functional is B3LYP [7], which consists of a mixture of LDA and GGA functionals taken from DFT and HF methods as illustrated;

$$E_{xc}^{B3LYP} = (1-a)E_x^{LSDA} + aE_x^{HF} + b\Delta E_x^B + (1-c)E_c^{LSDA} + cE_c^{LYP} \tag{2.16}$$

where a, b and c parameters were determined to be 0.20, 0.72 and 0.81, respectively.

CAM-B3LYP [8] is another example of hybrid exchange-correlation functional, which unites the hybrid features of B3LYP and long-range correction exhibited by Tawada *et al.* It emerges in applications where B3LYP is not successful, such as the polarizability of long-chains, excitations using TDDFT etc. CAM-B3LYP functional consists of 0.19 of HF and 0.81 B88 exchange interaction at its short-range, and 0.65 HF and 0.35 B88 at its long-range.

Another important functional is M06-2X [9], which is a member of Minnesota Functional family developed by the group of Prof. Donald Truhlar. The hybrid-exchange correlation can be written as follows:

$$E_{xc}^{hyb} = \frac{X}{100}E_x^{HF} + (1 - \frac{X}{100})E_x^{DFT} + E_c^{DFT} \tag{2.17}$$

in which X denotes the percentage of Hartree-Fock exchange, and it equals to 54 in the case of M06-2X functional.

2.4. Time Dependent Density Functional Theory

Time Dependent Density Functional Theory (TD-DFT) is a computational tool for the calculation of electronic excited states. The Hamiltonian operator can be expressed as:

$$\widehat{H} = \widehat{T}(r) + \widehat{W}(r) + \widehat{V}_{ext}(r,t) \tag{2.18}$$

In this equation, the foremost term corresponds to the kinetic energy of the electrons, the second one depicts the Coulomb interactions between the electrons, and the third term designates the effect of time-dependent potential on electrons. The excited state energy depends on the external potential. In this manner, it is essential to know the effects of the potential in order to calculate excited state properties.

The Hohenberg-Kohn Theorem is applied a variational principle involving the action:

$$A = \int_{t_0}^{t_1} \langle \Psi(t) | i\frac{\partial}{\partial_t} - \widehat{H} | \Psi(t) \rangle dt \tag{2.19}$$

and the wavefunction is determined up to a time-dependent constant:

$$\Psi(r_1, ..., r_N, t) = \Psi[\rho](t) e^{-ia(t)} \tag{2.20}$$

The phase factor adds a constant to the action in Equation 2.20:

$$A[\rho] = \int_{t_0}^{t_1} \langle \Psi(t) | i\frac{\partial}{\partial_t} - \widehat{H}(t) | \tilde{\Psi}[\rho](t) \rangle dt + a(t_1) - a(t_0) = A[\rho] + const. \tag{2.21}$$

And A[ρ] can be written as:

$$A[\rho] = B[\rho] - \int dr \int_{t_0}^{t_1} (r,t)\rho(r,t) dtv \tag{2.22}$$

where B[ρ] is independent of the external potential. Assume an independent system which has the property described as shown below:

$$\rho(r,t) = \sum_i f_i |\Psi(r,t)|^2 \tag{2.23}$$

Hence to rewrite B[ρ]:

$$B[\rho] = \Sigma_i f_i \int_{t_0}^{t_1} \langle \Psi_i(t) | i\tfrac{\partial}{\partial_t} - \tfrac{1}{2}\nabla_i^2 | \Psi_i(t) \rangle dtv - \tfrac{1}{2} \int_{t_0}^{t_1} dt \iint dr_1 dr_2 \tfrac{\rho(r_1,t)\rho(r_1,t)}{|r_1 - r_2|} - A_{xc}[\rho] \tag{2.24}$$

where $A_{xc}[\rho]$ is the exchange and correlation action functional. Applying the variational principle to (2.22) with constraint gives:

$$\rho(r,t) = \sum_i f_i |\Psi_i(r,t)|^2 = \sum_i^N |\Psi_i(r,t)|^2 \tag{2.25}$$

Time-dependent Kohn-Sham equation is thus obtained:

$$[-\frac{1}{2}\nabla^2 + v_{eff}(r,t)]\Psi_i(r,t) = i\frac{\partial}{\partial_t}\Psi_i(r,t) \tag{2.26}$$

$$v_{eff}(r,t) = v_H(r,t) + v_{xc}(r,t) + v_{ext}(r,t) \tag{2.27}$$

and the unknown is now the time-dependent exchange potential, and all exchange and correlation effects in TD-DFT are collected in 2.26:

$$v_{xc}(r,t) = \frac{\delta A_{xc}[\rho]}{\delta\rho(r,t)} \tag{2.28}$$

Time dependent density functional theory equations are exact, there is no approximations present in the methodolody. However, since the exchange correlation functional is not known, approximations should be introduced.

The adiabadic approximation (AA) is shown in Equation 2.29:

$$v_{xc}[\rho](r,t) = \frac{\delta A_{xc}[\rho]}{\delta\rho(r,t)} \approx \frac{\delta E_{xc}[\rho]}{\delta\rho(r)}|_{\rho=\rho(r,t)} \tag{2.29}$$

If the electron densities change, the exchange and correlation potential change instantaneously.

2.5. Basis Sets

A basis set consists of a set of functions to describe the orbitals within a system. Basis functions are usually expanded as a linear combination of atomic orbitals (LCAO), with varying coefficients.

$$\phi_i = \sum_{\mu=1}^{K} c_{\mu i} f_\mu \tag{2.30}$$

where the functions μ_i represents molecular orbitals, f_μ for atomic orbitals, $c_{\mu i}$ are coefficients and K is the total number of atomic orbital functions, which are also basis functions.

These basis sets can be divided into two groups, Slater-type Orbitals (STOs) and Gaussian-type orbitals (GTOs). The former is the solution to Schrödinger equation for hydrogen-atoms. When the computational expense is taken into account, increasing number of required integrals exponentially decreases the speed of a computation. Gaussian type orbitals (GTOs) are the approximated versions of STOs.

In a minimal basis set, one basis function (STO or GTO) is present for each atomic orbital in the atom, and thus, all orbitals are regarded as to have the same shape. Since this is not realistic, double-zeta and triple-zeta basis sets are constructed. However, when the molecule gets bigger, it becomes very costly to calculate a double-zeta for every orbital. In an effort to reduce computational cost, Pople developed split-valence basis set method. In this approach, only one basis function is used for each core, and a larger basis for the valence atomic orbitals. Given the fact that the core electrons are affected by the chemical environment to a lesser extent than valence electrons, inner shell electrons are treated with a minimal basis set whereas valence electrons are treated with a larger basis set. The notation of a split valence basis set is A-BCd [10], in which A represents the number of primitive Gaussians incorporating each core atomic basis function. B and C represents the valence orbitals consisting of two basis functions for each.

In order to obtain a better approximation and get closer to exact electronic energy, polarization functions are used in basis sets. Polarization functions account for the fact that orbitals share qualities of each other and not necessarily have the traits of one type of angular momentum. An s orbital can polarize in one direction if it is mixed with a p orbital. One asterisk (*) sign at the end of a basis set or (d) indicates that polarization has been taken into account in p orbitals. For hydrogen atoms, double asterisk ** or (d,p) is used to denote the polarization functions.

In addition to polarization, diffuse functions can also be added to get a better description for larger orbital occupancies. It is necessary for anions and very electronegative atoms with a high electron density. Diffuse functions in a basis set are represented by a +. One + sign indicates that diffuse functions are added only to p orbitals, while ++ means they are added to s orbitals as well.

The more complex basis sets yield more accurate solutions to Schrödinger's equation. However, computational expense also increases with accurate calculations. Thus, the choice of proper functionals and basis sets is substantial. Basis sets should be selected in conformity with the desired level of accuracy with reasonable computational cost.

2.6. Solvation Models

2.6.1. Continuum Solvation Models

Continuum solvation is a method to represent the solvent environment as polarizable medium characterized by a static dielectric constant, and the solute is placed in a cavity circumvented by this dielectric medium. The total solvation free energy can be denoted as:

$$\Delta G_{solvation} = \Delta G_{cavity} + \Delta G_{dispersion} + \Delta G_{electrostatic} + \Delta G_{repulsion} \tag{2.31}$$

in which $\Delta G_{solvation}$ is the penalty in energy, when the solute is placed in the medium. Dispersion interactions between the solute and solvent are expressed as $\Delta G_{dispersion}$, which is favorable and stabilizing. The electrostatic component of the solute-solvent interaction energy is $\Delta G_{electrostatic}$. $\Delta G_{repulsion}$ is the exchange solute-solvent interactions not included in the cavitation energy.

The main drawback of continuum solvent models is the electrostatic problem described by the general Poisson equation:

$$-\vec{\nabla}[\epsilon(\vec{r})\nabla\vec{V}(\vec{r})] = 4\pi\rho_M(\vec{r}) \tag{2.32}$$

simplified to

$$-\nabla^2 V(\vec{r}) = 4\pi\rho_M(\vec{r}) \text{ within C} \tag{2.33}$$

$$-\epsilon\nabla^2 V(\vec{r}) = 0 \text{ outside C} \tag{2.34}$$

where C is the section of space occupied by cavity, ϵ is the dielectric function, V corresponds to the total quantity of electrostatic potential generated by the charge distribution ρ_M. The reaction potential V(r) generated by the polarization of the dielectric medium:

$$V(\vec{r}) = V_M(\vec{r}) + V_R(\vec{r}) \tag{2.35}$$

The Polarizable Continuum Model (PCM) belongs to the class of polarizable continuum solvation models [11]. In this model, the solute is placed in a cavity defined by a set of spheres centered on atoms, having radii defined by the van der Waals radius of the atoms multiplied by a predefined factor (generally around 1.2). The cavity surface is then subdivided into small domains (tesserae), in which the polarization charges are placed. There are many different approaches to carry out PCM calculations. The origi-

nal method is called Dielectric PCM (D-PCM), the second model is the Conductor-like PCM (C-PCM), in which the surrounding medium is modeled as a conductor instead of dielectric, and the third one is an implementation whereby the PCM equations are recast in an integral equation formalism (IEF-PCM). Both IEF-PCM and C-PCM methods are used in this thesis.

2.6.2. Explicit Solvation Models

In explicitly solvated systems, all the atomic and molecular details of solvent are taken into account by means of including individual solvent molecules. A schematic representation of explicit and implicit solvation models is shown in Figure 2.1. By courtesy of adding discrete solvent molecules around solute species, significant interactions such as hydrogen bonding can also be defined. This method is useful when modeling organic reactions. The major drawback when using explicit solvation in the calculations is the proliferating computation time due to increasing number of atoms in the system.

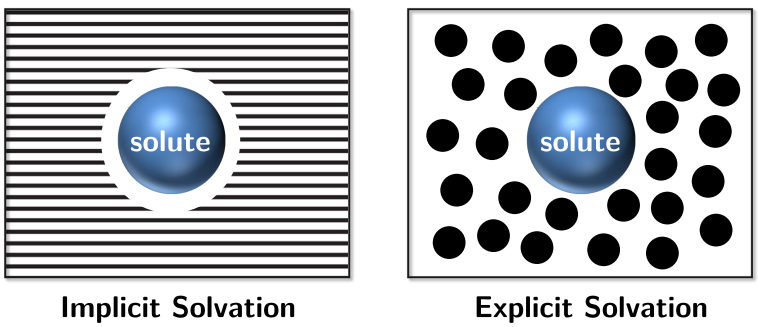

Figure 2.1. Representation of implicit and explicit solvation models.

2.7. ϕ_s Index

ϕ_s index [12] is a quantum mechanical descriptor of light-induced electronic charge density variation. It is a very straightforward way to describe charge transport occuring upon light-absorption. This index has been used in the second part of this thesis, when a depiction of charge transfer nature is needed.

ϕ_s index is obtained via an analysis of density matrices. The difference between the ground state matrix P_0 and excited state density matrix P_X is taken, and a difference density matrix Δ is obtained, as shown:

$$\Delta = P_X - P_0 \Rightarrow \sum_{k=1}^{K} (\Delta S)_{kk} = 0 \tag{2.36}$$

ΔS equals to zero, due to the fact that no electron gain or loss is present in the system. After a unitary similarity transformation is performed on Δ, the diagonal matrix δ is obtained:

$$\exists U | \delta = U^{\dagger} \Delta U; \quad (\delta)_{ij} = 0 \quad \forall i \neq j \tag{2.37}$$

Subsequently, the diagonal matrix is divided into two arrays according to their signs. The resultant diagonal matrices are backtransformed to obtain the Detachment Γ and Attachment Λ density matrices [13]. The detachment represents the deficiency of electron density that stems from light absorption. Attachment indicates the increase in electron density at excited state. They are expressed in the space of K atomic orbitals. Due to the fact that no electron is lost during the vertical excitation, one can see that:

$$\sum_{\mu=1}^{K} (\Gamma S)_{\mu\mu} = \sum_{\mu=1}^{K} (\Lambda S)_{\mu\mu} \tag{2.38}$$

Nonetheless, related detachment/attachment densities can be defined in 3D space. Spatial arrangement of the electronic density removed (detachment) from the ground state and rearranged (attachment) in the excited state during transition represented by equations below, in which detached/attached charge can be defined as:

$$\theta = \int_R d\xi_1 \int_R d\xi_2 \int_R d\xi_3 \varrho_\tau(\xi_1 \xi_2 \xi_3) \equiv \int_{R^3} d^3 \xi_{\varrho\tau}(\xi) \tag{2.39}$$

$$\tau \equiv \Gamma, \Lambda \tag{2.40}$$

ϕ_s index is dimensionless. As it was previously expressed, it indicates the overlap between the attachment and detachment densities. ϕ_s index can be shown as:

$$\phi_S = \theta^{-1} \int_{R^3} d^3\xi \sqrt{\varrho_\Gamma(\xi)\varrho_\Lambda(\xi)} \tag{2.41}$$

The ϕ_S index, that depends on the charge-transfer character of the electronic transition, ranges from 0 to 1. ϕ_S index can be equal to 0 if there is no intersection between detachment and attachment densities, and equal to 1 in an extreme case, where there is no electronic density variation between ground and excited states. One may consider that a three dimensional integration grid enclosing the sensitizer will connect the detachment/attachment densities over the delimited volume.

2.8. Periodic Boundary Conditions and Planewaves

In a solid-state material, the atoms are arranged in an orderly way. The uniformity of the system can be represented by a repeating 'unit'. This unit can infinitely be repeated in all directions, allowing for the reduction of computational cost. In this sense, Periodic Boundary Conditions (PBC) are taken into account, to model the infinitely sized crystalline solid by using only a small unit cell.

Named after its founding physicist Felix Bloch, a Bloch wave is a class of wavefunction for a system in a periodically-repeating environment. Its wavefunction has the form:

$$\psi(r) = e^{ikr}u(r) \tag{2.42}$$

where r denotes the position, k is the crystal wave vector and u(r) is the periodic function with the same periodicity as a crystal. In another point of view, it is safe to say that if a plane wave is multiplied by a periodic function, the result is a Bloch wave.

According to Bloch's theorem, the energy eigenstates of an electron in a crystal structure can be written as Bloch waves. This statement also governs the concept of

electronic band structure. The Block wave eigenstates are usually represented as Ψ_{nk}, where n is the band index. All distinguished Bloch-waves occur for k-vectors in the first Brillouin zone of the reciprocal lattice.

2.9. The Supercell Approach

Utilizing Bloch's theorem and a plane-wave basis set results in periodic calculations in all (three) dimensions. When calculations in bulk are considered, periodicity is needed in three dimensions. However, when defining a surface, periodicity in one direction needs to be taken out. By accepting the fact that the surface is normal to the z direction, a sufficient amount of vacuum space needs to be introduced, so that periodic copies corresponding to neighboring clones do not interact considerably.

2.10. Density of States

The second part of this thesis mainly employs electronic band structure analysis on dye-sensitized solar cells (DSSCs). Density of states (DOS) information of dye and semiconductor interfaces have been analyzed to describe the electronic coupling of dye LUMO and the conduction band (CB) states of semiconductor.

In solid-state, the array of energy levels that an electron in the solid is allowed to be in, is called "bands". Whereas the array of forbidden energy levels is called "band gap". Bands constitute tightly aligned orbitals. A simple schematic representation for electronic band structure is given in Figure 2.2. In this figure, the Fermi level is also shown, and denoted as E_F, which is defined as the highest energy level that can be occupied at 0 Kelvin.

The density of states (DOS) depicts the number of available states per interval of energy. In this sense, a large value of DOS refers to a high number of available states present for occupation. Conversely, a value of zero DOS indicates no occupancy of states at a given energy level. Density of states are highly far-reaching in theoretical physics, due to its descriptive power in particular energy ranges.

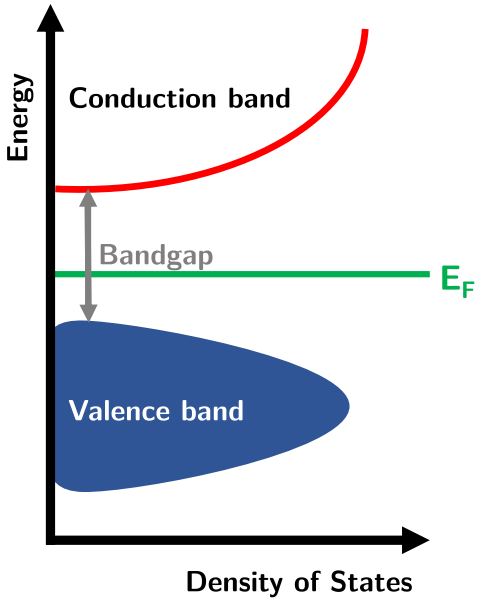

Figure 2.2. A simple graphical representation of electronic band structure.

3. RING-EXPANSIONS OF BICYCLIC AZIRIDINIUM IONS

3.1. Background

The smallest aza-heterocycle rings, aziridines, consist of one amine group (-NH-) and two methylene groups (-CH_2-) [14]. The history of aziridine ring moiety goes a long way back to 1888, when Siegmund Gabriel unintentionally synthesized ethylaziridine [15], as shown in Figure 3.1. After this nitrogen-containing three-membered ring system has been established via different routes, it has been widely used in synthetic organic chemistry ever since, mainly due to its selective synthesis and transformations [16,17].

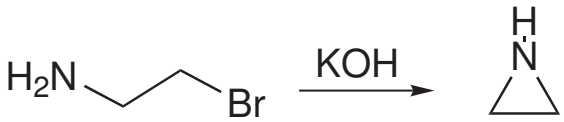

Figure 3.1. Gabriel synthesis of aziridine [15].

Along with Gabriel synthesis, aziridines can be prepared by a variety of different methods. Wenker synthesis is an example, in which a β amino alcohol is converted to an aziridine with the aid of sulfuric acid at high temperatures, as shown in Figure 3.2 [18]. After sulphonate salt is prepared, the base abstracts an amine proton, and deprotonation step results in ring closure.

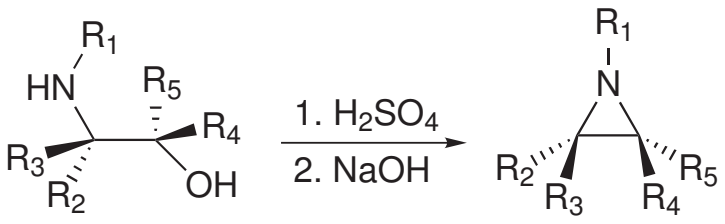

Figure 3.2. Wenker synthesis of aziridine [18].

Another method to obtain aziridine is the De Kimpe Aziridine Synthesis [19]. As can be seen from Figure 3.3, α-haloimines are converted into azaheterocycles by

intermolecular nucleophilic substitution.

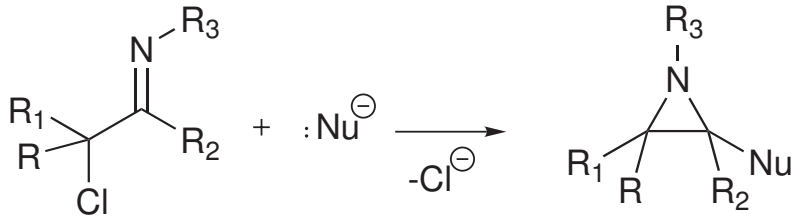

Figure 3.3. De Kimpe synthesis of aziridine [19].

Owing to its 60 degrees of internal angles, aziridine unit has angle and hence, ring strain, and the bonding in its structure has been explained by banana bond model as can be seen in Figure 3.4. The internal angles in three-membered rings are quite different from sp^3 hybridized bond angles, thus, the atoms in the ring customize their hybridization, in order to accommodate the triangular geometry. At the end, the endocyclic bonds gains more p character, as shown in Figure 3.4. Concurrently, on account of increased s character in the nitrogen lone pair, aziridine unit is less basic than acyclic aliphatic amines. In an experimental point of view, spectroscopic measurements via X-ray, nuclear magnetic resonance (NMR), or electron diffraction methods have been employed to detect the geometry and structural stability of ring nitrogen atom. These studies point out that, pyramidal inversion of ring nitrogen in aziridines have substantially higher barrier than open-chain amines.

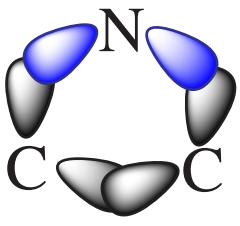

Figure 3.4. Banana bond model.

Substituents on the ring nitrogen atom play a fundamental role in aziridine ring-expansion reactions [20]. If these substituents are electron-withdrawing (EWG), the aziridine unit is called activated aziridine, since it is highly defenseless towards nucleophilic attack. In contrast, bearing an electron-donating group (EDG) at the ring-

nitrogen results in a non-activated aziridine, as shown in Figure 3.5. Non-activated aziridines demand activation during their ring-expansion reactions [21].

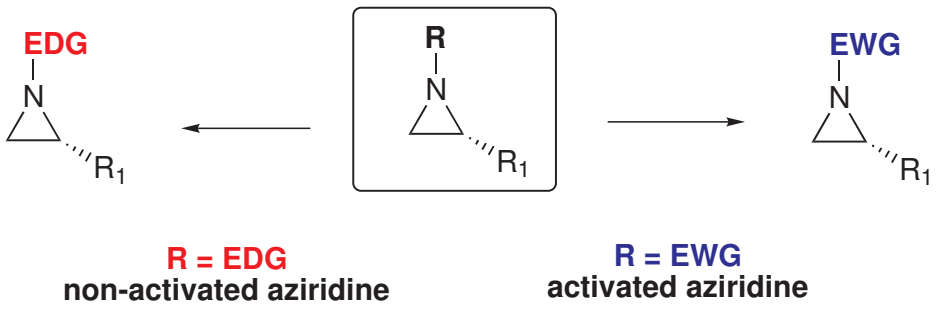

Figure 3.5. Activated and non activated aziridines.

Monocyclic aziridinium ions are obtained by N-alkylation with an alkyl halide. They react with nucleophiles and manifest ring-opening reactions. As shown in Figure 3.6a, an attack on unsubstituted carbon yields α-branched amines, and an attack on substituted carbon renders β-branched amines [22, 23].

Bicyclic aziridinium ions can also be procured, via an intermolecular S_N2 manner and presence of an appropriate leaving group as shown in Figure 3.6b [24,25]. Owing to their high ring strain energy, they tend to experience nucleophilic attack, and yielding azaheterocycles with larger ring size.

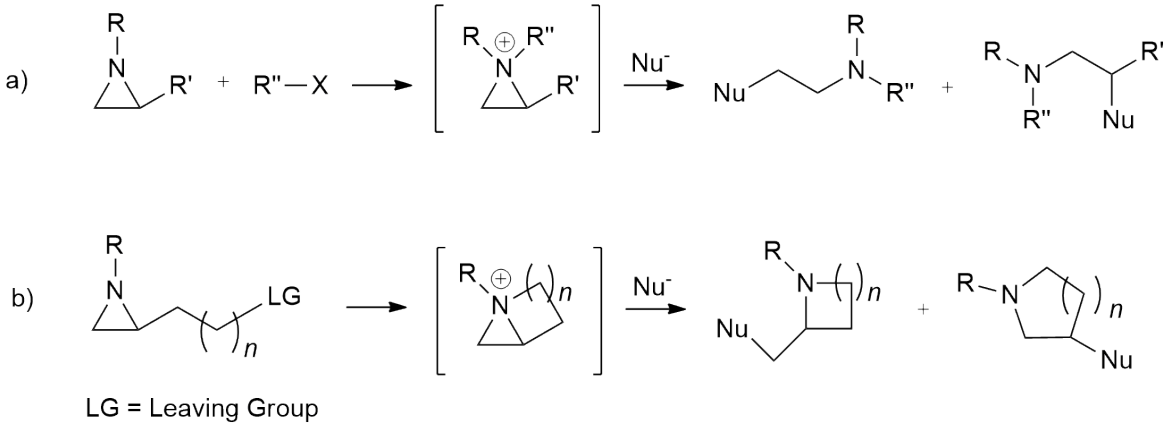

Figure 3.6. Formation of monocyclic (a) and bicyclic (b) aziridinium ions and their ring opening reactions by applied nucleophiles.

The mechanisms studied in this part of the thesis have been shown in Figure 3.7. The experimental results reported for bicyclic aziridinium 1 and 5 is given in Table 3.1. For 1-azoniabicyclo[3.1.0]hexane tosylate 1, the ring-expansion reaction with different nucleophiles yielded either piperidines or pyrrolidines. If the bicyclic aziridinium 1 follows the hindered route path i, piperidine product 3 is formed, and unhindered route path ii results in pyrrolidines 4. According to the results reported by Ha and coworkers, [1] if the applied nucleophile is cyanide, the ring-expansion product formed is exclusively pyrrolidines 4. Azide nucleophile does not show a clear preference over two possible routes, yielding a product ratio of 36:64. The treatment of bicyclic aziridinium 1 with chloride nucleophile merely produces piperidines 3.

Table 3.1. Experimental results for the ring-expansion reactions of 1-azonia bicyclo[3.1.0]hexane tosylate ions 1 and 1-azoniabicyclo[4.1.0]heptane tosylate ions 5 with different nucleophiles in acetonitrile.

Nucleophile	Substrate	T	Yield (%)	**3/4** ratio	**7/8** ratio
nBu$_4$N$^+$CN$^-$	Azirid. **1**	25	89	0:100	-
NaN_3	Azirid. **1**	25	89	36:64	-
TsCl	Azirid. **1**	25	88	100:0	-
NaCN	Azirid. **5**	25	92	-	8:92
NaN_3	Azirid. **5**	25	94	-	59:41
$BnNH_2$	Azirid. **5**	25	87	-	65:35

A similar synthetic work was performed on 1-azoniabicyclo[4.1.0]heptane tosylates 5 and their ring-expansion reactions with various nucleophiles, by Choi *et al.* [2]. This specific reaction resulted in either azepanes 7 or piperidines 8. Overall product ratio is shown in Table 3.1. Cyanide nucleophile prefers to follow hindered attack site, and mainly yields piperidines 8. Azide and amine nucleophiles did now show an observable regioselectivity, and affords 59:41 and 65:35 ratio of products 7/8.

The key elements governing the regioselectivity of nucleophiles are still not fully explored. A theoretical study regarding such reaction of 1-azoniabicyclo[4.1.0]heptane tosylates was not been present in the literature. Although the ring-expansion of bicyclic aziridiniums 1 were also investigated theoretically [1], further analysis have been done on the transition states in the current study, to also incorporate dispersion corrections in the calculations, which are known to be influential in terms of modeling small organic reactions [26, 27].

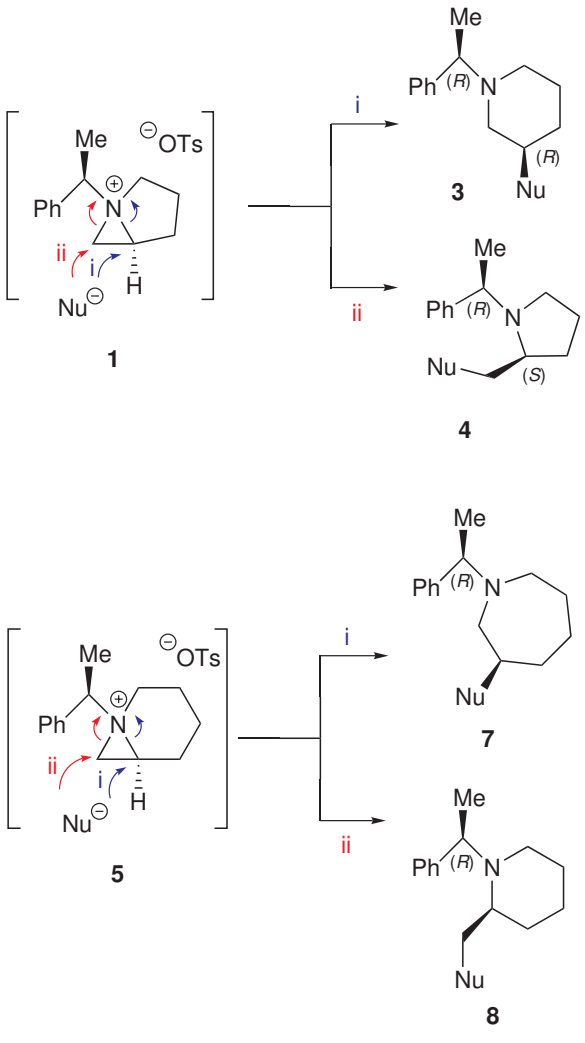

Figure 3.7. Schematic representation of ring-expansion reactions of 1-azonia bicyclo[3.1.0]hexane ion **1** (top) and 1-azoniabicyclo[4.1.0]heptane ion **5** (bottom).

3.2. Computational Procedure

An extensive Density Functional Theory (DFT) study was done on the ring-expansion reactions of 1-azoniabicyclo[3.1.0]hexane tosylates 1 and 1-azoniabicyclo [4.1.0]heptane tosylates 5. The optimizations were taken place at B3LYP [7] or M06-2X [9] functionals, employing 6-31+G(d,p) and 6-31++G(d,p) basis sets. A thorough analysis on possible conformers of all reactants, transition states and products was performed. Dispersion corrections were also added to B3LYP energies by means of Grimme's scheme DFT-D3 [28, 29], to append non-covalent interactions. Energy refinements were done at MPW1K [30] and BMK [31] functionals and 6-31+G(d,p) basis set. The performance of the functionals on the barrier heights and kinetics were comparatively analyzed.

Calculations were performed with Gaussian 09 software package [32]. Free energies are reported in kJs per mol at 1 atm and 298.15 K. Harmonic vibrational frequency analysis have been performed, as well as Intrinsic Reaction Coordinate (IRC) calculations to verify transition state geometries [33, 34].

Solvent effects are mimicked by different levels of solvation. The most common method of solvation, Polarizable Continuum Model (PCM) [11] was used for implicitly solvated systems. IEF-PCM [35] and C-PCM [36] methods were comparatively analyzed. Apart from implicit solvation, a discrete solvent model was employed to solvate the bicyclic aziridinium ions. The number of explicit acetonitrile molecules added to the systems were established by the value at which the coordination solvation energy converged, and adapted from a recent similar study [1]. A more detailed description of these solvation models can be found in Computational Methodology chapter.

To obtain a deeper understanding of the reaction mechanism, Activation-Strain Model (ASM) was used [37]. This model was designed to pinpoint favorable and unfavourable interactions in the transition states. A schematic representation of Activation Strain Model can be found in Figure 3.8.

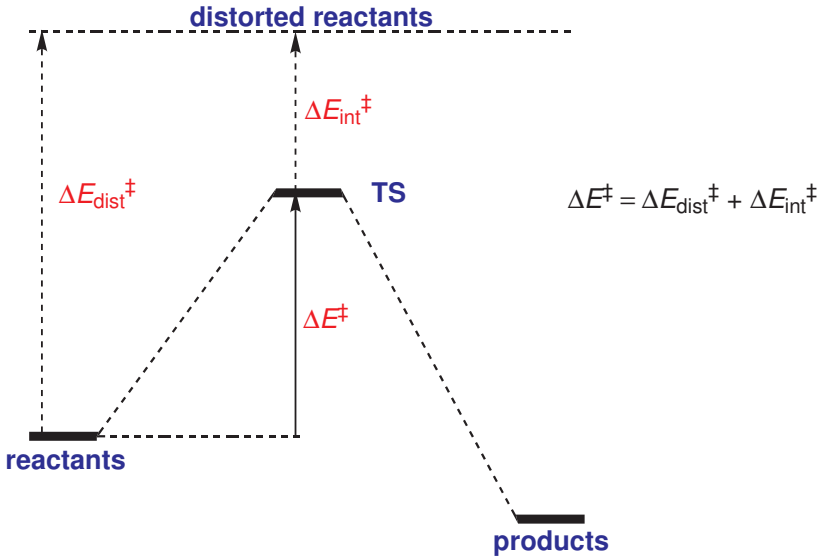

Figure 3.8. Schematic representation of Activation-Strain Model (ASM) [35].

According to Activation-Strain Model, the relative energy of a complex system is fragmented into two discrete units, referring to the deformation of the reacting systems and the consecutive interaction between them [38]. In a practical point of view, transition state structure needs to be shattered into suitable fragments. In the case of a bimolecular reaction, the clear and simple option is to select the initial reactants as the fragments to be analyzed during the transition state [39].

3.3. Transition State Analysis

As described before, there are two possible attack sites for the nucleophiles in their reactions with bicyclic aziridinium ions. For aziridinium substrate 1, CN, N_3 and Cl nucleophiles were investigated, and in the case of aziridinium substrate 5, CN, N_3 and NH_2 nucleophiles were included in the theoretical analysis. Transition states are located with both B3LYP and M06-2X functionals. A schematic representation for the possible pathways are given in Figure 3.9.

Transition state structures regarding all systems are shown in Table **??**. Explicitly added acetonitrile molecules interacts with nucleophiles at distances around 2.0 and 3.0 ångströms. Counter ion tosylate group were not included in the optimizations,

since it would not be in close relation with the reaction site due to the presence of highly-dielectric solvent acetonitrile. (ε=35.688)

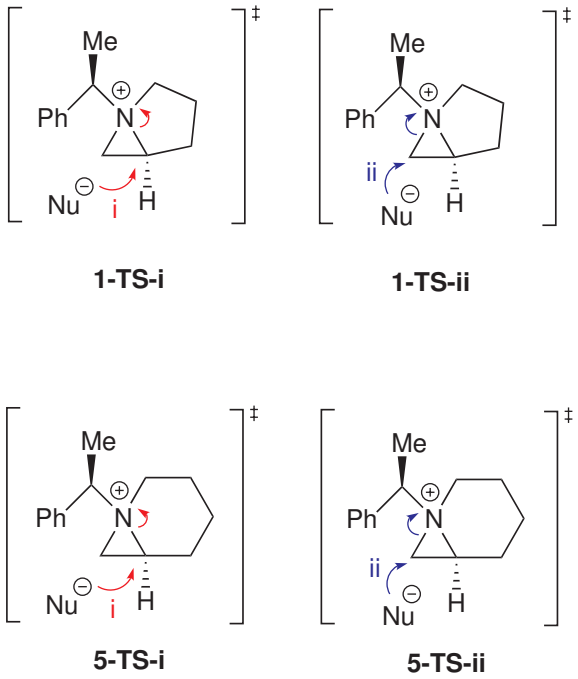

Figure 3.9. Schematic representation of transition states leading to ring expansion products.

For the ring-expansion reaction of aziridinium 1, the nucleophile azide prefers to attack in a closer distance to bicyclic substrate for both path i and path ii, when compared to cyanide and chloride nucleophiles. Contrarily, chloride ion exhibits the biggest attack distances. In the case of aziridinium 5, the trends of azide attack distances continue to be the smallest in comparison with other nucleophiles.

When the hindered and unhindered routes, path i and path ii are compared, the hindered carbon atom is not easily accessible to be attacked by a nucleophile. Thus, the critical distances appears to be longer when compared to its unhindered counterpart. A more detailed analysis on transition state critical distances are given in the next section.

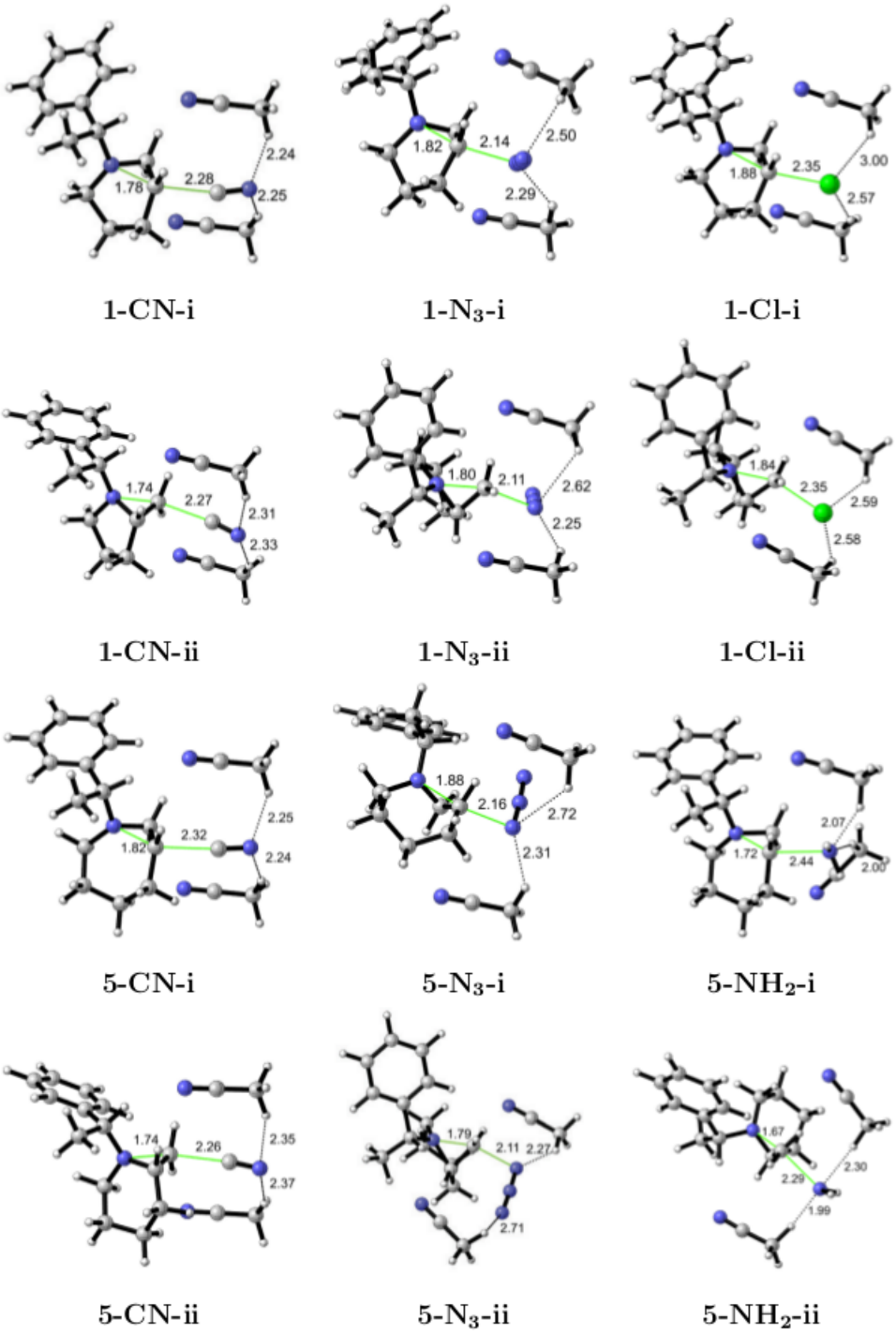

Figure 3.10. Transition state geometries of **path i** (hindered) and **path ii** (unhindered) for the ring-expansion of bicyclic aziridinium ions **1** (top) and **5** (bottom) with different nucleophiles (M06-2X/6-31+G(d,p); two explicit acetonitrile molecules; critical distances in Å)

3.3.1. Bond Elongation

A further investigation was done by calculating the bond elongation percentages of the transition states. A schematic representation for the numbering of the carbon atoms are given in Figure 3.10. More hindered carbon atom is denoted as C2, and less hindered one is denoted as C3. The bond-elongation results of both implicitly and explicit solvated transition states are shown in Table 3.2. In this table, d(Nu-C2) and d(Nu-C3) show the attack distances of applied nucleophiles. d(N-C2) and d(N-C3) indicates the scope of ring opening during transition state. Based on critical distances in transition states corresponding to ring-expansion reactions, bond elongation percentages are calculated according to Equation 3.1:

$$P(N-C)(\%) = \frac{d_{TS} - d_{reactant}}{d_{reactant}} \times 100 \tag{3.1}$$

The attack distances are mainly related to the steric effects and the nature of the nucleophile. The attack of a nucleophile on the hindered carbon atom C2 is more difficult due to the steric hindrance caused by the substituent on this carbon atom. This situation results in higher bond elongation percentages P(N-C2) when compared to P(N-C3) for each bicyclic aziridinium substrate and applied nucleophile. When different models of solvation are taken into account, implicitly solvated systems usually higher bond elongation than explicitly solvated systems. The interaction between

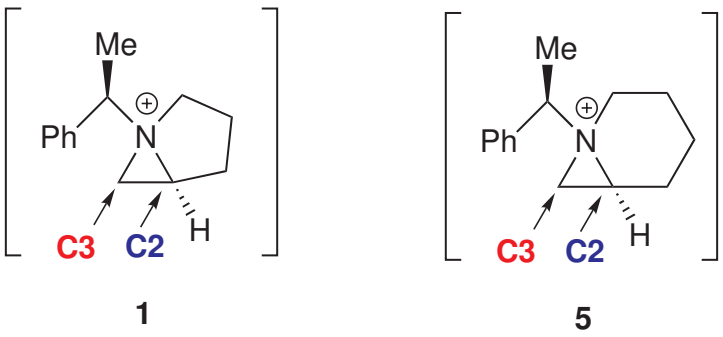

Figure 3.11. Schematic representation of more hindered carbon atom C2 and less hindered carbon atom C3.

nucleophiles and explicit acetonitrile molecules gives rise to higher attack distances.

For the ring-expansion of bicyclic aziridinium 1, the attack distances d(Nu-C2) and d(Nu-C3) corresponding to two different routes for cyanide and chloride are highly close to each other. The difference between two competitive pathways are more pronounces in azide case, by having d(Nu-C2) and d(Nu-C3) distances around 2.14 and 2.11, respectively.

When the reactions of 1-azoniabicyclo[4.1.0]heptane ion 5 are considered, the distinction between two paths are more noticeable. For instance, implicitly solvated cyanide nucleophile prefers to attack the bicyclic aziridinium 5 at a distance of 2.27 Å for more hindered path i, and 2.21 Å for less hindered path ii. Due to the fact that ring size is bigger in aziridinium 5 substrate, hindered path is less accessible to nucleophile attack, and thus, transition state critical distances appear to be longer.

Another point needs to be taken into consideration is d(N-C2) and d(N-C3) distances. The values of d(N-C2) and d(N-C3) in bicyclic aziridinium ions 1 and 5 are around 1.50 Å. More deviation from the initial reactant distances indicates a more deformed transition state. When we compare two distinct routes, d(N-C2) values are always higher than its less hindered alternative path.

Bond elongation percentages for bicyclic aziridinium 1 increases in the order of cyanide, azide and chloride. Cyanide attack to aziridinium substrate has the less deformation in the ring, indicating a more reactant-like transition state. In contrast, chloride with its softer nature as a nucleophile, induces higher bond elongation percentages. In the case of bicyclic azirinium 5, azide nucleophile exhibits the highest bond elongation. NH_2 nucleophile clearly causes the less deformation in the ring with its low P(N-C2) and P(N-C3) values around 12-15 %, and displays the lowest bond elongation.

Table 3.2. Transition state critical distances (Å) and bond elongation percentages of **path i** (hindered) and **path ii** (unhindered) for bicyclic aziridinium ions **1** and **5**.

			Path i (hindered)			**Path ii** (unhindered)		
		Azirid.	d(Nu-C2)	d(N-C2)	P(N-C2)	d(Nu-C3)	d(N-C3)	P(N-C3)
CN	Implicit	**1**	2.23	1.83	22.8	2.22	1.79	20.9
	Explicit	**1**	2.28	1.78	19.5	2.27	1.74	17.6
N_3	Implicit	**1**	2.11	1.86	24.8	2.08	1.82	23.0
	Explicit	**1**	2.14	1.82	22.1	2.11	1.80	21.6
Cl	Implicit	**1**	2.32	1.93	29.5	2.30	1.90	28.4
	Explicit	**1**	2.35	1.88	26.2	2.35	1.84	24.3
CN	Implicit	**5**	2.27	1.86	24.0	2.21	1.79	20.9
	Explicit	**5**	2.32	1.82	21.3	2.26	1.74	17.6
N_3	Implicit	**5**	2.13	1.90	26.7	2.08	1.83	23.6
	Explicit	**5**	2.16	1.88	25.3	2.11	1.79	20.9
NH_2	Implicit	**5**	2.39	1.74	16.0	2.36	1.66	12.2
	Explicit	**5**	2.44	1.72	14.7	2.29	1.67	12.8

3.3.2. Ring Distortion

As emphasized before, ring-expansion reactions of bicyclic aziridinium ions are S_N2 type of reactions, which incorporate a pentavalent character on attacked carbon atoms. Increasing sterics during the transition state leads to geometrical deformation. This deformation can be shown by the distortion energy ΔE_{dist}. Moreover, there is also a stabilizing interaction between the reactants, and this can also be analyzed by calculating interaction energy ΔE_{int}. The interaction energy is an indicator of how well the reactants oriented towards each other. The results are shown in Table 3.3

Table 3.3. Distortion and interaction energies for bicyclic aziridinium ions **1** and **5** in their ring-expansion reactions with different nucleophiles. (M06-2X/6-31+G(d,p), energies in kJ/mol at 298 K and 1 atm, IEF-PCM in acetonitrile)

		$\Delta E^{\ddagger}_{\text{dist}}$		$\Delta E^{\ddagger}_{\text{int}}$		
Nu	Azirid.	Path i	Path ii	Path i	Path ii	Exp
CN	**1**	83.8	81.8	-32.3	-37.3	0:100
N_3	**1**	95.8	96.9	-52.0	-53.2	36:64
Cl	**1**	119.3	121.0	-49.1	-55.4	100:0
CN	**5**	98.1	88.7	-44.6	-48.5	8:92
N_3	**5**	103.7	102.8	-60.6	-64.5	59:41
NH_2	**5**	45.8	36.1	-33.3	-34.3	65:35

For the ring-expansion reactions of 1-azoniabicyclo[3.1.0]hexane ion 1 with CN, N_3 and Cl nucleophiles, there is no noticeable difference between the distortion energies of two competitive pathways. When applied nucleophiles are considered, distortion energies decrease in the order of chloride, azide and cyanide. This order is consistent with bond elongation results. Softer nucleophile chloride resulted a greater deformation in the transition state, whereas cyanide has approximately 25 kJ/mol lower distortion energies than chloride, owing to its harder nature.

In the case of aziridinium ion 5, cyanide shows a clear preference of unhindered path, with its distortion energies of 98.1 and 88.7 kJ/mol for path i and path ii, respectively. In azide case, there is no distinction for hindered and unhindered cases. NH_2 nucleophile has considerably lower distortion energies when compared to other nucleophiles. Distortion energies are in line with bond elongation percentages and experimental results.

When the interaction energies are taken into account, a more negative value indicates higher interplay between two fragments. Unhindered route path ii always depicts higher interaction in its transition states, due to being more accessible to nucleophiles during the attack. A subtle difference has not been observed in interaction energies regarding two competitive pathways.

3.4. Gibbs Free Energies of Activation ($\Delta G^{\ddagger}$) and Reaction (ΔG_{rxn})

In this section, a thorough energetic analysis has been conducted, to further investigate the reaction mechanism. Gibbs free energies of activation ($\Delta G^{\ddagger}$) and reaction (ΔG_{rxn}) have been calculated via optimizations at B3LYP and M06-2X levels of theory, employing 6-31+G(d,p) and 6-31++G(d,p) basis sets. Energy refinements were done, in an effort to provide for dispersive and non-covalent interactions.

In Table 3.5, differences in reaction barriers correspond to two competitive pathways are given. The transition states have been explicitly solvated, as it was previously shown in Figure **??**. Explicit/Implicit section in Table 3.5 refers to energy refinement with IEF-PCM in acetonitrile in order to assess mixed implicit/explicit model on transition states.

According to $\Delta\Delta G^{\ddagger}$ values, path ii is proven to be kinetic pathway for both bicyclic aziridinium substrates. For bicyclic system 1, chloride nucleophile shows the greatest differences between two pathways, with a value of 10.3 and 13.2 kJ/mol for explicit and mixed explicit/implicit model, respectively. In the case of bicyclic aziridinium 5, azide nucleophile has the smallest difference. Including an energy refinement

to manifest the changes upon a mixed model did not show any clear trend that applies to all nucleophiles.

Table 3.4. Differences in Gibbs free energies of activation $\Delta\Delta G^{\ddagger}$ for the ring-expansion of 1-azoniabicyclo[n.1.0]alkane 1 and 5 with different nucleophiles. (M062X/6-31+G(d,p), energies in kJ mol at 298 K and 1 atm.)

		Explicit		Explicit/Implicit	
Nu	Azirid.	Path i	Path ii	Path i	Path ii
CN	1	7.4	0.0	11.3	0.0
$\mathbf{N_3}$	1	7.9	0.0	7.7	0.0
Cl	1	10.3	0.0	13.2	0.0
CN	5	11.4	0.0	13.9	0.0
$\mathbf{N_3}$	5	3.5	0.0	4.2	0.0
$\mathbf{NH_2}$	5	10.0	0.0	8.3	0.0

Consequently, Table 3.5 indicates that unhindered route is the kinetic, and hindered route is the thermodynamic route for this reaction. Following this, one would expect the ring expansion reactions with aziridinium 1 exclusively yields the thermodynamic product pyrrolidines 4. Nevertheless, this outcome is not consistent with the experimental outcome. For this reason, product stabilities and reaction reverse barriers are also portrayed in the next section, via reaction profiles constructed with respect to different level of theories.

Gibbs free energies of activation and reaction are given in Table 3.6 and 3.7. Table 3.6 refers to energy refinement with Grimme's dispersion correction scheme applied on B3LYP/6-31++G(d,p) calculations. Also, M06-2X/6-31+G(d,p) optimizations are given in this table to obtain a bigger and better perspective via including more HF exchange in optimizations. Implicit solvent calculations have been done with IEF-PCM. Another continuum solvation model, C-PCM, have also been performed. C-PCM resuls are given in Appendix A, since very similar results have been obtained in

IEF-PCM and C-PCM calculations.

When explicit and implicit solvation results are compared, barrier heights are noticeably higher in implicitly solvated systems. For instance, cyanide nucleophile has a barrier of 28.5 kJ/mol in its reaction with bicyclic substrate 1 via hindered path i when solvent effects are included two discrete solvent molecules (B3LYP/6-31++G(d,p)). Same reaction of cyanide and bicyclic aziridinium 1 has a barrier of 70.0 kJ/mol in implicitly solvated system. This is because of the reference state; seperate reactants (aziridinium substrate + nucleophile) are used in implicitly solvated systems, whereas pre-reactive complexes are adopted as reference states in explicit solvation.

The barrier heights follow the same fashion regarding two competing pathways, irrespective of the level of theory and solvation model employed in the optimizations. This situation assures the consistency and predictive power of theoretical models used in modeling this reaction mechanism. When dispersion corrected GGA M06-2X functional is used in the optimizations, reaction barriers are consistently higher. This circumstance is most probably due to extra stabilization of reactants, due to the long-range corrected nature of M06-2X.

In the case of 1-azoniabicyclo[3.1.0]hexane ion 1, CN nucleophile leads to a ring-expansion reaction more exothermic in nature when compared to azide and chloride nuclephiles. For instance, ΔG_{rxn} values corresponding to implicitly solvated cyanide (M06-2X/6-31+G(d,p)) are -150.2 and 139.4 kJ/mol for path i and path ii. Whereas azide ensues products 3 and 4, more than 70 kJ/mol higher in energy than cyanide products. Following this, the product-like nature of chloride is even more pronounced according to ΔG_{rxn} energies, since it has the least stable products 3 and 4. The experimentally observed outcome of chloride nucleophile exclusively yielding azepanes can easily be seen from this table, since there is a clear difference in ΔG_{rxn} energies in implicitly solvated systems, such as -7.7 and 11.4 kJ/mol for path i and ii, respectively.

For 1-azoniabicyclo[4.1.0]heptane ion 5, the certain preference of cyanide in experimental settings can be rationalized by the Gibbs free activation and reaction energies,

in which the unhindered route is favored by around 11-12 kJ/mol according to the M06-2X results. In related manner, the thermodynamic product appears to be piperidines 8 for each nucleophile employed. When bicyclic substrate 1 is treated with highly reactive metal amines, the reaction barriers eventuates in very low values, around 50 kJ/mol. Even though a 10 kJ/mol difference is observed between two competitive pathways, the resulting barrier heights are remarkably low to foresee a dominant preference over any of the routes, since both attack sites are regarded as almost equally attainable. The value reported for 7/8 product ratio in the case of azide nucleophile is 59:41, which can not be accurately reproducible within the scope of DFT; a higher level of theory is needed in terms of computational methods. Yet, the product stabilities turn out to be similar for 7/8, resulting in -61.6 and -62.8 kJ/mol, respectively.

Energy refinements have been done via kinetic functionals, namely BMK and MPW1K. They both include similar fraction of exact (HF) exchange: 42% and 42.7%, respectively. 6-31+G(d,p) basis set were used in single point calculations. The results are given in Table 3.7. The reaction barriers $\Delta G^{\ddagger}$ are similar to M06-2X optimizations, and notably higher than B3LYP-D results. Reiteratively, bicyclic substrate 1 and cyanide favors the kinetic pathway, without being able to undergo thermal equilibrium. Azide shows a similar selectivity upon two competitive routes, rationalizing the experimental results. In addition, energy refinement calculations with BMK and MPW1K functionals clearly indicate that, metal amine distinctively results in lowest barriers for both paths, around 40 kJ/mol differences when compared to the other nucleophiles. The superior reactivity of NH_2 nucleophile can be better observed in Table 3.7.

Table 3.5. Gibbs free energies of activation and reaction for the ring-expansion of bicyclic aziridinium ions 1 and 5 with different nucleophiles.

			B3LYP-D/6-31++G(d,p)				M06-2X/6-31+G(d,p)				
			Path **i**	Path **ii**	Path **i**	Path **ii**	Path **i**	Path **ii**	Path **i**	Path **ii**	
		Nu	$\Delta G^{\ddagger}$		ΔG_{rxn}		$\Delta G^{\ddagger}$		ΔG_{rxn}		Exp
Explicit solvent	1	**CN**	28.5	19.7	-211.5	-204.7	37.7	30.3	-204.2	-201.1	0:100
	1	**N_3**	31.8	28.5	-123.4	-105.4	50.9	43.0	-127.0	-112.4	36:64
	1	**Cl**	27.9	21.8	-68.5	-50.7	51.3	41.4	-63.5	-46.5	100:0
	5	**CN**	32.7	23.8	-180.7	-193.3	49.6	38.2	-178.7	-196.8	8:92
	5	**N_3**	28.2	26.2	-92.0	-109.6	66.6	63.1	-79.2	-81.4	59:41
	5	**NH_2**	40.1	28.2	-250.1	-253.3	26.6	16.6	-286.4	-292.1	65:35
Implicit solvent	1	**CN**	70.0	61.6	-151.4	-140.0	89.6	77.4	-150.2	-139.4	0:100
(IEFPCM)	1	**N_3**	59.5	58.4	-75.9	-57.0	82.0	78.6	-83.0	-63.7	36:64
	1	**Cl**	75.2	69.5	-1.5	15.0	96.7	90.8	-7.7	11.4	100:0
	5	**CN**	67.9	63.8	-127.0	-139.2	90.5	78.2	-124.3	-136.8	8:92
	5	**N_3**	59.1	59.8	-54.0	-57.6	87.3	78.2	-61.6	-62.8	59:41
	5	**NH_2**	38.2	31.0	-239.5	-242.0	54.9	43.1	-249.9	-252.5	65:35

Table 3.6. Gibbs free energies of activation and reaction for the ring-expansion of bicyclic aziridinium ions 1 and 5 with different nucleophiles.

		BMK/6-31+G(d,p)				MPW1K/6-31+G(d,p)				
		Path **i**	Path **ii**	Path **i**	Path **ii**	Path **i**	Path **ii**	Path **i**	Path **ii**	
	Nu	$\Delta G^{\ddagger}$		ΔG_{rxn}		$\Delta G^{\ddagger}$		ΔG_{rxn}		Exp
1	**CN**	87.3	75.2	-140.1	-131.2	93.0	82.5	-155.4	-147.8	0:100
1	$\mathbf{N_3}$	85.3	81.4	-70.5	-53.8	93.0	90.6	-74.2	-59.7	36:64
1	**Cl**	94.8	88.5	0.5	17.1	99.7	96.0	-0.93	14.9	100:0
5	**CN**	87.5	77.6	-116.2	-128.3	94.1	85.3	-129.8	-143.3	8:92
5	$\mathbf{N_3}$	91.1	82.5	-51.6	-52.8	99.2	92.2	-54.5	-57.1	59:41
5	$\mathbf{NH_2}$	54.8	46.4	-248.2	-252.2	63.1	52.1	-252.0	-256.7	65:35

3.5. Free Energy Profiles

Figure 3.12 and Figure 3.13 exhibit the Gibbs free energy profiles for bicyclic aziridinium substrate 1 and aziridinium substrate 5, respectively. The optimizations have been performed at M06-2X/6-31+G(d,p) level of theory with IEF-PCM solvation. Energy profiles have been constructed in an effort to emphasize the significance of reverse barrier height in the reactions.

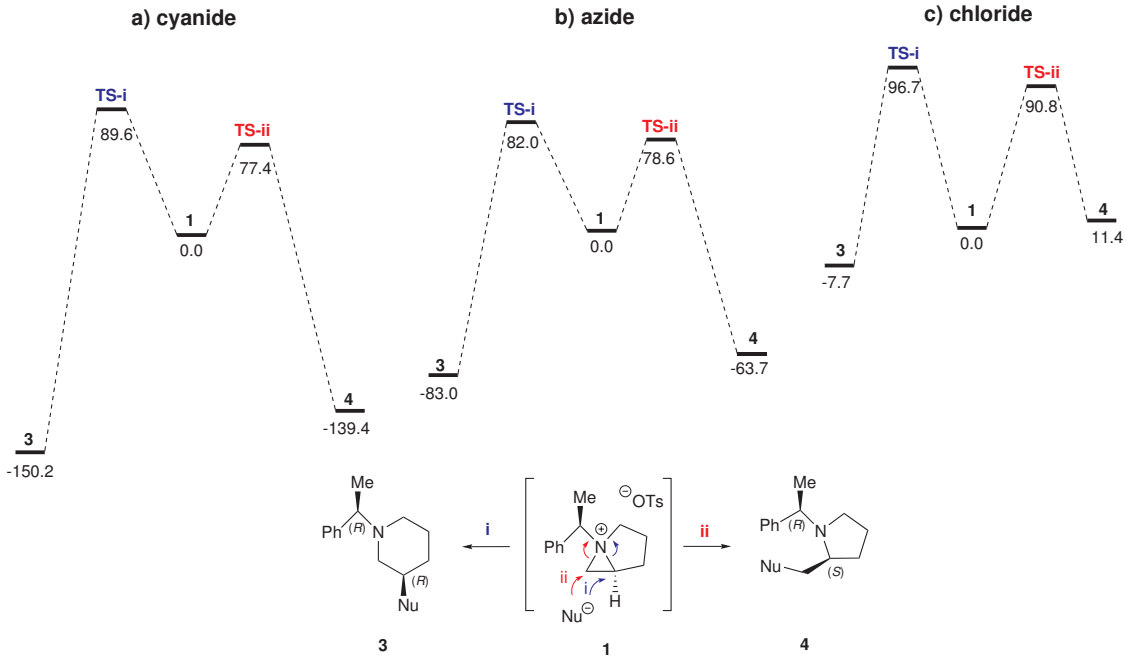

Figure 3.12. Gibbs free energy profiles for the ring-expansion of 1-azoniabicyclo [3.1.0]hexane 1 with different nucleophiles.

For 1-azoniabicyclo[3.1.0]hexane ion 1 with cyanide, one can immediately spot the high reverse barriers around 200 kJ/mol, which prohibits the chances of thermodynamic equilibrium. In contrast, chloride has around 90 kJ/mol reverse barriers, which can be surmounted, and eventually forming the thermodynamic product 3.

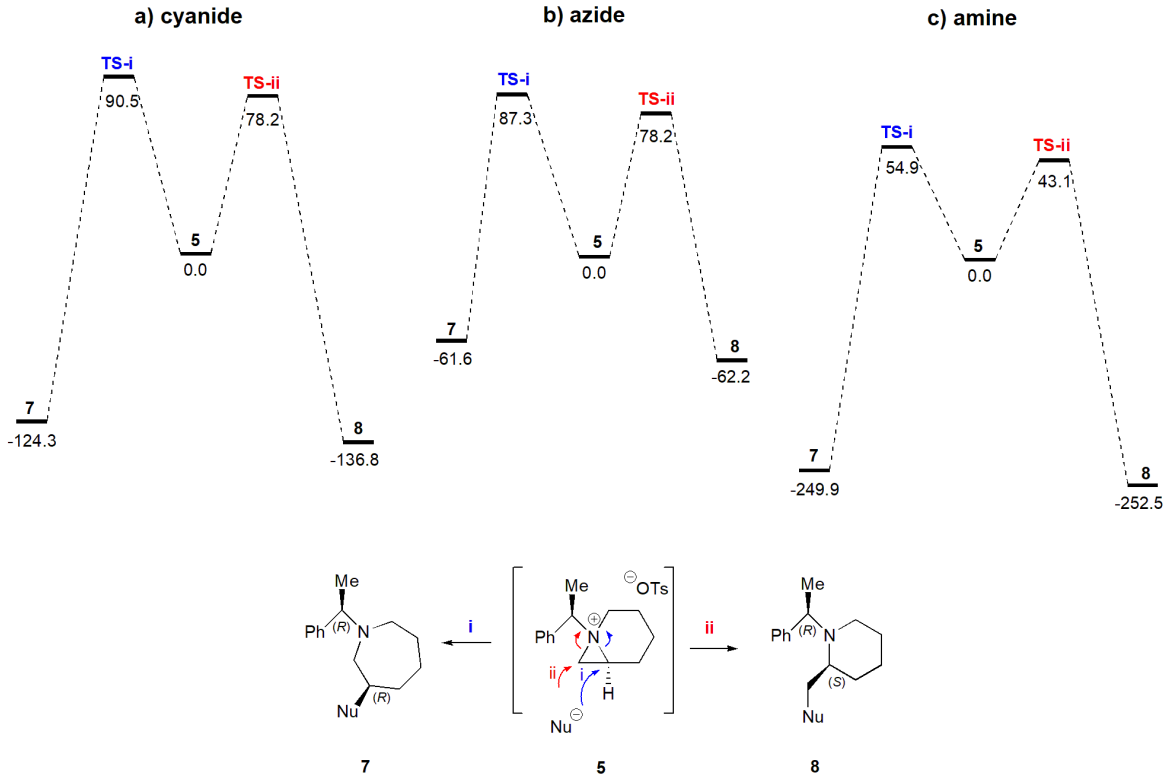

Figure 3.13. Gibbs free energy profiles for the ring-expansion of 1-azoniabicyclo [4.1.0]heptane 5 with different nucleophiles.

3.6. Conclusion

In the first part of this thesis, nucleophilic ring-expansion reactions of 1-azonia bicyclo[3.1.0]hexane and 1-azoniabicyclo[4.1.0]heptane ions are theoretically investigated. For bicyclic aziridinium 1, cyanide, azide and chloride nucleophiles, for bicyclic aziridinium 5, cyanide, azide and amine nucleophiles are selected in modeling reaction mechanisms. The paramount goal was to institute a computational methodology capable of predicting the outcome of future studies on similar reactions.

A detailed analysis of transition states were performed on both systems and both possible pathways. Gibbs free energy profiles were constructed, and different solvation methods were comparatively used. In addition to energetic analysis, transition state structures were thoroughly analyzed.

When the solvation models are taken into account, IEF-PCM and C-PCM optimizations resulted in highly similar structures and results. Calculated activation barriers consistently increased when M06-2X functional is used in the optimizations, due to stabilization of reactants. The trends in regioselectivities turned out to be rigid across different types of methods used in calculations.

The thermodynamic products were emerged to be piperidines 3 for bicyclic aziridinium 1, and piperidines 8 for bicyclic aziridinium 5. For both systems, unhindered route path ii was substantiated to be the kinetic pathway. In terms of regioselectivity, the quantity of the barrier heights depends on the nature of the nucleophile to a great extent. If the reverse barriers are attainable, thermodynamic equilibrium will favor the thermodynamic product, as expected.

Consequently, free energy profiles indicated that the nature of the nucleophile dictates the experimental results. In both systems, cyanide displayed an early transition state, and a clear preference over the less hindered route. Azide nucleophile exhibited very low regioselectivity in its ring expansion reaction with both bicyclic substrate 1 and 5. Chloride exclusively yielded the thermodynamic product, due to a feasible thermal equilibrium. Among all nucleophiles tested, metal amine showed the lowest barriers and highest exothermicities in each theory employed, and did not manifest any dominant affinity towards to competitive pathways.

4. PHOTOPHYSICAL PROPERTIES AND ELECTRONIC STRUCTURE OF ADSORBED DTP-π-A ORGANIC SENSITIZERS ON TiO_2

4.1. Background

Throughout roughly 4.5 billion years of its long history, Earth has interchangeably warmed and cooled from time to time. These changes in global climate were a result of natural occurrences. Receiving more or less sunlight by virtue of faint shifts in its orbit, or varying energy of the Sun contributed to the alteration of carbondioxide level in the atmosphere. However, another element has started to affect Earth's climate: humanity. As human beings, we are now fully proficient in dominating all the ecosystems within Earth. This domination paves the way to changes in Earth's functioning, and unfortunately serves as driving force for global climate change.

Fossil fuels and industry constitute approximately 90 % of all carbondioxide emissions, paving the way to unprecedented rise in global temperatures. Reducing greenhouse gases, mainly carbondioxide, now seems to be a must. Although there has been an increasing number of countries where emissions are declining, whether carbondioxide emissions will proceed to rise after 2018 is yet unclear.

Alternative energy sources continue to gain importance. There are countless number of organizations that take place in conducting research activites across the several subfields of the alternative energy spectrum. Sun, wind, rain, tides, waves and geothermal sources are the main elements of renewable energy.

The Sun has the energy potential of 89000 terawatts (TW) [40], while mankind only needs 12 TW to maintain lifestyle of 6.5 million people [41]. In addition to its energy potential, it is clean and safe. Effective use of solar energy plays a crucial role as a propitious and clean alternative to burning fossil fuels. In this sense, solar cells

(or photovoltaic cells) have attracted attention, since they were first displayed at Bell Laboratories in 1954 [42].

There are various types of solar photovoltaic cells. Currently, polycrystalline silicon based cells account for over 90% of market share [43]. Polysilicon consists of many fragments of silicon melted together to form a multi-crystalline structure. Since there are many crystals in each unit cell, the freedom is constrained for electrons to move. Polycrystalline silicon based solar cells are less expensive and less efficient than monocrystalline silicon based solar cells.

Another type of photovoltaic (PV) device is cadmium-telluride (CdTe) photovoltaics. This device belongs to thin film technology, and its high efficiency allows it to have the shortest energy payback time of all solar technologies. Cadmium being rare and toxic, there are still queries on this type of solar cells.

Within its very low production costs, perovskite solar cells are considered as the fastest-advancing solar technology [44]. Methylammonium lead halide is an example of a ABX_3 crystal structure of perovskite materials, and it is cheap and simple to synthesize. Despite the ease of fabrication, its poor stability was on the table, until the report of one-year stable perovskite with 11.2% efficiency [45].

The fact that organic dyes are capable of generating electricity at oxide electrodes was first discovered in the late 1960s. Later on, O'Regan and Gratzel produced the ground-breaking invention of Dye-sensitized Solar Cells (DSSCs) [46]. A schematic representation of the mechanism is given below. After the absorption of sunlight, photo excitation of the organic dye takes place. Being grafted onto the titanium dioxide semiconductor, dye transfers the excited electron to the conduction band of the anatase oxide layer. The transferred electron travels through an external load to counter electrode. The ground state of the dye is retained by the electron donors in the electrolyte. The donors can be reduced back to its original state by the photoexcited electrons, coming from the dye molecule in the first place, closing the circuit. In this respect, DSSCs can convert photons coming from sunlight to electricty, without causing any

abiding chemical transformation.

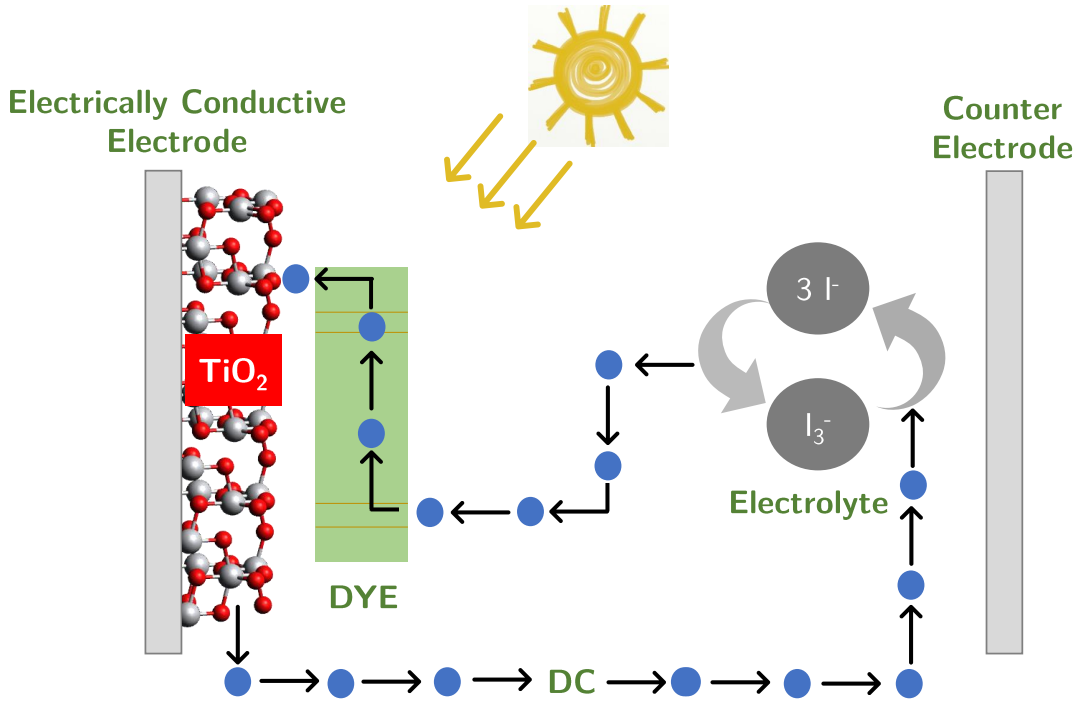

Figure 4.1. Working principles of a dye-sensitized solar cell.

The significance of harvesting sunlight and store electricity has been very-well understood. A decent amount of attention and thorough research efforts have been given to photovoltaic cells over the past two decades. Despite thousands of published papers on the subject, there hasn't been a breakthrough, and an important progress has not recently been shown in the device performance. A high percentage of the theoretical research articles focuses on only one main component of the device, which usually produces results far from reality.

In 2015, Sharmoukh et al reported a set of two D-π-A sensitizer based of 2,5-dithienylpyrrole (DTP) motifs [4]. These dyes were found to be distinguished sunlight harvesters when anchored on TiO_2 photoanodes. The structure of the dyes are given in Figure 4.2. The donor group is 2,5-dithienylpyrrole (DTP), and the π-delocalized bridge is styryl. The electron acceptor group is cyanoacrylic group, which ensures the grafting onto the TiO_2 surface [47]. The electronic properties of the dyes were investi-

gated by UV-vis absorption. The UV-vis and electrochemical data were given in Table 4.1.

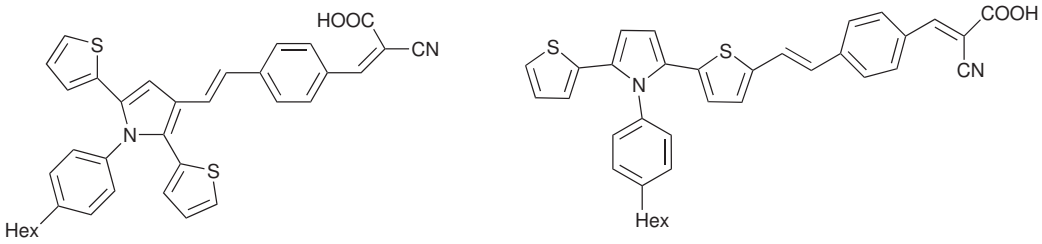

DTP1 **DTP2**

Figure 4.2. Structures of organic dyes DTP1 and DTP2 [4].

The π - π^* band for DTP1 molecule is observed around 334 nm, whereas this value for DTP2 is around 364 nm. Both dyes gave their absorption maximum wavelengths in the visible part, 415 nm and 458 nm for DTP1 and DTP2 respectively. As it is stated before, the connectivity of π bridge to the donor part is at thiophene for DTP2 and at pyrrole for DTP1. This difference in the molecular structure resulted in a red shift for DTP2.

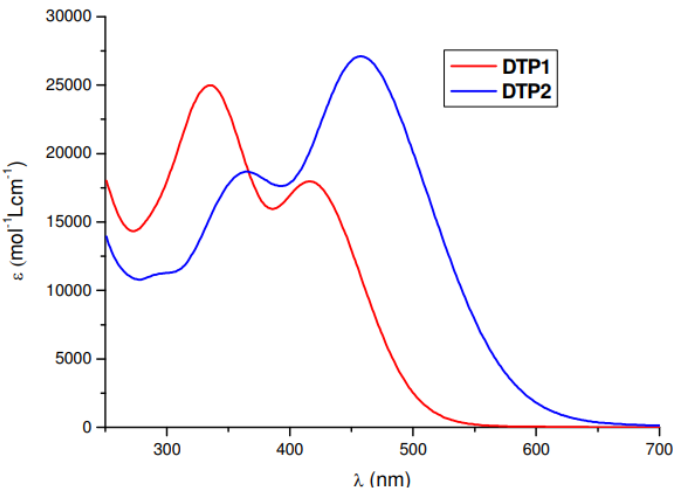

Figure 4.3. UV-Vis spectra of the dyes in dichloromethane [4].

The electrochemical properties of the dyes were measured by using a cyclic voltammetry. The results are given in Table 4.1. The oxidation potential of the dyes

were found to be 0.85 V for DTP1, and 0.68 V for DTP2. The results implicate that, restoring of dye's ground state by the iodide/triiodide redox mediator (0.2 V vs SCE) is thermodynamically favorable.

Table 4.1. UV-Vis and electrochemical data for dyes DTP1 and DTP2 [4].

Dye	$\lambda_{max}{}^{ab}$ (nm)	$\lambda_{max}{}^{em}$ (nm)	E_{ox} (V)	E_{red} (V)
DTP1	415	594	0.85	-1.50
	334	496, 594		
DTP2	457	685	0.68	-1.45
	364	542, 685		

Overall photovoltaic performances are given in Table 4.2. The values in parantheses have been obtained with the opaque TiO_2 photoanode. The photovoltaic measurements were done by using 7 μm TiO_2 layer. At first glance, the solar device with a DTP2-sensitizer showed better performance compared to DTP1-based device. In order to achieve a comparison, a ruthenium-based dye Z907 were also investigated in photovoltaic measurements. Under the same conditions, Z907 dye gave better performance, by resulting in 8.57 mA cm^{-2} of photocurrent and 3.85 % efficiency.

Table 4.2. Photovoltaic performance of DSSC sensitized by DTP1 and DTP2 [4].

Dye	$\mathbf{J_{sc}}$	$\mathbf{V_{oc}}$ (mV)	**FF**	**eff**
DTP1	4.29 (6.55)	570 (620)	0.61 (0.61)	1.49 (2.46)
DTP2	6.82 (7.60)	620 (610)	0.63 (0.60)	2.68 (2.80)
Z907	8.57 (8.50)	680 (640)	0.66 (0.64)	3.85 (3.46)

In Sharmoukh's work, a computational analysis was also performed at Time-Dependent Density Functional Theory (TD-DFT) level. In this sense, an absorption spectra and NTOs (natural transition orbitals) were examined to characterize the dye performances. This analysis were done with respect to isolated dye molecules. As a result of these quantum mechanical calculations, DTP2 showed a red-shift, accounting

for its better photovoltaic performance. In addition, the cyanoacrylic group was found to be less emphasized in DTP2's occupied NTOs, implying a better charge seperation.

The extended conjugation on these dyes, and their remarkable absorption capabilities were making them possible candidates for sensitization. To gain more insight into the device performances, and to propose improvements upon the dye's chemical structure, a computational analysis have initially been performed to report the linear and nonlinear optical properties of the stand-alone dyes [5].

In the work regarding isolated sensitizer molecules [5], a conformational analysis was performed on the dyes to explore the potential energy surface. After establishing ground state most stable geometries, excited state calculations were performed to obtain the absorption spectra of the dyes. The charge transfer nature were also investigated in this work, and it has been found out that, the charge transfer nature of these dyes are quite local. A significant result were also found in this work: The two-photon absorption capabilities of these dyes were found to be remarkable and this DTP based dye motifs were reported to be a notable candidates for TPA-sensitization.

The coupling between the dye and TiO_2 surface leads to hybridization of their molecular orbitals with the sequential change in their relative energy alignment. To account for this effect, the combined dye@semiconductor system has to be treated as a whole. For this reason, this part also includes theoretical investigation of two recent push-pull type organic dyes and its electronic structure when it is adsorbed on titanium dioxide surface.

4.2. Computational Procedure

Two different approaches were tested and comparatively analyzed. First one employed a $(TiO_2)_{82}$ cluster and the organic DTP dyes anchored onto the surface. Adsorption geometries of this model were obtained by using the generalized gradient approximation (GGA) PBE functional and TZP(DZP) basis set for Ti(H, C, N, O S), as implemented in ADF modeling suite. In addition to PBE functional, dispersion

corrections were also added by means of DFT-D3 and the results were compared. In single interface optimizations, solvent environment was included by Conductor-like Screening Model (COSMO) [48], as well as gas phase calculations. For extracting density of states, single point calculations were performed using B3LYP and CAM-B3LYP functionals with 6-31G(d) and 6-311G(d) basis sets as implemented in Gaussian 16 program package. In single point calculations, solvation effects were taken into account by means of IEF-PCM solvation in dichloromethane.

Periodic DFT calculations have been done using the periodic plane-wave code, Vienna *Ab Initio* Simulation Package (VASP) [49]. A large $(TiO_2)_{144}$ cluster with 434 atoms was constructed with lattice parameters of 30.25, 22.38, 45.70 Å. A conjugate-gradient (CG) algorithm have been used to relax the ions into their instantaneous groundstate. The exchange-correlation energy was characterized by GGA-PBE functional. The wavefunction and the density in the augmentation spheres were described by standard PAW atomic data sets. The volume and half of the atoms of the titanium dioxide semiconductor were fixed during the relaxation. The plane-wave cut-off energy was set at 400 eV for all materials. A convergence criterion of 10^{-6} eV was used for the electronic self-consistent cycle. The sampling of Brilliouin Zone were done by a k-point mesh of 1 x 1 x 1 in reciprocal lattice. Inclusion of dispersion corrections were done by DFT-D3 method during optimizations.

4.3. Stand-alone Sensitizers

The extended conjugation on these dyes, and their remarkable absorption capabilities were making them possible candidates for sensitization. To gain more insight into the device performances, and to propose improvements upon the dye's chemical structure, a computational analysis were performed to report the linear and nonlinear optical properties of the stand-alone dyes [5].

In this part, a conformational analysis was performed on the dyes to explore the potential energy surface. The respective positions of the substituents were taken into account. In optimizations, B3LYP and M06-2X functionals were used. The

dichloromethane solvent environment was mimicked by implicit solvation (IEF-PCM) during calculations. Ground-state best conformers are given in Figure 4.4.

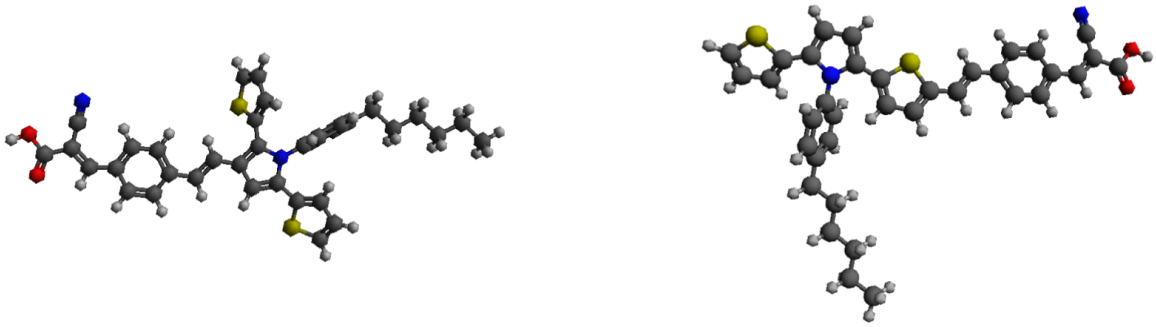

Figure 4.4. Optimized structures of DTP1 (left) and DTP2 (right).
(M06-2X/6-31+G(d,p), IEF-PCM in dichloromethane.)

4.3.1. Natural Transition Orbitals

There are many charge transport processes in an operating dye-sensitized solar cell. Initially upon light-absorption an exciton is generated. The source of the excited electron in an push-pull type of sensitizer is the donor part of the molecule. After the absorption, the electron is expected to be transferred to the semiconductor's conduction band states. These charge transport mechanisms have the upmost importance, since this step does not successfully transpire in a DSSC, the other processes will followingly be distrupted and finally resulting in a low electrical conversion efficiency. For this reason, the intramolecular charge transfer is investigated by performing quantum chemical calculations on isolated dye molecules DTP1 and DTP2.

It is essential to consider the excited state nature of the sensitizers. There are many quantum chemical methods that inspect electronic transitions. In this case, Natural Transition Orbitals and Detachment-Attachment density matrices are used in analysis of excited states topology. A detailed mathematical explanation of Detachment/Attachment matrices can be found in Computational Methodology chapter. In a more conceptual way, detachment represents the deficiency in electron density that arises from absorption. On the other hand, attachment acts for the increase in electron density in the excited state. These concepts are used to identify a transition between

Table 4.3. Occupied and virtual NTO's for the lowest energy conformers of DTP1 and DTP2.

Dye	oNTO	vNTO
DTP1 S_0 - S_1	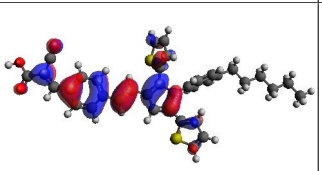	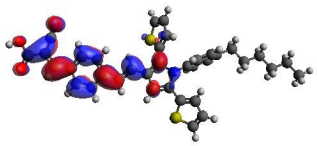
DTP1 S_0 - S_2	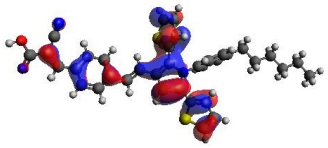	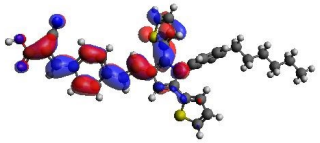
DTP2 S_0 - S_1	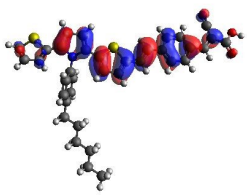	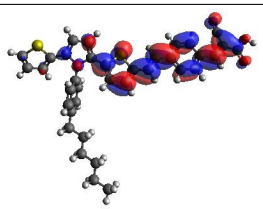
DTP2 S_0 - S_2	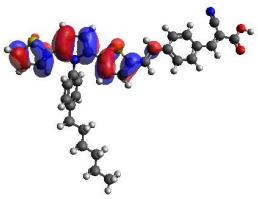	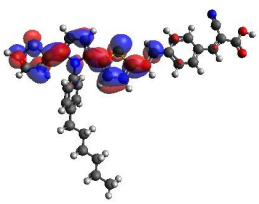

certain energy levels, and gives a qualitative description of the excited state.

Natural transition orbitals of DTP1 and DTP2 are given in Table 4.3. The oNTO stands for occupied Natural Transition Orbitals, and vNTO stands for virtual Natural Transition Orbitals. The electrostatic potential in their corresponding isodensity plots provides valuable information in terms of charge transfer. When the orbitals of DTP1 and DTP2 are considered, one can not see an observable difference in their occupied and virtual states. This statement is true for states that depicts the transition from ground state to first excited state, and to second excited state. However, in order to have an effective charge transfer procedure within the isolated molecule, there should have been an observable difference between the electron densities.

4.3.2. Absorption Spectra

In order to assess the vertical transition, absorption spectra were calculated for best ground state conformers of DTP1 and DTP2. The results are given in Table 4.4. ωB97X-D and CAM-B3LYP functionals are used to reproduce absorption spectra, utilizing 6-31+G(d,p) basis set.

These functionals were selected due to their range-seperated nature. They are intended to be capable of capturing both short-range and long-range interactions. In addition to range seperation, ωB97X-D functional also incorporates an empirical atom-atom dispersion correction [52]. Further information on functionals can be found in Computaional Methodology chapter.

For both DTP1 and DTP2, CAM-B3LYP results are extended towards visible region, in comparison with ωB97X-D and experimental results. In addition, if a modest charge seperation is present within a system, CAM-B3LYP may sustain significant deviations in reproducing vertical excitation [53, 54]. The differences in the vertical transition energies are in the order of 10^{-2} eV, which further reinforces the use of ωB97X-D as a functional quite suitable for reproducing absorption properties of these molecules. Since the experimental values [4] were reproduced for almost each conformer, the results for static calculations can be considered as highly propitious. In addition, when the structures of the two organic dyes are compared, the extended conjugation in DTP2 brings about the extension of the absorption toward the low energy region of the spectrum, both experimentally and theoretically.

4.4. Cluster Approach

A detailed atomistic description of dye@SC interface is given in this section. The modeling style studied herein consists of a cluster model, which represents the surface stoichometrically, and it governs the correct atomic ratio of the bulk semiconductor [55]. Bidendate-bridging anchoring of dyes onto the anatase titanium dioxide semiconductor was established. Optimizations were took place in different level of theories.

Table 4.4. Benchmark calculations and experimental results for absorption of DTP1 and DTP2.

	ωB97X-D	CAM-B3LYP	Expt. [4]
DTP1	414 (2.99)	431 (2.87)	415 (2.98)
	306 (4.05)	311 (3.98)	334 (3.71)
DTP2	458 (2.70)	479 (2.58)	457 (2.71)
	291 (4.26)	316 (3.92)	364 (3.40)

4.4.1. Modeling the Semiconductor

Titanium dioxide, also known as titania, has many applications, ranging from pigments in toothpaste and sunscreen, to photocatalysts and nanotubes. In 2014, it has been produced more than 9.000.000 metric tones worldwide [56].

TiO_2 exists in three different polymorphs: rutile, anatase and brookite. In terms of photocatalysis, anatase form is found to be more suitable and thermodynamically stable [57, 58].

As mentioned before, a DSSC photoanode consists of a sensitizer anchored onto a semiconductor. The device studied herein, has anatase (TiO_2) (101) surface in its photoanode. For the modeling of semiconductor, two different clusters were prepared, namely $(TiO_2)_{82}$ and $(TiO_2)_{144}$.

$(TiO_2)_{82}$ cluster is shown in Figure 4.2. This cluster size has been used in a number of studies, and it has been shown that this size has adequately described the electronic and optical properties of other organic sensitizers [50, 51]. After the bidendate anchoring of the dye carboxy group onto this semiconductor, full optimizations took place employing PBE functional.

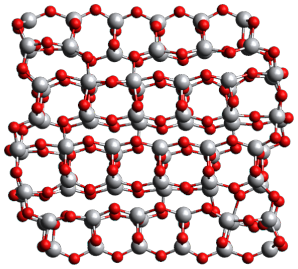

Figure 4.5. $(TiO_2)_{82}$ cluster

Modeling the charge injection in dye-sensitized solar cells requires thorough investigation. Efficient charge seperation has to be maintained and recombination of the injected electron to dye's ground state should be avoided. In this sense, one of the main aspects that need to be taken into account is dye adsorption mode.

Up to now, there has been a massive number of theoretical studies examining dye adsorption [59–61]. With the help of these investigations, it is now well-established that organic dyes bearing a carboxylic acid as anchoring group would prefer bidendate-bridging binding mode, with one proton is shifted to a nearby oxygen on the surface [62, 63]. Thus, the systems studied herein are constructed within bidentate bridging mode. A schematic representation of bidentate bridging is given below.

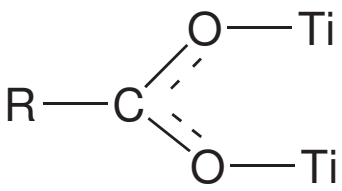

Figure 4.6. Schematic representation of a bidendate bridging mode.

4.4.2. Structural Properties of Dye-TiO_2 Interfaces

In an effort to point out the changes upon anchoring the dyes on the TiO_2 semiconductor, the structural properties are carefully examined through this section. As stated before, the donor component of the organic dyes is 2,5-Dithienylpyrrole (DTP), attached to the styryl π spacer. Grafting of the dyes is established through cyanoacrylic

acid; the bidentate bridging anchoring of the carboxylate fragments to titanium atoms in anatase surface.

The carboxylic group, which is acidic in nature, is contemplated to be initially protonated, since the dyeing solution should be charge neutral. Owing it to bidendate-bridging adsorption mode, the carboxylic proton has been transferred to a nearby oxygen. As a result, the dye molecules bind almost perpendicular to the titaniumdioxide surface with the formation of two O-Ti bonds.

Here various adsorption configurations regarding different level of theories are discussed. In order to obtain a complete picture at hand, optimizations were held in different level of theories. Calculations in gas phase, calculations with explicit dispersion correction DFT-D3, inclusion of solvent environment with COSMO solvation model were scrutinized in this section.

4.4.2.1. Inclusion of Dispersion Corrections. Gas phase optimizations in PBE functional and DZP basis set resulted in absorption geometries as shown in Figure 4.7. In all dye@SC systems, the O-Ti bonds between the sensitizer and the semiconductor were found to be around 2.05 and 2.20 angstroms.

In terms of adsorption geometries, an observable difference has not been found for PBE and PBE-D3 calculations. Gas phase adsorption geometries of DTP1 and DTP2 are given in Appendix D.

4.4.2.2. Inclusion of Implicit Solvation. Implicity solvated systems were optimized via COSMO solvation model, in dichloromethane. Optimized structures are given in Figure 4.7. DTP1 and DTP2 gas phase optimizations are also given in this table for comparison.

There has been an observable change on adsorption geometries upon addition of implicit solvation to the calculations. In gas phase optimizations, sensitizer molecules

have a configuration almost perpendicular to the semiconductor surface, as it can be seen in Table 4.5. On the contrary, inclusion of implicit solvation in the calculations resulted in bent dye molecules, leaning towards the semiconductor. A more closely packed configuration of implicitly solvated systems may indicate a better description of electronic structure, by having an increased electronic coupling between dye's LUMO and CB of titanium dioxide surface.

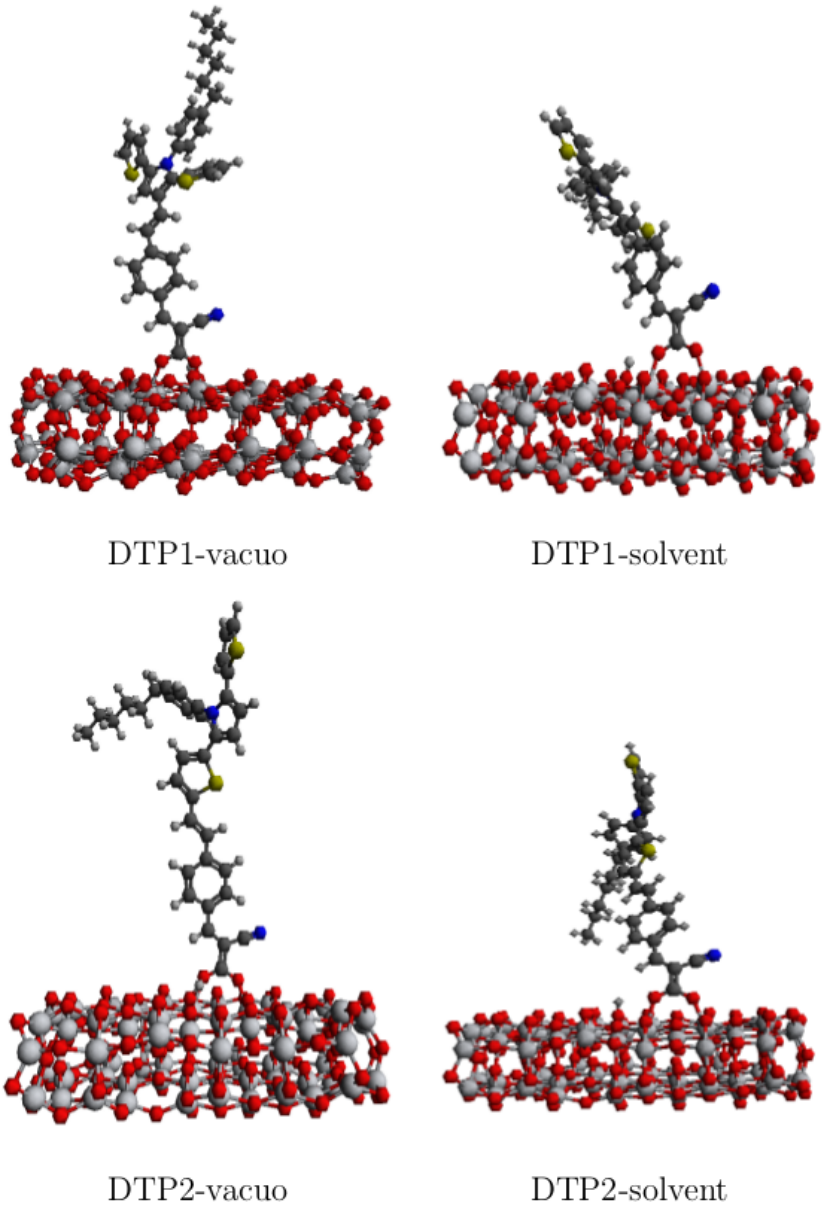

Figure 4.7. Comparison of adsorption geometries of DTP1 and DTP2 in gas phase and in solvent.

4.4.2.3. Impact of Grafting on Dye Electronic Structure. Adsorption of sensitizers on top of semiconductor results in a different geometry for the dyes due to the interaction with titanium dioxide surface. HOMO-LUMO levels need to be thoroughly analyzed due to the fact that they constitute the lowest electronic excitation. In section 4.3, isolated dye molecules were investigated by means of Natural Transition Orbitals (NTOs). In this section, dye parts have been cut from the interface after the optimizations, and Frontier Molecular Orbitals are analyzed in comparison with isolated dye molecules. The structures which were previously optimized while being grafted onto the semiconductors are denoted as "Grafted", whereas isolated dye molecules are referred to as "Isolated".

Compared to isolated dye molecules, grafted geometries afford higher HOMO energy levels for both DTP1 and DTP2.

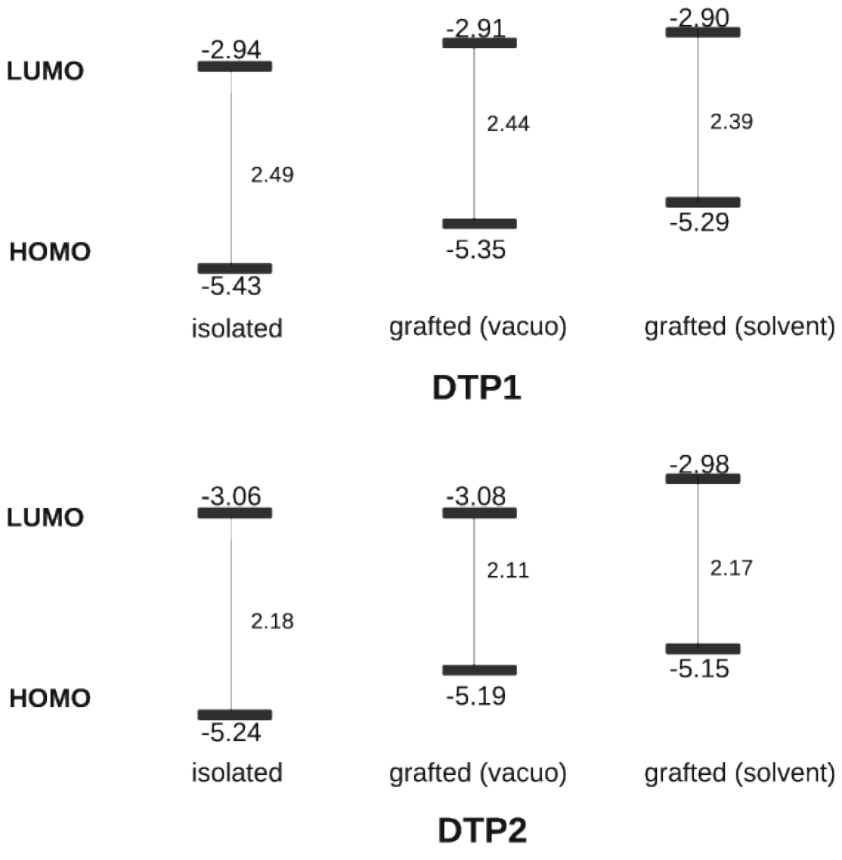

Figure 4.8. HOMO-LUMO levels for DTP1 and DTP2. (B3LYP/6-31+G(d,p), IEF-PCM in dichloromethane, energies in eV.)

Table 4.5. Isodensity plots for HOMO and LUMO levels for DTP1 and DTP2. (Single points at B3LYP/6-31+G(d,p), IEF-PCM in dichloromethane.)

		Isolated	Grafted (vacuo)	Grafted (solvent)
DTP1	LUMO	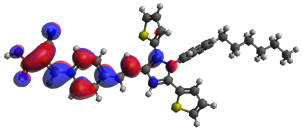	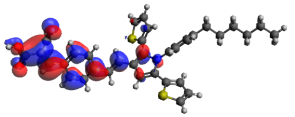	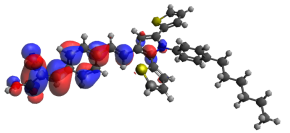
DTP1	HOMO	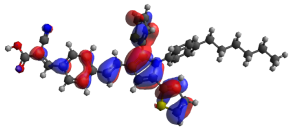	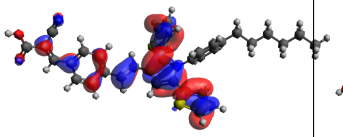	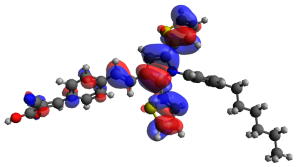
DTP2	LUMO	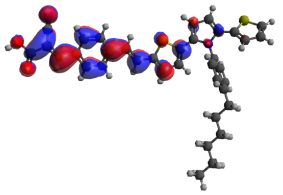	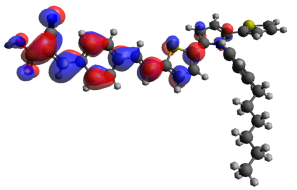	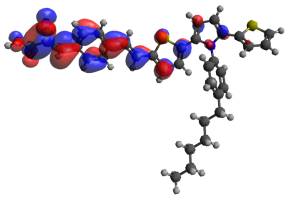
DTP2	HOMO	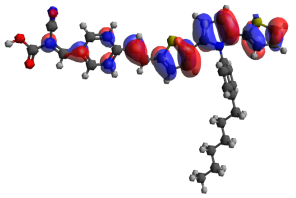	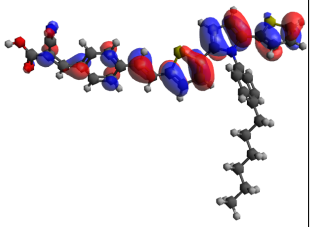	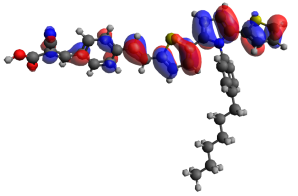

4.4.3. Electronic Properties of Dye-TiO_2 Interfaces

The charge transfer process across the dye@SC interface is assumed to be controlled by a strong electronic coupling between the unoccupied states of the dye and the conduction band (CB) of the semiconductor [64]. For this reason, the key elements of electron coupling can be established by analyzing the interfacial orbital mixing.

The apportionment of frontier molecular orbitals and the energy gap of the organic sensitizer are crucial parameters to elucidate the electronic properties of the dyes. The accumulation of the electrons at the HOMO and LUMO energy levels confirms the reactive sites in the push-pull sensitizers. Considering both isolated dye molecules and dye@TiO_2 interfaces is essential to apprehend the changes in electronic structure upon anchoring of the dyes. This part concentrates on the electronic properties via a thorough analysis of molecular orbitals.

A distinguished approach for chemisorption and electron transfer process in DSSCs is the Newns-Anderson Model [65,66]. This method is advanced for adsorbates on metal surfaces, and it gives a quantitative description of electron coupling between the surface and the adsorbate. Projected Density of States (PDOS) are used in this model, to analyze the electronic structure.

Adopting the fact that a single dye state (LUMO) interacts with the semiconductor (CB), we can get an estimation of the injection rate by simply examining the broadening of the density of states relative to the LUMO of the organic sensitizer. [ref] The Full Width at Half Maximum (FWHM) of the PDOS can give a quantitative portrait of lifetime broadening, $\hbar\Gamma$, and the electron lifetime τ can be approximated by $\tau(\text{fs})=658/\hbar\Gamma$. The obtained electron injection time can be directly compared to the experimental value [67].

In previous studies, it has been established that the standard B3LYP provides the correct alignment of the dye@SC energy levels, whereas long-range corrected hybrids deliver a more accurate prediction of the optical properties, but an unphysical descrip-

tion of the energetics. For this reason, both B3LYP and CAM-B3LYP functionals were used in extracting density of states (DOS), along with two different basis sets (6-31G* and 6-311G*).

Isodensity surface plots of projected Mulliken orbitals regarding HOMO and LUMO levels of the dye@SC interface is given in Table 4.6 and Table 4.7.

In Table 4.7, orbitals are extracted at B3LYP/6-31G* level of theory. Interface HOMO surfaces are quite similar to standalone dye electrostatic densities. The HOMO electrostatic densities do not accumulate on cyanoacrylic acceptor group, indicating a lower chance of charge recombination. Dye@SC_{LUMO} plots given in Table 4.7 and 4.8 are belong to LUMO orbitals which is mostly located on the dye, to see the dye contribution to the electronic structure. In these LUMO orbitals, electronic density is mostly located on the donor group, and has a little weight on the cyanoacrylic acceptor group. This situation is not favorable in terms of charge transfer.

The frontier molecular orbital (FMO) energies for DTP1 and DTP2 are given in Table 4.8 and Table 4.9. HOMO and LUMO levels of both isolated dyes and dye@SC interfaces are given together for comparison. Four different level of theories were used when extracting molecular orbital information. The average LUMO energy has been calculated for the dye@SC interface, and reported in Table 4.9 and Table 4.10 as $LUMO_{avg}$.

For each level of theory and for each organic sensitizer, HOMO level of dye@SC interface is found to be higher in energy when compared to isolated dye HOMO levels. For DTP1 and DTP2, HOMO levels of dye isolated dye molecules are lower in energy for DTP1. This stabilization of HOMO levels in DTP1 can also be observed in experimental results (See Table 4.1). According to the electrochemical device performance, the oxidation potentials of the dyes DTP1 and DTP2 were found to be 0.85 V and 0.68 V, respectively. Better oxidation capability of DTP1 can be seen in their HOMO level energies. This situation is also present for dye@semiconductor interfaces.

Table 4.6. Isodensity surface plots of Mulliken HOMO and LUMO orbitals of standalone dyes and dye@semiconductor interfaces.(Optimizations were held in PBE/DZP in gas phase, Mulliken orbitals were extracted at B3LYP/**6-31G*** level of theory, IEFPCM in dichloromethane)

	$\mathbf{Dye_{HOMO}}$	$\mathbf{Dye@SC_{HOMO}}$	$\mathbf{Dye_{LUMO}}$	$\mathbf{Dye@SC_{LUMO}}$
DTP1	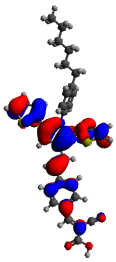	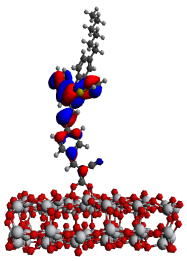	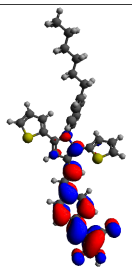	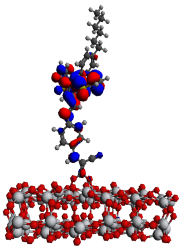
DTP2	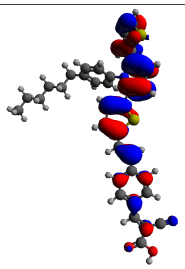	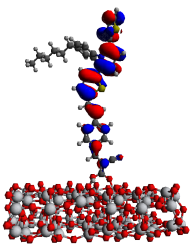	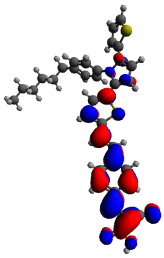	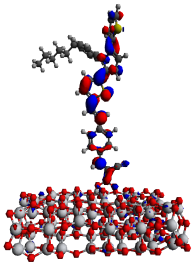

When the LUMO levels are analyzed, DTP2 gave lower results in energy, for each functional and basis set combination employed in the calculations. This is also true for average LUMO energies of the dye@semiconductor interfaces, with only one exception: CAM-B3LYP/6-31G* method resulted in 0.14 and 0.15 eV of average LUMO energy for DTP1 and DTP2, respectively. However, it is safe to say that, this results are quite similar. Going from DTP1 to DTP2, this destabilization of HOMO levels and stabilization of LUMO levels show that, the band gap of DTP1 is smaller compared to DTP2. This situation can also account for the better absorbance of DTP2 in the experimental results.

The broadening values are also given in Table 4.9 and 4.10. The higher value of this Lorentzian distribution indicated a better electronic coupling between dye LUMO level and the conduction band of the semiconductor.

Table 4.7. Isodensity surface plots of Mulliken HOMO and LUMO orbitals of standalone dyes and dye@semiconductor interfaces.(Optimizations were held in PBE/DZP in gas phase, Mulliken orbitals were extracted at B3LYP/**6-311G*** level of theory, IEF-PCM in dichloromethane)

	Dye$_{HOMO}$	**Dye@SC$_{HOMO}$**	**Dye$_{LUMO}$**	**Dye@SC$_{LUMO}$**
DTP1	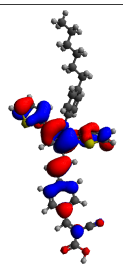	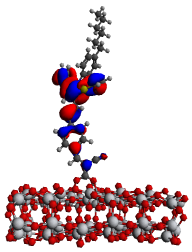	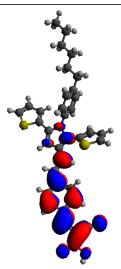	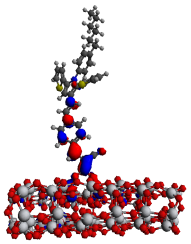
DTP2	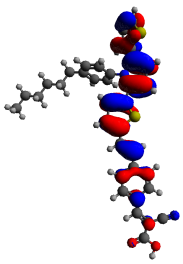	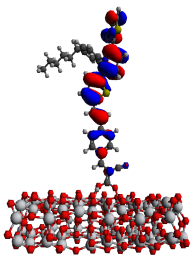	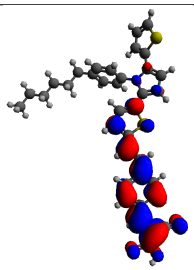	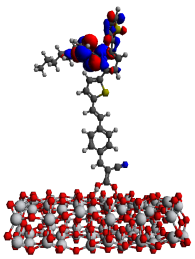

Table 4.8. Overview of Interface Frontier Molecular Orbital energies for DTP1 (eV), (Optimizations with **PBE**/DZP in gas phase)

DTP1	HOMO$_{dye}$	HOMO$_{dye@SC}$	LUMO$_{dye}$	LUMO$_{avg}$	Γ
B3LYP/6-31G*	-5.20	-5.03	-2.62	-1.47	0.62
B3LYP/6-311G*	-5.42	-5.23	-2.87	-2.77	0.12
CAM-B3LYP/6-31G*	-6.39	-6.19	-1.56	0.14	0.67
CAM-B3LYP/6-311G*	-6.61	-6.39	-1.83	-1.73	0.09

Table 4.9. Overview of Interface Frontier Molecular Orbital energies for DTP2 (eV)(Optimizations with **PBE**/DZP in gas phase)

DTP2	$\mathrm{HOMO_{dye}}$	$\mathrm{HOMO_{dye@SC}}$	$\mathrm{LUMO_{dye}}$	$\mathrm{LUMO_{avg}}$	Γ
B3LYP/6-31G*	-5.00	-4.88	-2.75	-1.53	0.66
B3LYP/6-311G*	-5.22	-5.06	-2.99	-2.94	0.08
CAM-B3LYP/6-31G*	-6.15	-6.00	-1.73	0.15	0.87
CAM-B3LYP/6-311G*	-6.37	-6.20	-1.99	-1.91	0.08

Table 4.10. Overview of Interface Frontier Molecular Orbital energies for DTP1 (eV), (Optimizations with **PBE-D3**/DZP in gas phase)

DTP1	$\mathrm{HOMO_{dye}}$	$\mathrm{HOMO_{dye@SC}}$	$\mathrm{LUMO_{dye}}$	$\mathrm{LUMO_{avg}}$	Γ
B3LYP/6-31G*	-5.20	-5.01	-2.62	-1.27	0.62
B3LYP/6-311G*	-5.42	-5.21	-2.87	-2.75	0.11
CAM-B3LYP/6-31G*	-6.39	-6.17	-1.56	0.11	0.67
CAM-B3LYP/6-311G*	-6.61	-6.37	-1.83	-1.70	0.07

Table 4.11. Overview of Interface Frontier Molecular Orbital energies for DTP2 (eV), (Optimizations with **PBE-D3**/DZP in gas phase)

DTP2	$\mathrm{HOMO_{dye}}$	$\mathrm{HOMO_{dye@SC}}$	$\mathrm{LUMO_{dye}}$	$\mathrm{LUMO_{avg}}$	Γ
B3LYP/6-31G*	-5.00	-4.88	-2.75	-1.50	0.66
B3LYP/6-311G*	-5.22	-5.08	-2.99	-2.94	0.08
CAM-B3LYP/6-31G*	-6.15	-6.02	-1.73	0.36	0.78
CAM-B3LYP/6-311G*	-6.37	-6.22	-1.99	-1.89	0.07

4.5. Periodic Approach

Up to this point, Density Functional Theory calculations were carried out with localized basis sets. As emphasized in Computational Methodology chapter, this type

of basis sets are centered on the nuclei and they are known to describe well the atoms. Modeling the semiconductor with atomistic DFT can be beneficial, especially if one wants to compare two systems. However, it would be more realistic if periodic nature of the surface was also taken into account in optimizations.

In its simplest terms, one can choose the basis functions as plane waves to acquire implicit periodicity in DFT calculations. In this sense, plane wave pseuodopotential approach is highly used in solid-state physics, to obtain an accurate description for the crystalline materials. The number of plane waves that are used in the calculations are described by an energy cufoff value. The pseudopotential approximation treats only the valence electrons, and assigns "potentials" for the core electrons.

In the case of dye and semiconductor interface, the grafting of the dye molecule onto the titanium dioxide semiconductor is a replicated system through lateral directions. This is why ab initio DFT calculations have also been performed in this work to include periodic nature of the solid photoanode.

As stated before, periodic DFT calculations were also done with PBE functional. For this part, $(TiO_2)_{144}$ cluster were used, as shown in Figure 4.9.

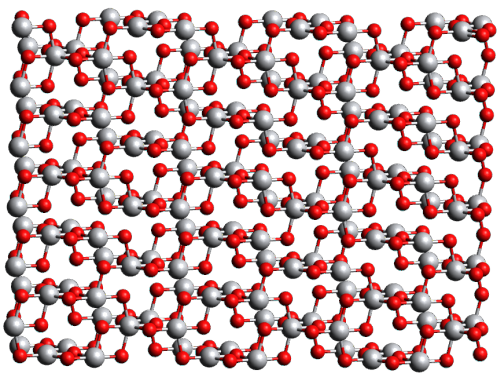

Figure 4.9. $(TiO_2)_{144}$ cluster

4.5.1. Structural Properties of Dye-TiO_2 Interfaces

In addition to atomistic DFT with localized basis sets, optimizations of dye and semiconductor interfaces have also been done with plane-wave DFT. A larger slab of titanium dioxide have been used for this system, with 144 titanium and 288 oxygen atoms. Anatase form is implemented to the semiconductor. PBE functional is used along with Projector Augmented Wave (PAW) pseudopotentials.

When anchoring the dyes onto the semiconductor, structural properties of isolated dyes are taken into account. Optimized structures of the interfaces are given in Figure **??** and **??**. DTP1, being a more symmetrical molecule was grafted onto the semiconductor at the center of $(TiO_2)_{144}$ slab. On the contrary, DTP2 was attached to the surface, in a way that maximizes the interaction between the organic dye and the surface. This is mainly due to the connectivity difference in donor and π-bridge parts of the two dye molecules.

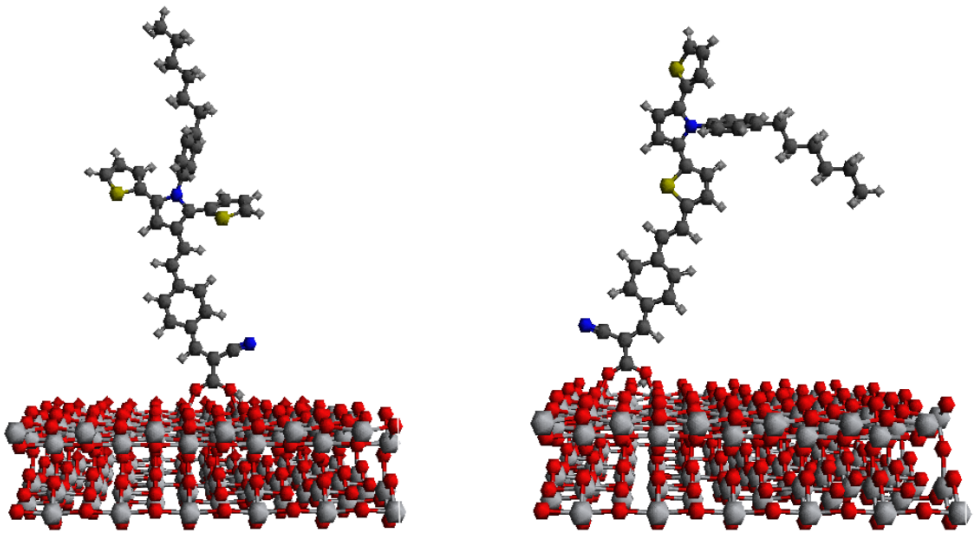

Figure 4.10. Optimized structures of dye@$(TiO_2)_{144}$ for DTP1 (right) and DTP2 (left).

4.5.1.1. Impact of Grafting on Dye Electronic Structure. In order to assess the changes upon grafting, HOMO-LUMO levels of the dyes are investigated. As mentioned in the previous section on Cluster Approach, the optimized dyes are cut from the surface and

compared to the isolated dye molecules, to pinpoint the changes. HOMO-LUMO levels are given in Figure 4.11.

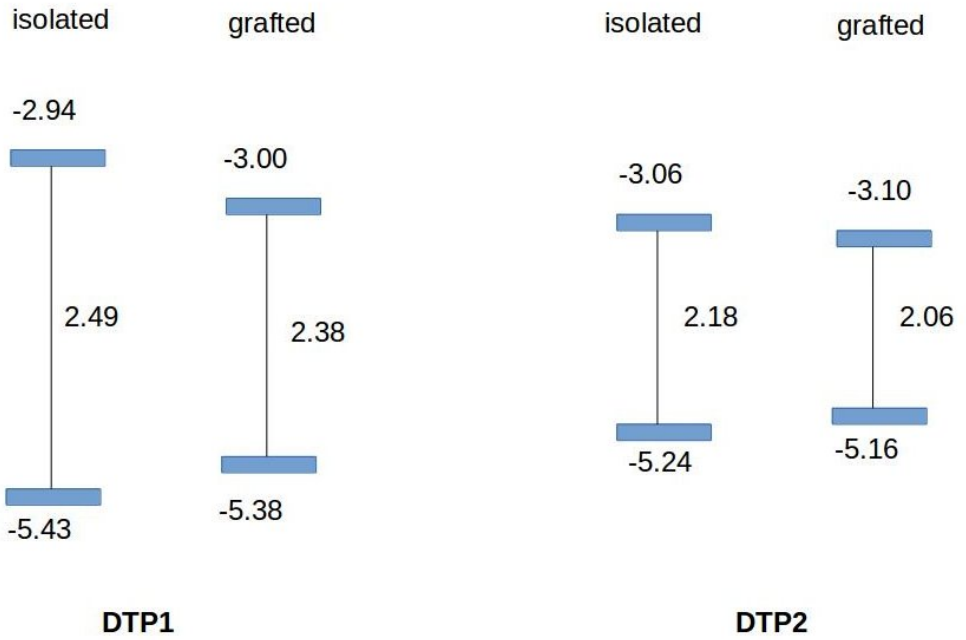

Figure 4.11. HOMO-LUMO levels for DTP1 and DTP2. (B3LYP/6-31+G(d,p), IEF-PCM in dichloromethane, energies in eV.)

At first glance, band gaps appear to be smaller for both DTP1 and DTP2, when they are attached to the semiconductor surface. Isolated DTP1 molecule has a bandgap of 2.49 eV, whereas grafted structure results in a stabilization. This situation is also true for DTP2, for which the bandgap values are 2.18 and 2.06 eV for isolated and grafted versions, respectively.

The superior performance of DTP2 in both absorbance and device performance can also be seen in Figure 4.11. Lower bandgap of DTP2 makes light-induced vertical transition more feasible. For both dyes, HOMO levels are destabilized, LUMO levels are stabilized when they are attached to the semiconductor surface.

4.5.2. Electronic Properties of Dye-TiO_2 Interfaces

After the optimizations were done via VASP code, a self-consistent single point run has been performed, to get the charge density and occupancies of states. In order to obtain a better picture, LORBIT=11 flag has been used to induce elemental decomposition of orbitals.

Total Density of States have been plotted in eV and given in Figure 4.12 and 4.13. The Fermi energies of the interfaces are found to be -3.49 eV for DTP1, -3.44 eV for DTP2. The calculated values for Fermi energy can be useful as a reference state, and do not depict a practical value in real temperatures.

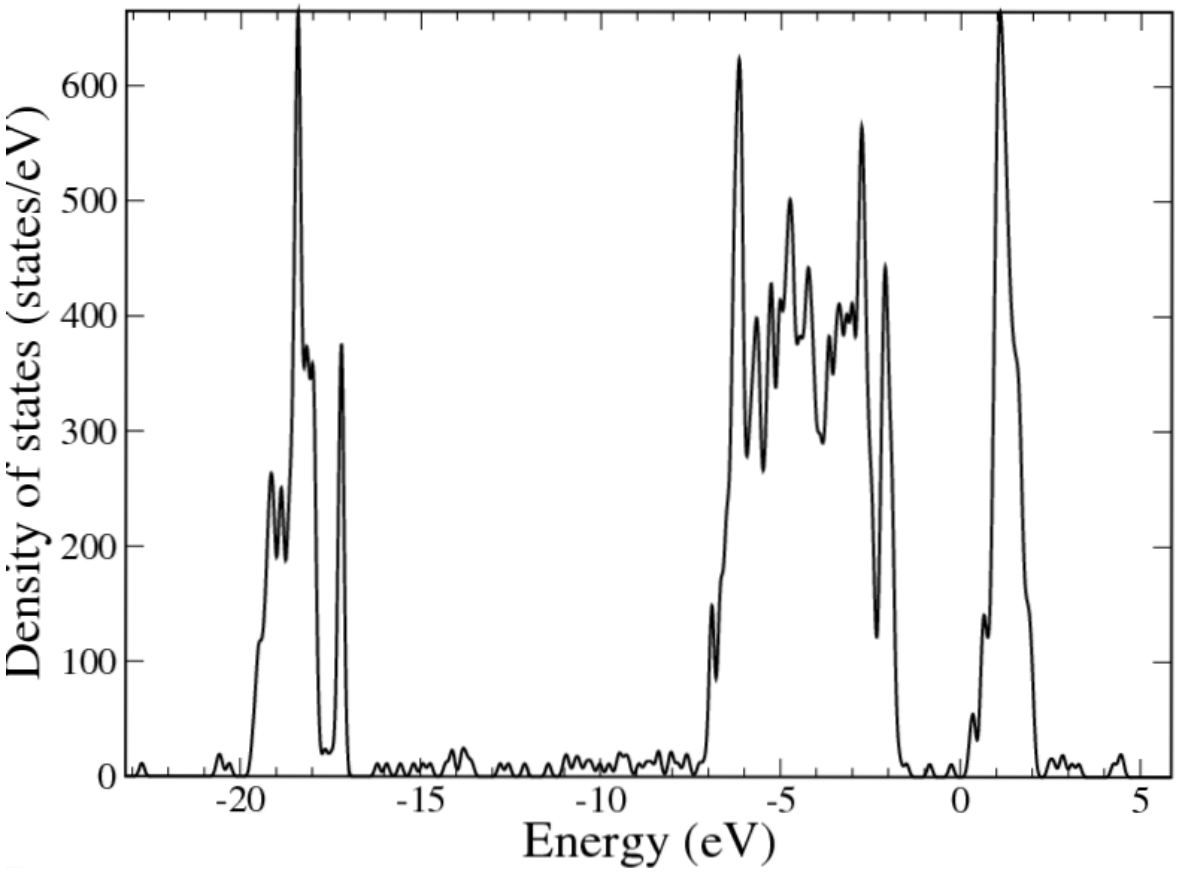

Figure 4.12. Total Density of States (DOS) for DTP1.

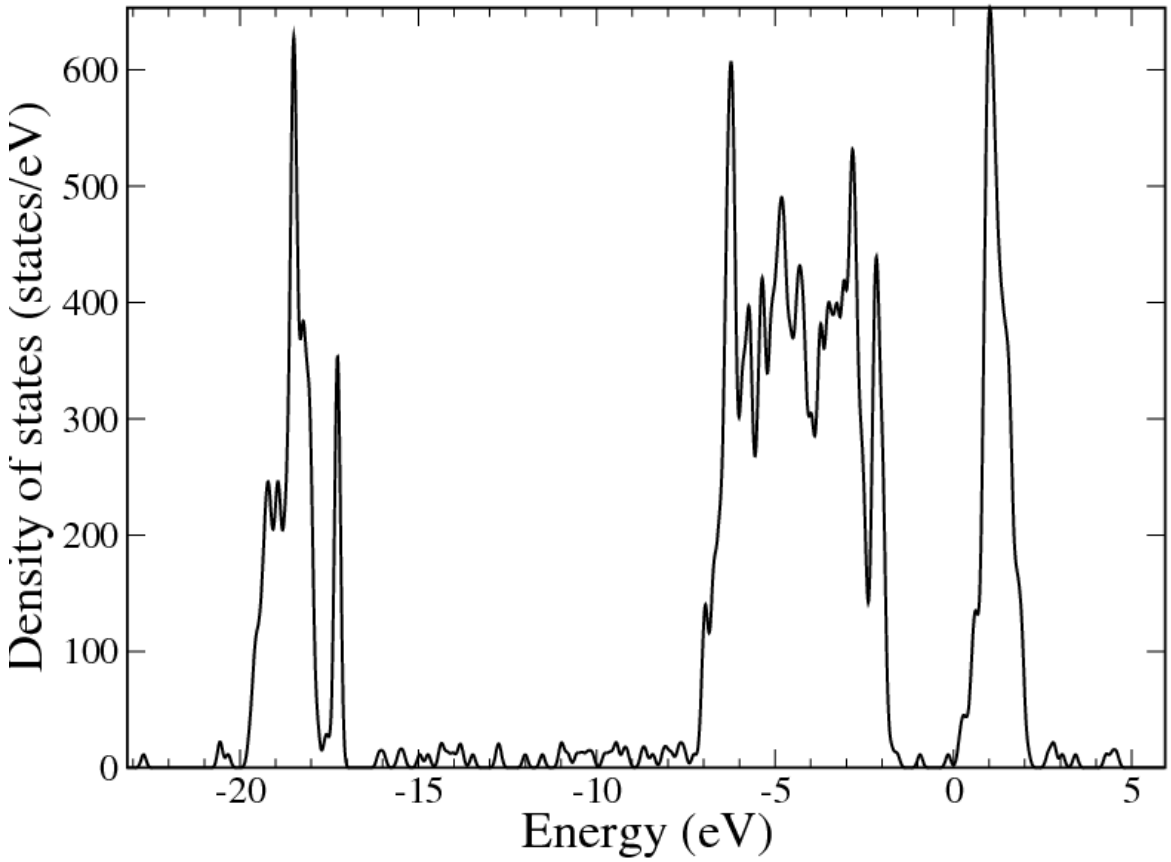

Figure 4.13. Total Density of States (DOS) for DTP2.

4.5.2.1. Partial Density of States. For periodically repeated systems, partial density of states are also calculated for carbon atoms. The extended conjugation of the dyes can be reflected through an analysis on density of states corresponding to carbons. The results can be seen in Figure 4.14 and 4.15.

A valuable information can be obtained from partial density of states, if this analysis would also be done on newly proposed structures. The fluctuations on certain orbitals can be monitored, and tuning the dye molecules may be achieved in a better way.

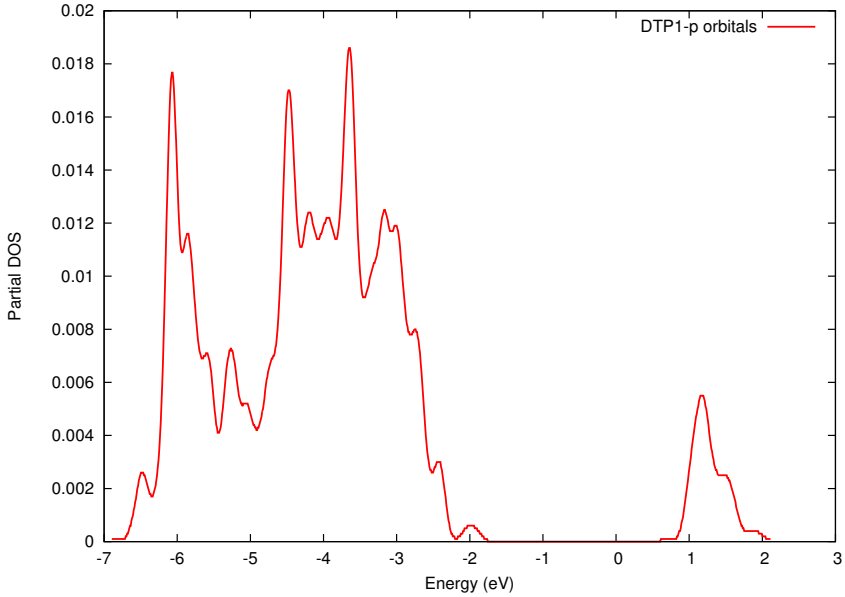

Figure 4.14. Partial Density of States (DOS) corresponding to Carbon atoms in DTP1.

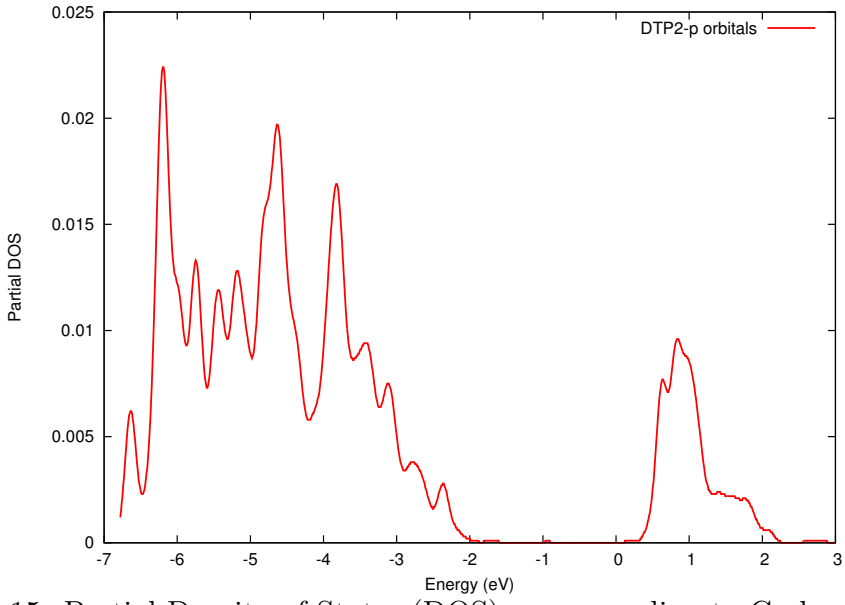

Figure 4.15. Partial Density of States (DOS) corresponding to Carbon atoms in DTP2.

4.6. Conclusion

In the second part of this thesis, modeling of Dye-sensitized Solar Cells (DSSCs) were established. Firstly, an investigation of isolated dye molecules were done. Fol-

lowing this, dyes are anchored onto the titanium dioxide semiconductor. Molecular orbitals were thoroughly studied, and different level of theories were employed during optimizations.

At the first glance, DTP2 molecule resulted in a superior performance according to both experimental and theoretical results. The red-shift in DTP2's absorption spectra were shown in each level of theory employed.

According to the theoretical analysis included in this thesis, the dyes suffer from lack of intrinsic charge transfer nature. In terms of isolated dye molecules, Natural Transition Orbital (NTO) analysis showed a great overlap between ground and excited state densities. The quantum mechanical descriptor ϕ_s values turned out to be very close to 1, indicating a local excited state nature. In addition, when these dyes were anchored onto the semiconductor, the LUMO levels which are mostly populated by dye orbitals, indicated an electron density located mainly on the donor part of the dye. This result is also in line with the fact that the dyes suffer from intramolecular charge transfer, since the most populated LUMO levels should be accumulated on the acceptor moiety of the sensitizer in order to ensure an effective charge injection.

To increase the intramolecular charge transfer, changes upon dye molecular structure should be proposed. In this sense, a longer π-spacer can be implemented in the dye structure, to assure better charge seperation. It is important to note that the outcome of tuning the dye molecule is not straight-forward, since electron-injection mechanism is not purely based on chemical intuition, but rather a subtle harmony between dye LUMO and titanium dioxide. The dye structure can be modified depending upon one's chemical intuition, however the intrinsic coupling of molecular orbitals will be affected by adsorption geometry, dye-binding modes and even dye aggregation mechanisms.

As future work, the oxidation potentials of the sensitizers and their electronic coupling with iodine redox mediator should also be investigated.

5. FUTURE REMARKS

DFT applications to systems in diverse subfields of computational sciences have been presented in this thesis. First part included a mechanistic modeling of a small organic reaction. Experimentally observed regioselective outcome in product ratios can be rationalized by conventional DFT calculations. Global hybrid B3LYP and meta-GGA M062X functionals resulted in an adequate portrayal of reaction mechanism, when combined with a meticulous analysis on transition states. As a future perspective, more accurate level of theories can be implemented on these systems, to account for scarcely selective nucleophiles.

Second part of this work demonstrates two different approaches to be implemented when atomistic modeling of Solar Cell mechanism is needed. To be able to propose improvements upon device performance, a new design can be suggested, involving a longer π-spacer and better donor substitutents. A similar theoretical investigation can be done on proposed dye structures to discover any changes in electronic structure and photophysical properties.

This thesis has been written from the point of enhancing predictive power of computational studies. As the computing power and capacity is increasing, it will become easier to accomplish more reliable results, and yet, tuning of chemical structures and anticipating the outcomes will be more prevalent.

REFERENCES

1. Ji, M.-K., Hertsen, D., Yoon, D. H., Eum, H., Goossens, H., Waroquier, M., ... , Ha H.-J., "Nucleophile-Dependent Regio- and Stereoselective Ring Opening of 1-Azoniabicyclo[3.1.0]hexane Tosylate", *Chemistry - An Asian Journal*, Vol. 9, pp. 1060-1067, 2014.

2. Choi, J., Yadav, N., and Ha, H.-J., "Preparation of a Stable Bicyclic Aziridinium Ion and Its Ring Expansion toward Piperidines and Azepanes", *Asian Journal of Organic Chemistry*, Vol. 6, pp. 1292-1307, 2017.

3. Boydas, E. B., Tanriver, G., D'Hooghe, M., H.-J. Ha, Van Speybroeck, V., and Catak, S., "Theoretical insight into the regioselective ring-expansions of bicyclic aziridinium ions", *Organic and Biomolecular Chemistry*, Vol. 16, pp. 796-806, 2018.

4. Sharmoukh, W., Attanzio, A., Busatto, E., Etienne, T., Carli, S., Monari, A., ... , Gros, P. C., "2,5-Dithienylpyrrole (DTP) as a donor component in DTP-π-A organic sensitizers: photophysical and photovoltaic properties", *RSC Advances*, Vol. 5, pp. 4041-4050, 2015.

5. Sengul, O., Boydas, E. B., Pastore, M., Sharmouk, W., Gros, P. C., Catak, S., and Monari, A., "Probing optical properties of thiophene derivatives for two-photon absorption", *Theoretical Chemistry Accounts*, Vol. 136, pp. 67-72, 2017.

6. Perdew, J. P., Burke K., and Ernzerhof, M., "Generalized Gradient Approximation Made Simple", *Physical Review Letters*, Vol. 78, pp. 3865-3868, 1996.

7. Becke, A., "B3LYP", *The Journal of Chemical Physics*, Vol. 98, pp. 5648-5652, 1993.

8. Yanai, T., Tew, D. P., and Handy, N. C., "A new hybrid exchange-correlation functional using the Coulomb-attenuating method (CAM-B3LYP)", *Chemical Physics*

Letters, Vol. 393, pp. 51-57, 2004.

9. Zhao, Y. and Truhlar, D. G.., "M062X and M06", *Theoretical Chemistry Accounts*, Vol. 120, pp. 215-241, 2008.

10. Ditchfield, R., Hehre, W. J., and Pople, J. A., "Self Consistent Molecular Orbital Methods. IX. An Extended Gaussian Type Basis for Molecular Orbital Studies of Organic Molecules", *The Journal of Chemical Physics*, Vol. 54, pp. 724-728, 1971.

11. Mennucci, B., "Polarizable continuum model", *Computational Molecular Science*, Vol. 2, pp. 386–404, 2012.

12. Etienne, T., "Probing the locality of excited states with linear algebra", *Journal of Chemical Theory and Computation*, Vol. 11, pp. 1692-1699, 2015

13. Etienne, T., Assfeld, X., and Monari, A., "New insight into the topology of excited states through detachment/attachment density matrices-based centroids of charge", *Journal of Chemical Theory and Computation*, Vol. 10, pp. 3906-3914, 2014.

14. Padwa, A., "Epoxides and aziridines: a mini review", *Journal of Physical Chemistry*, Vol. 99, pp. 2224-2235, 1995.

15. Gabriel, S., "Ueber eine Darstellungsweise primärer Amine aus den entsprechenden Halogenverbindungen", *Berichte der deutschen chemischen Gesellschaft*, Vol. 2, pp. 2224–2236, 1888.

16. Sweeney, J. B., "Aziridines: epoxides' ugly cousins?", *Chemical Society Reviews*, Vol. 31, pp. 247-258, 2002.

17. Yudin, A. K., *Aziridines and Epoxides in Organic Synthesis*, Wiley-VCH, Boston, 2006.

18. Li, X., Chen, N., and Xu, J., "An improved and mild wenker synthesis of

aziridines", *Synthesis*, Vol. 20, pp. 3423-3428, 2010.

19. Denolf, B., Leemans, E, and De Kimpe, N., "Asymmetric synthesis of aziridines by reduction of N-tert-butanesulfinyl α-chloro imines", *Journal of Organic Chemistry*, Vol. 72, pp. 3211–3217, 2007.

20. Hu, X. E., "Nucleophilic ring opening of aziridines", *Tetrahedron*, Vol. 60, pp. 2701-2743, 2004.

21. Padwa, A., *Comprehensive Heterocyclic Chemistry III*, Elsevier, Cambridge, 2008.

22. Kim, Y, Ha, H.-J., Yun, S. K., and Lee, W. K., "The preparation of stable aziridinium ions and their ring-openings", *Chemical Communications*, Vol. 36, p. 4363, 2008.

23. D'hooghe, M., Van Speybroeck, V., Waroquier, M., and De Kimpe, N., "Regio- and stereospecific ring opening of 1,1-dialkyl-2-(aryloxymethyl)aziridinium salts by bromide", *Chemical Communications*, Vol. 8, pp. 1554-1556, 2006.

24. Anxionnat, B., Robert, B., George, P., Ricci, G., Domingo, G. P., and Cossy J., "Ring expansion of cyclic β-amino alcohols induced by diethylaminosulfur trifluoride: Synthesis of cyclic amines with a tertiary fluorine at C3", *Journal of Organic Chemistry*, Vol. 77, pp. 6087-6099, 2012.

25. Nonn, M., Remete, A. M., Fülöp, F., and Kiss, L., "Recent advances in the transformations of cycloalkane-fused oxiranes and aziridines", *Tetrahedron*, Vol. 73, pp. 5461-5483, 2017.

26. Burns, L. A., Vázquez-Mayagoitia, A., Sumpter, B. G., and Sherrill C. D., "Density-functional approaches to noncovalent interactions: A comparison of dispersion corrections (DFT-D), exchange-hole dipole moment (XDM) theory, and specialized functionals", *Journal of Chemical Physics*, Vol 134, pp. 1-10, 2011.

27. Marom, N., Tkatchenko, A., Rossi, M., Gobre, V., Hod, O., Scheffler, M., and Kronik, L., "Dispersion interactions with density-functional theory: Benchmarking semiempirical and interatomic pairwise corrected density functionals", *Journal of Chemical Theory and Computation*, Vol. 7, pp. 3944-3951, 2011.

28. Grimme, S., "Semiempirical GGA-type density functional constructed with a long-range dispersion correction", *Journal of Computational Chemistry*, Vol. 27, pp. 1787-1799, 2006.

29. Grimme, S., Antony, J., Ehrlich, S., and Krieg, H., "A consistent and accurate ab initio parametrization of density functional dispersion correction (DFT-D) for the 94 elements H-Pu", *Journal of Chemical Physics*, Vol. 132, p. 154, 2010.

30. Lynch, B., Fast, P., Harris, M., and Truhlar, D. G., "Adiabatic Connection for Kinetics", *The Journal of Physical Chemistry A*, Vol. 104, pp. 4811-4815, 2000.

31. Boese, A. D., and Martin, J. L., "Development of density functional for thermochemical kinetics", *Journal of Chemical Physics*, Vol. 121, pp. 3405-3416, 2004.

32. Frisch, M. J.; Trucks, G. W.; Schlegel, H. B.; Scuseria, G. E.; Robb, M. A.; Cheeseman, ... , Fox, D. J., *Gaussian 09, Revision E.01*, Gaussian, Inc., Wallingford CT, 2009.

33. Gonzalez, C., and Schlegel, H. B., "An improved algorithm for reaction path following", *The Journal of Chemical Physics*, Vol. 90, pp. 2154-2161, 1989.

34. Gonzalez, C., and Schlegel, H. B., "Reaction path following in mass-weighted internal coordinates", *Journal of Physical Chemistry*, Vol. 94, pp. 5523-5527, 1990.

35. Chipman, D. M., "Comparison of solvent reaction field representations", *Theoretical Chemistry Accounts*, Vol 107, pp. 80-89, 2002.

36. Takano, Y., and Houk, K.N., "Benchmarking the conductor-like polarizable con-

tinuum model (CPCM) for aqueous solvation free energies of neutral and ionic organic molecules", *Journal of Chemical Theory and Computation*, Vol. 1, pp. 70-77, 2005.

37. Zeist, W. J., and Bickelhaupt, F. M., "The activation strain model of chemical reactivity", *Organic & Biomolecular Chemistry*, Vol. 8, p. 3118, 2010.

38. Wolters, L. P. and Bickelhaupt, F. M., "The activation strain model and molecular orbital theory", *Computational Molecular Science*, Vol. 5, pp. 324–343, 2015.

39. Bickelhaupt, F. M. and Houk, K.N., "Analyzing Reaction Rates with the Distortion/Interaction-Activation Strain Model", *Angewandte Chemie International Edition*, Vol. 56, pp. 10070–10086, 2017.

40. Bostan, I., Gheorghe, A. V., Dulgheru, V., Sobor, I., Bostan, V. and Sochirean, A., *Resilient Energy Systems: Renewables: Wind, Solar, Hydro.* 2012.

41. Kamat, P. V., "Meeting the clean energy demand: Nanostructure architectures for solar energy conversion", *Journal of Physical Chemistry C*, Vol 111, pp. 2834-2860, 2007.

42. Blandford, R. and Watkins, M., "This Month in Physics History: April 25, 1954: Bell Labs Demonstrates the First Practical Silicon Solar Cell", *APS News*, Vol 18, pp. 17-20, 2009.

43. Mints, P., "Photovoltaic crystalline and thin film capacity, production, shipments and inventory, 1982-2019; Past and future trends", In *2015 IEEE 42nd Photovoltaic Specialist Conference, PVSC 2015*, 2015.

44. Kojima, A., Teshima, K., Shirai, Y., and Miyasaka, T., "Organometal Halide Perovskites as Visible- Light Sensitizers for Photovoltaic Cells", *Journal of American Chemical Society*, Vol. 131, pp. 6050-6051, 2009.

45. Grancini, G., Roldán-Carmona, C., Zimmermann, I., Mosconi, E., Lee, X., Martineau, D., Narbey, S., Oswald, F., De Angelis, F., Graetzel, M., and Nazeeruddin, M. K., "One-Year stable perovskite solar cells by 2D/3D interface engineering", *Nature Communications*, Vol. 8, p. 15684, 2017.

46. O'Regan, B. and Grätzel, M., "A low-cost, high-efficiency solar cell based on dye-sensitized colloidal TiO_2 films", *Nature*, Vol. 353, pp. 737-740, 1991.

47. Anders, H., Gerrit, B., Licheng, S., Lars, K., and Pettersson, H., "Dye-Sensitized Solar Cells", *Chemistry Reviews*, Vol. 110, pp. 6595-6663, 2010.

48. Klamt, A., "Conductor-like screening model for real solvents: A new approach to the quantitative calculation of solvation phenomena", *Journal of Physical Chemistry*, Vol. 99, pp. 2224-2235, 1995.

49. Kresse, G., and Furthmüller, J., "Efficient iterative schemes for ab initio total energy calculations using a plane wave basis set", *Physical Reviews B*, Vol. 54, pp. 11169-11170, 1996.

50. Ronca, E., Pastore, M., Belpassi, L., and Tarantelli, F., "Influence of the dye molecular structure on the TiO_2 conduction band in Dye-sensitized solar cells: Disentangling charge transfer and electrostatic effects", *Energy % Environmental Sciences*, Vol. 6, pp. 183-193, 2012.

51. Rana, T. H., Solanki, A. K., Skomski, R. and Kashyap, A., "Ab-initio study of free standing TiO_2 clusters: Stability and magnetism", *Journal of Applied Physics*, Vol. 113, pp. 2013-2016, 2013.

52. Da Chai, J., and Head-Gordon, M., "Long-range corrected hybrid density functionals with damped atom-atom dispersion corrections", *Physical Chemistry Chemical Physics*, Vol. 10, pp. 6615-6620, 2008.

53. Peach, M., Benfield, P., Helgaker, T., and Tozer, T., "Excitation energies in density

functional theory: An evaluation and a diagnostic test", *The Journal of Chemical Physics*, Vol. 128, pp. 1-9, 2008.

54. Jacquemin, D., Wathelet, V., Perpète, E., and Adamo, C., "Extensive TD-DFT benchmark: Singlet-excited states of organic molecules", *Journal of Chemical Theory and Computation*, Vol. 5, pp. 2420-2435, 2009.

55. Lü, X., Xu, X., Wang, N., Zhang, Q., Ehara, M., and Nakatsuji, H., "Cluster modeling of metal oxides: how to cut out a cluster?", *Chemical Physics Letters*, Vol. 291, pp. 445-452, 1998.

56. Gambogi, J., "Mineral Commodity Summaries 2015", *U.S. Geological Survey*, p. 128, 2015.

57. Hagfeldt, A., and Grätzel, M., "Light-Induced Redox Reactions in Nanocrystalline Systems", *Chemical Reviews*, Vol. 95, pp. 49-68, 1995.

58. Luttrell, T., Halpegamage, S., Tao, J., Kramer, A., Sutter, E., and Batzill, M., "Why is anatase a better photocatalyst than rutile? - Model studies on epitaxial TiO_2 films", *Scientific Reports*, 4, 2015.

59. Pastore, M., and De Angelis, F., "Computational modelling of TiO_2 surfaces sensitized by organic dyes with different anchoring groups: adsorption modes, electronic structure and implication for electron injection/recombination", *Physical Chemistry Chemical Physics*, Vol. 14, pp. 920–928, 2012.

60. Srinivas, K., Yesudas, K., Bhanuprakash, K., Jayathirtha Rao, R., and Giribabu, L., "A combined experimental and computational investigation of anthracene based sensitizers for DSSC: Comparison of cyanoacrylic and malonic acid electron withdrawing groups binding onto the TiO_2 anatase (101) surface", *Journal of Physical Chemistry C*, Vol. 113, pp. 20117-20126, 2009.

61. León, C.-P., Kador, L., Peng, B., and Thelakkat, M., "Characterization of the

adsorption of Ru-bpy dyes on mesoporous TiO_2 films with UV-Vis, Raman, and FTIR spectroscopies", *Journal of Physical Chemistry B*, Vol. 117, pp. 8723-8730, 2006.

62. Pastore, M., and De Angelis, F., "Aggregation of organic dyes on TiO_2 in dye-sensitized solar cells models: An Ab initio investigation", *ACS Nano*, Vol. 4, pp. 556-562, 2010.

63. Chen, P., Yum, J.-H., De Angelis, F., Mosconi, E., Fantacci, S., Moon, S., ... , Grätzel, M., "High open-circuit voltage solid-state dye-sensitized solar cells with organic dye", *Nano Letters*, Vol. 9, pp. 2487-2492, 2009.

64. Schnadt, P., Brühwiler, A., Patthey, L., O'Shea, J. N., Södergren, S., Odelius, M., Ahuja, R., Karis, O., Bässler, M., Persson, P., Slegbahn, H., Lunell, S., and Mårtensson, N., "Experimental evidence for sub-3-fs charge transfer from an aromatic adsorbate to a semiconductor", *Nature*, Vol. 418, pp. 620-623, 2002.

65. Oliveira, L. N., and Yoshida, M., "Adsorbate spectral density for a generalized Anderson-Newns Hamiltonian", *Journal of Physics: Condensed Matter*, 5(33 A), 1993.

66. Martin-Rodero, A., Flores, F., Baldo, M., and Pucci, A., "A new solution to the Anderson-Newns Hamiltonian of chemisorption", *Solid State Communications*, Vol. 44, pp. 911-914, 1982.

67. Persson, P., Lundqvist, M., Ernstorfer, R., Goddard, W., and Willig, F., "Quantum chemical calculations of the influence of anchor-cum-spacer groups on femtosecond electron transfer times in dye-sensitized semiconductor nanocrystals", *Journal of Chemical Theory and Computation*, Vol. 2, pp. 441-451, 2006.

APPENDIX A: ARTICLES

A.1. Theoretical Insight Into the Regioselective Ring-Expansions of Bicyclic Aziridinium Ions

A full-text version of the article regarding part I is given in this section.

Organic & Biomolecular Chemistry

PAPER

View Article Online
View Journal | View Issue

Cite this: *Org. Biomol. Chem.*, 2018, **16**, 796

Theoretical insight into the regioselective ring-expansions of bicyclic aziridinium ions†

Esma B. Boydas,[a] Gamze Tanriver,[a] Matthias D'hooghe,[b] Hyun-Joon Ha,[c] Veronique Van Speybroeck[d] and Saron Catak *[a,d]

Received 7th September 2017,
Accepted 2nd January 2018

DOI: 10.1039/c7ob02253k

rsc.li/obc

Transient bicyclic aziridinium ions are known to undergo ring-expansion reactions, paving the way to functionalized nitrogen-containing heterocycles. In this study, the regioselectivity observed in the ring-expansion reactions of 1-azoniabicyclo[*n*.1.0]alkanes was investigated from a computational viewpoint to study the ring-expansion pathways of two bicyclic systems with different ring sizes. Moreover, several nucleophiles leading to different experimental results were investigated. The effect of solvation was taken into account using both explicit and implicit solvent models. This theoretical rationalization provides valuable insight into the observed regioselectivity and may be used as a predictive tool in future studies.

Introduction

There is a wide interest in aziridines due to their outstanding synthetic applications as end-products and particularly as intermediates.[1,2] The release of ring strain in aziridines serves as a strong driving force in their ring-opening reactions, giving rise to a wide variety of functionalized nitrogen-containing target compounds.[3–5] Aziridine ring-opening reactions are mostly governed by the substituents on the ring nitrogen atom.[6,7] If the aziridine ring is endowed with an electron-withdrawing substituent at the ring nitrogen, it is classified as an "activated-aziridine".[8–11] Conversely, the introduction of an electron-donating (alkyl) substituent at nitrogen results in a more inert aziridine ring, which is often referred to as a "non-activated aziridine" (Scheme 1a)[12–15] that requires activation with a suitable electrophile in order to undergo ring-opening (Scheme 1b).[16] For example, *N*-alkylation of non-activated aziridines provides reactive aziridinium ions prone to undergo ring opening. Although such activated aziridinium ion intermediates have not been easily isolated –only a few examples of isolated (monocyclic) aziridinium salts have been reported[17]– their formation has usually been detected spectroscopically.[18,19]

Monocyclic aziridinium ions, generated through *N*-alkylation with an external alkyl halide, could undergo ring-opening reactions with a suitable nucleophile to afford either α-branched amines *via* an attack on the unsubstituted carbon or β-branched amines through an attack on the more hindered carbon, as shown in Scheme 2a.[20,21]

In addition to monocyclic structures, bicyclic aziridinium ions can be generated in an intramolecular S_N2 fashion, from which ring-opening reactions would result in ring-expansions and lead to azaheterocyclic products,[22,23] as shown in Scheme 2b. Several studies reporting on the formation of bicyclic aziridinium moieties and their synthetic applications are available.[15,24,25] The ring-expansion routes of bicyclic aziridinium ions mainly depend on their ring-size, the nature of the aziridinium substituents and the identity of the nucleo-

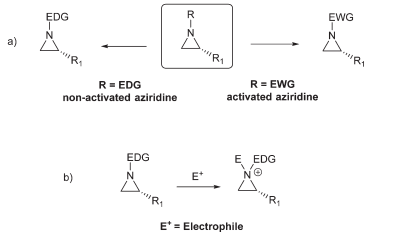

Scheme 1 (a) Activated *versus* non-activated aziridines and (b) activation of non-activated aziridines.

[a]*Bogazici University, Department of Chemistry, Bebek, 34342 Istanbul, Turkey. E-mail: saron.catak@boun.edu.tr*
[b]*Department of Sustainable Organic Chemistry and Technology, Faculty of Bioscience Engineering, Ghent University, Coupure Links 653, 9000 Ghent, Belgium*
[c]*Department of Chemistry, Hankuk University of Foreign Studies, Yongin, 17035, Korea*
[d]*Center for Molecular Modeling, Ghent University, Technologiepark 903, 9052 Zwijnaarde, Belgium*

†Electronic supplementary information (ESI) available. See DOI: 10.1039/c7ob02253k

Figure A.1. Article 1.

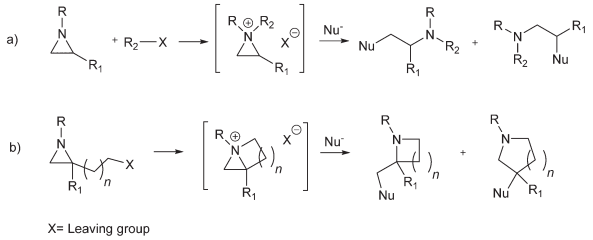

Scheme 2 Schematic representation of (a) monocyclic and (b) bicyclic aziridinium ion formation and their ring-opening reactions by nucleophiles.

phile, which all contribute to determining the kinetic and thermodynamic properties of the reaction.

Recently, the formation of 1-azoniabicyclo[3.1.0]hexane tosylates **1** and their ring-expansion upon treatment with various nucleophiles in acetonitrile have been investigated by Ha and coworkers.[25] This ring-expansion, as shown in Scheme 3, resulted in either piperidines **3** or pyrrolidines **4**, depending on the site of nucleophile attack. While ring-opening at the hindered aziridinium carbon *via* **path i** affords piperidines **3**, an attack on the unhindered carbon (through **path ii**) leads to pyrrolidines **4**. In Ha's work,[25] (Scheme 3) the cyanide nucleophile was shown to induce an attack on the less hindered carbon and exclusively yield pyrrolidines **4**, whereas chloride preferred the more hindered path and led to piperidines **3** as seen in Table 1.

More recently, the syntheses of 1-azoniabicyclo[4.1.0]heptane tosylates **5** and their ring-expansion products were proposed by Choi *et al.*[26] The subsequent ring-expansion reactions, conducted with different nucleophiles, resulted in either azepanes **7** by way of the more-hindered **path i** or piperidines **8** by following **path ii**, as depicted in Scheme 4. Once again, cyanide was shown to attack the less hindered position, and mainly gave rise to piperidines **8** in an 8 : 92 ratio (Table 1). There seems to be less of a distinction between the two routes for azide and amine attacks on the aziridinium ion **5**, with product ratios of 59 : 41 and 65 : 35, respectively, slightly in favor of the more hindered pathway leading to azepane **7** (Table 1).

Table 1 Ring-expansion reactions of 1-azoniabicyclo[3.1.0]hexane tosylates **1**[25] and 1-azoniabicyclo[4.1.0]heptane tosylates **5**[26] with different nucleophiles in CH_3CN

Nucleophile	Substrate	T [°C]	Yield (%)	**3**/**4** ratio	**7**/**8** ratio
nBu$_4$N$^+$**CN**$^-$	Aziridinium **1**	25	89	0 : 100	—
Na**N**$_3$	Aziridinium **1**	25	89	36 : 64	—
Ts**Cl**	Aziridinium **1**	25	88	100 : 0	—
Na**CN**	Aziridinium **5**	25	92	—	8 : 92
Na**N**$_3$	Aziridinium **5**	25	94	—	59 : 41
Bn**NH**$_2$	Aziridinium **5**	25	87	—	65 : 35

As seen from the product ratios in the reactions mentioned above, the factors governing the regioselectivity in ring-expansion of 1-azoniabicyclo[n.1.0]alkanes are still unclear. There are many factors that contribute to the selectivity, such as the effect of the solvent, and the nature of the nucleophiles and electrophiles.[27] The present study aims at focusing on these two recent examples, involving the formation and interception of 1-azoniabicyclo[3.1.0]hexane tosylates **1** and 1-azoniabicyclo [4.1.0]heptane tosylates **5**, and to computationally explore the two competing reaction routes in an effort to elucidate the underlying elements that determine the preferred path in the ring expansions of bicyclic aziridiniums and lead to the experimental product distributions. Both aziridinium ions **1** and **5** bear the same *N*-substituent, allowing for a clear comparison of the effect of the ring size and the nature of the nucleophile.

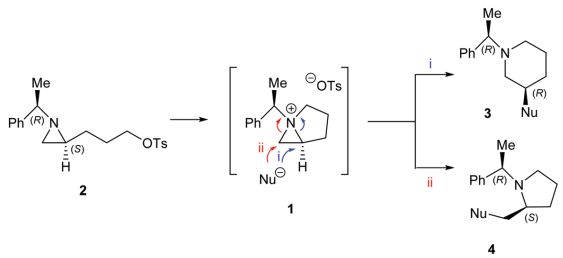

Scheme 3 The formation of 1-azoniabicyclo[3.1.0]hexane tosylate **1** and its corresponding ring expansion reaction by a nucleophile.[25]

Figure A.1. Article 1. (cont.)

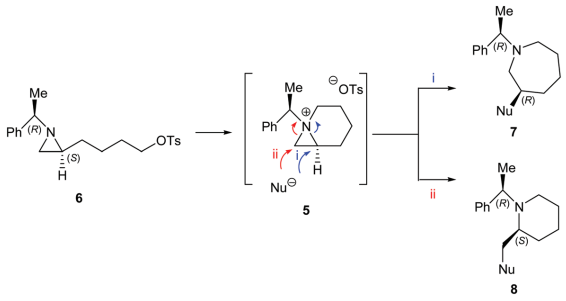

Scheme 4 The formation of 1-azoniabicyclo[4.1.0]heptane tosylate **5** and its corresponding ring expansion reaction by a nucleophile.

The theoretical study of regioselectivity in complex reaction media as studied herein is quite challenging, as recently reviewed by Houk and coworkers.[28] An in-depth understanding of the transition state structures and an accurate assessment of their energies are of utmost importance to make a distinction between the various competitive routes in mechanistic studies. Thus, the energy differences between the competing pathways for both the 1-azoniabicyclo[*n*.1.0]alkane systems under study herein are of major interest and a suitable modeling approach is pertinent for attaining reliable results and assessing the factors influencing the experimental results. The ring-expansion of 1-azoniabicyclo[3.1.0]hexane tosylates **1** has previously been analyzed by some of the present authors in a joint experimental/computational study.[25] Herein, it will be revisited to account for dispersion interactions, which are well known to significantly affect the outcome of organic reactions.[29–31] The aim is to aid the experimental strategy by shedding light on the factors affecting the regioselectivity in ring-expansions of bicyclic aziridiniums. Moreover, the ultimate goal is to establish a computational methodology able to predict the outcome of future studies on ring-expansions of these ions.

Computational methodology

To gain insight into the regioselective preference of different nucleophiles towards the ring opening of 1-azoniabicyclo [3.1.0]hexane tosylates **1** and 1-azoniabicyclo[4.1.0]heptane tosylates **5**, a thorough Density Functional Theory (DFT) study was performed. All reactants, transition states (TS) and products were optimized at the B3LYP[32] and M06-2X[33] levels of theory utilizing the 6-31+G(d,p) and 6-31++G(d,p) basis sets. Conformational analysis was performed on all reactants, transition states and products in an effort to identify the most plausible conformers. The semi-empirical dispersion correction scheme DFT-D,[34,35] developed by Grimme, was used to account for dispersive and non-covalent interactions, as an add-on term to B3LYP energies, allowing for a comparison between M06-2X and B3LYP-D performance. Energy refinements were performed at MPW1K[36] and BMK[37] levels of theory, and the 6-31+G(d,p) basis set. These functionals were specifically designed for predicting accurate barrier heights and kinetics.

All calculations were carried out with the Gaussian 09 software package.[38] Free energies were reported in kJ mol^{-1} at 1 atm and 298 K. Normal mode analysis was performed to identify the nature of the ground state and transition state structures. Furthermore, Intrinsic Reaction Coordinate (IRC)[39,40] calculations were used to verify the transition state geometries.

It has been shown that solvent effects cannot be neglected in the regioselective ring opening of aziridinium ions.[14,41,42] Hence, the possible pathways under study were modeled with several different levels of solvation. The simplest method for taking into account the solvent environment consists in using a continuum model, where the solute is placed in a continuous medium characterized by a dielectric constant.[43,44] Two well-known implicit solvation methods based on the Polarizable Continuum Model (PCM), namely IEFPCM and CPCM, were used.[45,46] PCM models surely provide a better environment than gas phase calculations; however, they still are not able to take into account possible explicit interactions with solvent molecules. In addition to the implicit solvent approach, a discrete solvent model (also called the 'supermolecule' approach or microsolvation)[27,47–51] was used to solvate the bicyclic aziridinium ions and the attacking nucleophiles in their corresponding transition states. The number of explicit solvent molecules was determined by the value at which the coordination solvation energy converged and was incorporated from a previous study of a similar system.[25] To also elucidate potential long-range interactions, systems containing two explicit solvent (acetonitrile) molecules were additionally placed in a dielectric continuum in an approach known as a mixed implicit/explicit model.[51–53]

In an effort to further understand the regioselectivity in the ring-expansion reactions of bicyclic aziridinium ions, the distortion–interaction model, also known as the Activation-Strain Model (ASM), was used.[54–56] The ASM model is very proficient

Figure A.1. Article 1. (cont.)

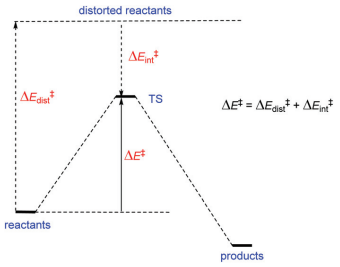

Scheme 5 Schematic illustration of the distortion–interaction model.[54–56]

in differentiating between the favorable interactions as well as the unfavorable distortions occurring in the transition state structure.[57,58] This model partitions the electronic activation energy $\Delta E^{\ddagger}$ into distortion energy ($\Delta E_{dist}^{\ddagger}$) and interaction energy ($\Delta E_{int}^{\ddagger}$) (Scheme 5). Distortion energy represents the strain caused by deformation of the reactants in the course of the transition state and is determined by the rigidity of the reactants. If the reaction coordinate entails a high reorganization within/among the reactants, distortion energy would be high. On the other hand, interaction energy stems from a stabilizing interaction between reactants, and is associated with how well the reactants are oriented towards each other. In most cases, $\Delta E_{int}^{\ddagger}$ is negative and stabilizing, and $\Delta E_{dist}^{\ddagger}$ is positive and destabilizing.[27,47,48,55,59,60]

Results and discussion

In an effort to elucidate the factors governing the selectivity in ring-expansion reactions of 1-azoniabicyclo[*n*.1.0]alkane systems, the two possible routes in Schemes 3 and 4 were computationally explored with several different nucleophiles, as summarized in Table 1. In particular, the interaction of CN^-, N_3^-, and Cl^- with the aziridinium ion **1** was investigated, as well as the reaction of CN^-, N_3^-, and NH_2^- for the ring-expansion reactions of the aziridinium ion **5**. The hybrid GGA functional B3LYP was used for optimizations, as well as the meta-GGA M06-2X, which is known to perform well with non-covalent interactions and produce accurate thermochemical data.[33,61]

Transition state structures for all nucleophiles are shown in Fig. 1 for both systems. Explicit acetonitrile molecules were placed in a consistent manner around the attack sites; the positive dipole of solvent molecules interacts with nucleophiles at a distance of 2.0–3.0 Å. Counter ions of the nucleophiles and the tosylate ion were not included in the calculations, since they are unlikely to have a close association with the aziridinium ion in the presence of such a high-dielectric solvent. It is important to note that, while nucleophile attack distances are similar for both pathways in the case of aziridinium **1**, they significantly differ for aziridinium **5**, indicating the importance of ring size in nucleophile-induced ring expansions of bicyclic aziridinium ions. Moreover, taking into account the C–N distances in the aziridinium ions, the extent of reaction is shown to be somewhat similar for pathways in the case of aziridinium ion **1**. However, in the aziridinium ion **5** case, the transition state leading to the unhindered pathway (**path ii**) is clearly much more reactant-like (see shorter aziridinium C–N distances) than their **path i** counterparts, which have much larger C–N distances, indicating a later TS. A more elaborate analysis of the critical distances will be given in the following section.

Bond elongation analysis

The reaction mechanism has been further investigated by calculating the variation of critical distances along different routes for 1-azoniabicyclo[*n*.1.0]alkanes **1** and **5**. Bond elongation percentages were calculated with respect to the nitrogen–carbon distances in bicyclic aziridinium ions **1** and **5**, as illustrated in Table 2. Several different methods of solvation were used in the optimization of the transition states. Both implicitly solvated (IEFPCM) and explicitly solvated transition states are comparatively examined in this section.

As mentioned earlier, steric effects and the nature of the nucleophile determine the attack distance. The hindered aziridinium carbon atom (**C2**) is not easily approached by a nucleophile and the critical distances are expected to be longer for **path i**; this effect is more pronounced in the case of aziridinium ion **5** due to the larger ring size. For both aziridinium ions **1** and **5**, bond elongation percentages for the unhindered aziridinium carbon *P*(N–C3) are smaller than those for *P*(N–C2), indicating that in all cases regardless of the ring size and the nucleophile identity the hindered attack is always more distorting than its unhindered counterpart. When solvation effects are considered, implicitly solvated transition states often have higher bond elongation percentages than their explicit counterparts, indicating earlier TSs in the latter.

In the case of ring-expansion of bicyclic aziridinium ion **1** with an explicit solvent model, the critical distances between the incoming nucleophile and the S_N2 carbon are 2.28 and 2.35 Å for cyanide and chloride, respectively, for both paths **i** and **ii**. However, it is important to note that the extent to which the ring has opened in the chloride case (1.88 and 1.84 Å carbon-nitrogen distances for explicitly solvated **paths i** and **ii**, respectively) is indicative of a late and more 'product-like' transition state, which tends to lead to the thermodynamic product. Moreover, cyanide is shown to attack the aziridinium ring at shorter distances, leading to earlier, more 'reactant-like' transition state structures that typically lead to the kinetic product. For both bicyclic systems, azide is shown to attack at closer distances; moreover, with its higher bond-elongation values, a more "product-like" transition state is depicted. NH_2^- induces the lowest elongation along the nitrogen–carbon bond, by around 12–16% for each aziridinium carbon. This is a clear indication of the very early nature of the TS and the high reactivity of the nucleophile. In an effort to

Figure A.1. Article 1. (cont.)

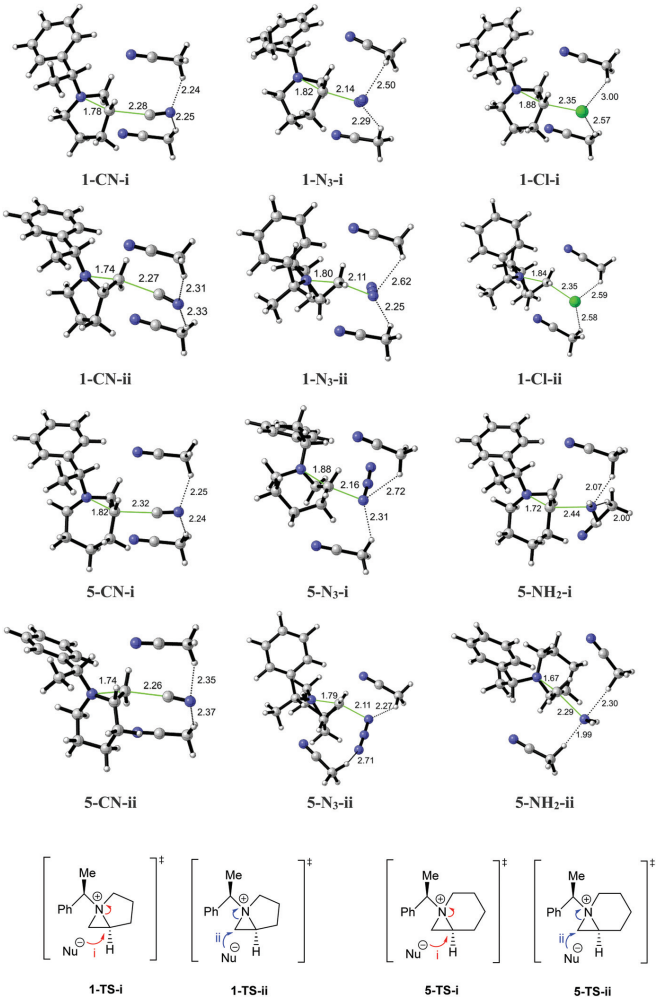

Fig. 1 Transition state structures of **path i** (hindered) and **path ii** (unhindered) for the ring opening of bicyclic aziridinium ions **1**[25] (top) and **5**[26] (bottom) with different nucleophiles (M06-2X/6-31+G(d,p); two explicit acetonitrile molecules; critical distances in Å).

pinpoint the consequences of the differential critical distances, the distortion–interaction model was utilized in the next sections.

Energetic analysis

The differences in Gibbs free energy of activation ($\Delta\Delta G^{\ddagger}$) between **paths i** and **ii** for the explicitly solvated ring-expansion of bicyclic aziridinium ions **1** and **5** are tabulated in Table 3. Energy refinements with IEFPCM were performed on the explicitly solvated reaction systems shown in Fig. 1 in order to assess the effect of a mixed implicit/explicit model. The results of the mixed solvation model were compared with explicitly solvated systems *in vacuo* as well as the implicitly solvated systems (Table 3). No significant difference in energetic trends was observed by the incorporation of the dielectric continuum on the explicitly solvated system. Henceforth, the study will use explicit–implicit models and exclude mixed solvation models.

Figure A.1. Article 1. (cont.)

Table 2 Transition state critical distances (Å) and bond elongation percentages of **path i** (hindered) and **path ii** (unhindered) for bicyclic aziridinium ions **1** and **5**[a,b,c,d,e] (M06-2X/6-31+G(d,p), 298 K and 1 atm)

			Path i (hindered)			**Path ii** (unhindered)		
		Azirid.	*d*(Nu–C2)	*d*(N–C2)	*P*(N–C2)[c,d,e] (%)	*d*(Nu–C3)	*d*(N–C3)	*P*(N–C3)[c,d,e] (%)
CN^-	Implicit	**1**	2.23	1.83	22.8	2.22	1.79	20.9
	Explicit	**1**	2.28	1.78	19.5	2.27	1.74	17.6
N_3^-	Implicit	**1**	2.11	1.86	24.8	2.08	1.82	23.0
	Explicit	**1**	2.14	1.82	22.1	2.11	1.80	21.6
Cl^-	Implicit	**1**	2.32	1.93	29.5	2.30	1.90	28.4
	Explicit	**1**	2.35	1.88	26.2	2.35	1.84	24.3
CN^-	Implicit	**5**	2.27	1.86	24.0	2.21	1.79	20.9
	Explicit	**5**	2.32	1.82	21.3	2.26	1.74	17.6
N_3^-	Implicit	**5**	2.13	1.90	26.7	2.08	1.83	23.6
	Explicit	**5**	2.16	1.88	25.3	2.11	1.79	20.9
NH_2	Implicit	**5**	2.39	1.74	16.0	2.36	1.66	12.2
	Explicit	**5**	2.44	1.72	14.7	2.29	1.67	12.8

[a] Implicit solvent model: IEFPCM in acetonitrile (ε = 35.688). [b] Explicit solvent model: two explicit acetonitrile molecules. [c] Bond elongation percentages $P(\text{N–C})$ (%) = $(d_{TS} - d_{reactant})/(d_{reactant}) \times 100$. [d] *d*(N–C2) = 1.49 Å, *d*(N–C3) = 1.48 Å from bicyclic aziridinium ion **1**. [e] *d*(N–C2) = 1.50 Å, *d*(N–C3) = 1.48 Å from bicyclic aziridinium ion **5**.

Table 3 Differences in Gibbs free energies of activation ($\Delta\Delta G^{\ddagger}$) for the ring-expansion of 1-azoniabicyclo[*n*.1.0]alkane **1** and **5** with different nucleophiles[a,b,c,d] (M06-2X/6-31+G(d,p), energies in kJ mol^{-1} at 298 K and 1 atm)

	$\Delta\Delta G^{\ddagger}$				
		Explicit[a]		Explicit/implicit[b,c]	
Nu	Aziridinium	**Path i** (hindered)	**Path ii** (unhindered)	**Path i** (hindered)	**Path ii** (unhindered)
CN^-	**1**	7.4	0.0	11.3	0.0
N_3^-	**1**	7.9	0.0	7.7	0.0
Cl^-	**1**	10.3	0.0	13.2	0.0
CN^-	**5**	11.4	0.0	13.9	0.0
N_3^-	**5**	3.5	0.0	4.2	0.0
NH_2^-	**5**	10.0	0.0	8.3	0.0

[a] Two explicit acetonitrile molecules. [b] Two explicit acetonitrile molecules. [c] Energy refinement with IEFPCM in acetonitrile (ε = 35.688). [d] All energies relative to the pre-reactive complex (PRC) of path **ii**.

When differences in barriers for the competing pathways are considered (Table 3), the unhindered route (**path ii**) is shown to be the kinetic path for both aziridinium **1** and **5**, as expected. These data would suggest that aziridinium ions **5** would yield piperidines **8** with all nucleophiles. Similarly, ring-opening of aziridinium ions **1** with all nucleophiles would result in the formation of pyrollidines **4**. However, this is not the experimental outcome and these data alone are not conclusive and only point toward the kinetically favored pathway, which is the unhindered route (**path ii**). In order to rationalize the experimental outcome, several factors, such as product stabilities, relative barrier heights for the reverse reactions, thermodynamic equilibration as well as the feasibility of the reactions under the experimental conditions, need to be considered for each case. A more detailed discussion of the free energy profiles is given in the following section.

Gibbs free energies of activation ($\Delta G^{\ddagger}$) and reaction (ΔG_{rxn}) for the ring opening of both bicyclic aziridinium ions **1** and **5** are reported in Table 4. Energy refinements with Grimme's dispersion correction scheme were implemented on B3LYP optimizations. In addition, optimizations with the dispersion-corrected GGA M06-2X are reported. Computed data in Table 4 reveal that activation barriers are consistently higher with the M06-2X functional for each system, possibly due to the extra stabilization of the reactants with dispersion effects. Moreover, barrier heights for implicitly solvated systems (IEFPCM, Table 4, and CPCM results in Table S1†) are higher than their explicit counterparts, since the reference points in these calculations are separate reactants as opposed to pre-reactive complexes in the latter explicitly solvated systems. Furthermore, implicit solvent models show almost identical results, indicating that the high-dielectric solvent, acetonitrile, is sufficiently mimicked by implicit models. It should be noted that due to their reference state (separate reactants), relative barriers attained through PCM calculations are less prone to conformational bias and as such, IEFPCM results will be used in the remainder of the discussion.

Figure A.1. Article 1. (cont.)

Table 4 Gibbs free energies of activation ($\Delta G^{\ddagger}$) and reaction (ΔG_{rxn}) [kJ mol^{-1}] for the ring opening of bicyclic aziridinium ions **1** and **5** with different nucleophiles (M06-2X/6-31+G(d,p), energies in kJ mol^{-1} at 298 K and 1 atm, IEFPCM in acetonitrile (ε = 35.688))

			B3LYP-D/6-31++G(d,p)[e]				M06-2X/6-31+G(d,p)				
		Nu	Path **i** $\Delta G^{\ddagger}$	Path **ii**	Path **i** ΔG_{rxn}	Path **ii**	Path **i** $\Delta G^{\ddagger}$	Path **ii**	Path **i** ΔG_{rxn}	Path **ii**	Exp[f]
Explicit solvent[a,b]	**1**	**CN**	28.5	19.7	−211.5	−204.8	37.7	30.3	−204.2	−201.1	0 : 100
	1	**N_3**	31.8	28.5	−123.4	−105.4	50.9	43.0	−127.0	−112.4	36 : 64
	1	**Cl**	27.9	21.8	−68.5	−50.7	51.3	41.1	−63.5	−46.5	100 : 0
	5	**CN**	32.7	23.8	−180.7	−193.3	49.6	38.2	−178.7	−196.8	8 : 92
	5	**N_3**	28.2	26.2	−92.0	−109.6	66.6	63.1	−79.2	−81.4	59 : 41
	5	**NH_2**	40.1	28.8	−250.1	−253.3	26.6	16.6	−286.4	−292.1	65 : 35
Implicit solvent (**IEFPCM**)[c,d]	**1**	**CN**	70.0	61.6	−151.4	−140.0	**89.6**	**77.4**	−150.2	−139.4	0 : 100
	1	**N_3**	59.5	58.4	−75.9	−57.0	**82.0**	**78.6**	−83.0	−63.7	36 : 64
	1	**Cl**	75.2	69.5	−1.5	15.0	**96.7**	**90.8**	−7.7	11.4	100 : 0
	5	**CN**	67.9	63.8	−127.0	−139.2	**90.5**	**78.2**	−124.3	−136.8	8 : 92
	5	**N_3**	59.1	59.8	−54.0	−57.6	**87.3**	**78.2**	−61.6	−62.8	59 : 41
	5	**NH_2**	38.2	31.0	−239.5	−242.0	**54.9**	**43.1**	−249.9	−252.5	65 : 35

[a] All energies relative to the pre-reactive complex (PRC) of path **ii**. [b] Optimizations with two explicit acetonitrile molecules in the gas phase. [c] All energies relative to the separate reactants. [d] Optimizations with IEFPCM in acetonitrile (ε = 35.688). [e] Energy refinement with DFT-D dispersion correction. [f] Experimental results: 3 : 4 for aziridinium **1** and 7 : 8 for aziridinium **5**.

It is important to note that differences in barrier heights consistently show the same trend, regardless of the level of theory or the type of solvation employed. This brings confidence in the predictive power of the calculations and will be useful in future experimental studies on similar systems. At all levels of theory and levels of solvation, the thermodynamic product for the ring-opening of bicyclic aziridinium ion **1** is piperidine **3**, obtained *via* the hindered **path i**. Similarly, in the case of aziridinium **5**, piperidine **8**, obtained *via* the unhindered **path ii**, is the thermodynamic product at all levels of theory and levels of solvation. Moreover, for both aziridinium ions **1** and **5**, the unhindered **path ii** is evidently the kinetically preferred route. Ultimately, the identity of the nucleophile determines the experimental outcome, and in some cases yields the kinetic and in other cases the thermodynamic products. The free energy profiles (Fig. 2) for each nucleophile reveal the rationale behind the experimentally observed outcomes.

Fig. 2 shows the Gibbs free energy profiles for both systems at the M06-2X/6-31+G(d,p) level of theory with IEFPCM solvation. The ring-expansion of aziridinium ion **1** with cyanide yields the kinetic products, pyrrolidines **4**. The rationale behind the unexpected experimental results is seen in the free energy profile in Fig. 2. The kinetic product **4** is formed through the smaller free energy barrier (**path ii**, **TS-ii**), owing to the high reverse barriers (~217 kJ mol^{-1}), thermodynamic equilibration is not feasible, and cyanide exclusively affords the kinetic product **4**, despite piperidines **3** being the thermodynamic product. In the case of the chloride ion, although the kinetic product forms initially, consistent with experimental outcome, the ring-expansion eventually affords the thermodynamic products, piperidines **3**, due to low reverse barriers (~100 kJ mol^{-1}) that enable thermodynamic equilibration. Moreover, for the chloride nucleophile the difference in stability of products **3** and **4** is consistently of the order of 17 kJ mol^{-1} in favor of piperidine **3**, regardless of the level of theory. This is perfectly aligned with the experimental outcome (100 : 0 for **3**/**4**). For the azide nucleophile, free energy barriers for both pathways seem equally feasible; however, due to high reverse barriers, equilibration is not expected. This is in line with the experimentally observed product ratios (36 : 64 for **3**/**4**) for the azide induced ring-expansion of aziridiniums **1**.

In the nucleophile-induced ring-expansions of aziridinium ions **5**, some similarities to aziridinium ions **1** are observed; particularly for cyanide, there is a clear preference for the unhindered pathway (**path ii**) and the reaction yields piperidines **8**, in line with the experimentally observed regioselectivities (8 : 92 for **7**/**8**). Incidentally, piperidines **8** is also the thermodynamic product in all ring-expansions of aziridinium ions **5**; therefore thermodynamic equilibration, when reverse barriers are feasible, would still favor piperidines **8** over azepanes **7**. Free energy profiles for the ring-expansion of aziridiniums **5** with amines depict very low barriers for both pathways (~50 kJ mol^{-1}), revealing the extremely reactive and, therefore, non-selective nature of the nucleophile. The barrier for the unhindered route (**path ii**) is ~10 kJ mol^{-1} lower, as expected; however, the overall barrier heights are too low to expect a kinetic outcome at room temperature and both pathways are deemed feasible. Consistent with the experimental outcome (65 : 35 for **7**/**8**), both azepanes **7** and piperidines **8** are expected to form from the ring-expansion of aziridiniums **5** with amines. Additionally, ring-expansions of aziridinium **5** with metal amines show the highest exothermicity among all the nucleophiles; hence, no thermal equilibration could be observed for these types of nucleophiles. These results indicate that although azepanes **7** are neither the kinetically favored

Figure A.1. Article 1. (cont.)

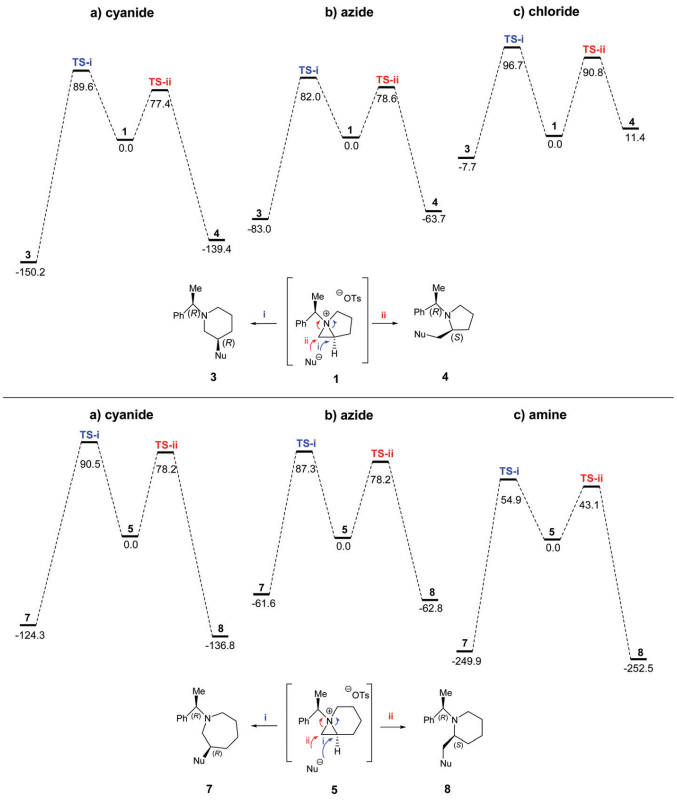

Fig. 2 Gibbs free energy profiles for the ring-expansion of 1-azoniabicyclo[*n*.1.0]alkane **1** (top) and **5** (bottom) with different nucleophiles.

product nor the thermodynamically favored product of aziridinium ion **5** ring-expansions, the formation of azepanes **7** is sufficiently feasible in the presence of very reactive nucleophiles, such as metal amines. In the case of the azide nucleophile, the experimental results (59 : 41 for **7**/**8**) indicate very slight preference for the formation of azepanes **7**. It is important to note that accurately reproducing an experimental product ratio of 59 : 41 is not within the feasible accuracy level of current computational methods. However, the observed product ratios could be rationalized by studying the free energy profiles, where azepanes **7** and piperidines **8** are almost isoenergetic (−61.6 kJ mol^{-1} and −62.8 kJ mol^{-1}, respectively). Contrary to the amine case, where the reverse barriers were of the order of ~300 kJ mol^{-1}, for the azide, reverse barriers are shown to be more feasible, enabling thermodynamic equilibration.

Computational findings were further extended by performing energy refinements (on both aziridinium systems with all nucleophiles) with kinetic functionals, BMK and MPW1K, well known to give accurate barrier heights (Table 5).[27,50,62] Once again the formation of the kinetic product for the cyanide-induced ring-expansion of bicyclic aziridinium **1** is confirmed through unfeasibly high reverse barriers for thermodynamic equilibration. Azide displays a similar preference for both attack sites in its reaction with aziridinium **1**, resulting in low regioselectivities. Ring-expansion products resulting from a chloride attack on aziridinium **1** undergo thermal equilibration to ultimately produce the thermodynamic products, piperidines **3**. The data resulting from kinetic functionals show that the barriers for amine-induced ring expansions of aziridinium **5** remain significantly lower than those for azide and cyanide, enabling the formation of both products. In the case of bicyclic aziridinium **5** with a cyanide nucleophile, the kinetic route is shown to be favored, and piperidines **8**, which are also the thermodynamic products, are formed. For the azide case, similar product stabilities and feasible back bar-

Figure A.1. Article 1. (cont.)

Table 5 Gibbs free energies of activation ($\Delta G^{\ddagger}$) and reaction (ΔG_{rxn}) [kJ mol^{-1}] for the ring opening of bicyclic aziridinium ions **1** and **5** with different nucleophiles[a,b]

		BMK/6-31+G(d,p)				MPW1 K/6-31+G(d,p)				
	Nu	Path **i** $\Delta G^{\ddagger}$	Path **ii**	Path **i** ΔG_{rxn}	Path **ii**	Path **i** $\Delta G^{\ddagger}$	Path **ii**	Path **i** ΔG_{rxn}	Path **ii**	Exp[c]
1	**CN**	87.3	75.2	−140.1	−131.2	93.0	82.5	−155.4	−147.8	0 : 100
1	**N_3**	85.3	81.4	−70.5	−53.8	93.0	90.6	−74.2	−59.7	36 : 64
1	**Cl**	94.8	88.5	0.5	17.1	99.7	96.0	−0.93	14.9	100 : 0
5	**CN**	87.5	77.6	−116.2	−128.3	94.1	85.3	−129.8	−143.3	8 : 92
5	**N_3**	91.1	82.5	−51.6	−52.8	99.2	92.2	−54.5	−57.1	59 : 41
5	**NH_2**	54.8	46.4	−248.2	−252.0	63.1	52.1	−252.0	−256.7	65 : 35

[a] Single-point (IEFPCM ε = 35.688) energies on M062X/6-31+G(d,p) IEFPCM (ε = 35.688) optimized structures. [b] All energies relative to the separate reactants. [c] Experimental results: 3 : 4 for aziridinium **1** and 7 : **8** for aziridinium **5**.

Table 6 Distortion energies for bicyclic aziridinium ions **1** and **5** in their ring-expansion reactions with different nucleophiles (M06-2X/6-31+G(d,p), energies in kJ mol^{-1} at 298 K and 1 atm, IEFPCM in acetonitrile (ε = 35.688))

		$\Delta E^{\ddagger}_{dist}$		$\Delta E^{\ddagger}_{int}$		
Nucleophile	Aziridinium	Path **i**	Path **ii**	Path **i**	Path **ii**	Exp[a]
CN^-	**1**	83.8	81.8	−32.3	−37.3	0 : 100
N_3^-	**1**	95.8	96.9	−52.0	−53.2	36 : 64
Cl^-	**1**	119.3	121.0	−49.1	−55.4	100 : 0
CN^-	**5**	98.1	88.7	−44.6	−48.5	8 : 92
N_3^-	**5**	103.7	102.8	−60.6	−64.5	59 : 41
NH_2^-	**5**	45.8	36.1	−33.3	−34.3	65 : 35

[a] Experimental results: 3 : 4 for substrate **1** and 7 : 8 for substrate **5**.

riers allowing thermal equilibration result in both regioisomers being formed.

Ring distortion energies

Previous studies on S_N2 reactions found that the central barrier of nucleophilic substitutions at an S_N2 type carbon is steric in nature, due to the pentavalent transition state.[63–65] This steric repulsion, which is destabilizing in nature, results in geometrical deformation, which requires a high distortion energy, ΔE_{dist}. In an effort to compare the difference in deformation caused by **paths i** and **ii**, distortion energies were calculated for both aziridinium ions in their ring-expansion reactions with different nucleophiles, as shown in Table 6. For bicyclic aziridinium ion **1**, no clear distinction between the two paths is observed. However, distortion energies are shown to increase in the order of cyanide, azide and chloride, in line with bond elongation percentages discussed earlier. Moreover, the cost of distorting the bicyclic aziridinium ions and forming a reorganized structure corresponding to the transition state is shown to increase as the nucleophile size increases. This is also consistent with the experimental outcome, as seen in the case of chloride with aziridinium ion **1**, which has highly product-like transition states, in comparison with cyanide and azide. Distortion energies reported for bicyclic aziridinium ion **5** are also in agreement with their bond elongation percentages; while azide has the highest, NH_2^- has the lowest values for distortion, consistent with the very early nature of its transition state. There is a noteworthy difference between distortion energies of paths **i** and **ii** for a cyanide attack on aziridinium ion **5**; an attack on the less hindered carbon has less distortion, verifying the experimental outcome.

Conclusion

Nucleophilic ring-expanson reactions of aziridinium ions **1** with cyanide, azide, and chloride and aziridinium ions **5** with cyanide, azide, and amine nucleophiles in acetonitrile have been investigated within a theoretical framework to understand the underlying factors for the experimental outcomes and to guide experimental efforts towards higher regioselectivities by rationalizing the influence of the nucleophile and the bicyclic aziridinium's ring size. A thorough analysis of the transition states was performed on both systems and both pathways; Gibbs free energy profiles were constructed with the inclusion of different solvation models as well as non-covalent interactions. Energetic analysis allowed the identification of kinetic and thermodynamic routes, which were further reinforced by studying the nature of the transition state struc-

Figure A.1. Article 1. (cont.)

tures, the variation of critical bonds, as well as the effects of distortion.

In terms of the computational methodologies employed, IEFPCM and CPCM optimizations yielded very similar results for each case. Activation barriers were shown to consistently increase with the M06-2X functional for each system, owing to the stabilization of the reactants. In the current study, the computed trends in regioselectivities were shown to be relatively robust across different levels of theory and the type of solvation method employed, allowing confident predictions through the calculated data. The thermodynamic product for bicyclic aziridinium ions **1** and **5** clearly appears to be piperidines **3** and piperidines **8**, respectively, at all levels of theory. For both aziridinium ions **1** and **5**, the unhindered **path ii** is shown to be the kinetically preferred route. However, the magnitude of the barrier heights for both pathways depends heavily on the nature of the nucleophile. Ultimately, a thorough investigation of the free energy profiles showed that the identity of the nucleophile determines the experimental outcome, and in some cases yields the kinetic and in other cases the thermodynamic products. Moreover, the current study helps predict the ways in which the desired regioselective outcomes could be induced in future experimental studies on similar systems. Particularly in the case of aziridinium ions **5**, ring-expansion products could be influenced by employing sterics on the bicyclic system and through a careful selection of the nucleophile's characteristics.

Conflicts of interest

There are no conflicts to declare.

Acknowledgements

The numerical calculations reported in this paper were partially performed at the TUBITAK ULAKBIM High Performance and Grid Computing Center (TRUBA resources) as well as at the computational resources at CCBG funded by the Bogazici University Research Fund (BAP-SUP project no. 8245).

References

1 A. K. Yudin, *Aziridines and Epoxides in Organic Synthesis*, Wiley-VCH Verlag GmbH & Co. KGaA, Weinheim, FRG, 2006.
2 M. K. Ghorai, A. Bhattacharyya, S. Das and N. Chauhan, in *Synthesis of 4- to 7-membered Heterocycles by Ring Expansion: Aza-, oxa- and thiaheterocyclic small-ring systems*, ed. M. D'hooghe and H.-J. Ha, Springer International Publishing, Cham, 2015, vol. 41, pp. 49–142.
3 B. Zwanenburg and P. ten Holte, in *Topics in Current Chemistry*, ed. P. Metz, Springer, Berlin, Heidelberg, 2001, vol. 216, pp. 93–124.
4 U. M. Lindström and P. Somfai, *Synthesis*, 1998, 109–117.
5 J. B. Sweeney, *Chem. Soc. Rev.*, 2002, **31**, 247–258.
6 X. E. Hu, *Tetrahedron*, 2004, **60**, 2701–2743.
7 S. Stanković, M. D'hooghe, S. Catak, H. Eum, M. Waroquier, V. Van Speybroeck, N. De Kimpe and H.-J. Ha, *Chem. Soc. Rev.*, 2012, **41**, 643–665.
8 D. Tanner, *Angew. Chem., Int. Ed. Engl.*, 1994, **33**, 599–619.
9 C. Schjoeth-Eskesen, P. R. Hansen, A. Kjaer and N. Gillings, *ChemistryOpen*, 2015, **4**, 65–71.
10 A. Bhattacharyya, C. V. Kavitha and M. K. Ghorai, *J. Org. Chem.*, 2016, **81**, 6433–6443.
11 H. Goossens, D. Hertsen, K. Mollet, S. Catak, M. D'hooghe, F. De Proft, P. Geerlings, N. De Kimpe, M. Waroquier and V. Van Speybroeck, in *Structure, Bonding and Reactivity of Heterocyclic Compounds*, ed. F. De Proft and P. Geerlings, Springer, Berlin, Heidelberg, 2014, vol. 38, pp. 1–34.
12 T. Ohwada, H. Hirao and A. Ogawa, *J. Org. Chem.*, 2004, **69**, 7486–7494.
13 M. D'hooghe, K. Vervisch, A. Van Nieuwenhove and N. De Kimpe, *Tetrahedron Lett.*, 2007, **48**, 1771–1774.
14 H. Goossens, K. Vervisch, S. Catak, S. Stanković, M. D'Hooghe, F. De Proft, P. Geerlings, N. De Kimpe, M. Waroquier and V. Van Speybroeck, *J. Org. Chem.*, 2011, **76**, 8698–8709.
15 H. Eum, J. Choi, C.-G. Cho and H.-J. Ha, *Asian J. Org. Chem.*, 2015, **4**, 1399–1409.
16 A. Padwa, in *Comprehensive Heterocyclic Chemistry III*, Elsevier, 2008, vol. 1, pp. 1–104.
17 H. S. Chong, H. A. Song, M. Dadwal, X. Sun, I. Sin and Y. Chen, *J. Org. Chem.*, 2010, **75**, 219–221.
18 T.-X. Métro, B. Duthion, D. Gomez Pardo and J. Cossy, *Chem. Soc. Rev.*, 2010, **39**, 89–102.
19 Y. Dong, H. Yun, C. S. Park, W. K. Lee and H. J. Ha, *Acta Crystallogr., Sect. C: Cryst. Struct. Commun.*, 2003, **59**, 659–660.
20 Y. Kim, H.-J. Ha, S. Y. Yun and W. K. Lee, *Chem. Commun.*, 2008, 4363–4365.
21 M. D'hooghe, V. Van Speybroeck, M. Waroquier and N. De Kimpe, *Chem. Commun.*, 2006, 1554–1556.
22 B. Anxionnat, B. Robert, P. George, G. Ricci, M. A. Perrin, D. Gomez Pardo and J. Cossy, *J. Org. Chem.*, 2012, **77**, 6087–6099.
23 M. Nonn, A. M. Remete, F. Fülöp and L. Kiss, *Tetrahedron*, 2017, **73**, 5461–5483.
24 J. Dolfen, N. N. Yadav, N. De Kimpe, M. D'hooghe and H. J. Ha, *Adv. Synth. Catal.*, 2016, **358**, 3485–3511.
25 M. K. Ji, D. Hertsen, D. H. Yoon, H. Eum, H. Goossens, M. Waroquier, V. Vanspeybroeck, M. D'Hooghe, N. Dekimpe and H. J. Ha, *Chem. – Asian J.*, 2014, **9**, 1060–1067.
26 J. Choi, N. N. Yadav and H. J. Ha, *Asian J. Org. Chem.*, 2017, **6**, 1292–1307.
27 S. Catak, M. D'Hooghe, N. De Kimpe, M. Waroquier and V. Van Speybroeck, *J. Org. Chem.*, 2010, **75**, 885–896.
28 Y. Lam, M. N. Grayson, M. C. Holland, A. Simon and K. N. Houk, *Acc. Chem. Res.*, 2016, **49**, 750–762.

Figure A.1. Article 1. (cont.)

29 L. A. Burns, Á. V. Mayagoitia, B. G. Sumpter and C. D. Sherrill, *J. Chem. Phys.*, 2011, **134**, 84107.
30 N. Marom, A. Tkatchenko, M. Rossi, V. V. Gobre, O. Hod, M. Scheffler and L. Kronik, *J. Chem. Theory Comput.*, 2011, **7**, 3944–3951.
31 G. A. Dilabio and A. Otero-de-la-Roza, in *Reviews in Computational Chemistry*, ed. A. L. Parrill and K. B. Lipkowitz, 2016, vol. 29, pp. 1–97.
32 A. Becke, *J. Chem. Phys.*, 1993, **98**, 5648–5652.
33 Y. Zhao and D. G. Truhlar, *Theor. Chem. Acc.*, 2008, **120**, 215–241.
34 S. Grimme, *J. Comput. Chem.*, 2006, **27**, 1787–1799.
35 S. Grimme, J. Antony, S. Ehrlich and H. Krieg, *J. Chem. Phys.*, 2010, **132**, 154104.
36 B. J. Lynch, P. L. Fast, M. Harris and D. G. Truhlar, *J. Phys. Chem. A*, 2000, **104**, 4811–4815.
37 A. D. Boese and J. M. L. Martin, *J. Chem. Phys.*, 2004, **121**, 3405–3416.
38 M. J. Frisch, G. W. Trucks, H. B. Schlegel, G. E. Scuseria, M. A. Robb, J. R. Cheeseman, G. Scalmani, V. Barone, B. Mennucci, G. A. Petersson, H. Nakatsuji, M. Caricato, X. Li, H. P. Hratchian, A. F. Izmaylov, J. Bloino, G. Zheng, J. L. Sonnenberg, M. Hada, M. Ehara, K. Toyota, R. Fukuda, J. Hasegawa, M. Ishida, T. Nakajima, Y. Honda, O. Kitao, H. Nakai, T. Vreven, J. A. Montgomery Jr., J. E. Peralta, F. Ogliaro, M. Bearpark, J. J. Heyd, E. Brothers, K. N. Kudin, V. N. Staroverov, T. Keith, R. Kobayashi, J. Normand, K. Raghavachari, A. Rendell, J. C. Burant, S. S. Iyengar, J. Tomasi, M. Cossi, N. Rega, J. M. Millam, M. Klene, J. E. Knox, J. B. Cross, V. Bakken, C. Adamo, J. Jaramillo, R. Gomperts, R. E. Stratmann, O. Yazyev, A. J. Austin, R. Cammi, C. Pomelli, J. W. Ochterski, R. L. Martin, K. Morokuma, V. G. Zakrzewski, G. A. Voth, P. Salvador, J. J. Dannenberg, S. Dapprich, A. D. Daniels, O. Farkas, J. B. Foresman, J. V. Ortiz, J. Cioslowski and D. J. Fox, *Gaussian 09 Revis. E.01*, 2010.
39 C. Gonzalez and H. B. Schlegel, *J. Chem. Phys.*, 1989, **90**, 2154–2161.
40 C. Gonzalez and H. B. Schlegel, *J. Phys. Chem.*, 1990, **94**, 5523–5527.
41 M. D'Hooghe, V. Van Speybroeck, A. Van Nieuwenhove, M. Waroquier and N. De Kimpe, *J. Org. Chem.*, 2007, **72**, 4733–4740.
42 S. Stanković, H. Goossens, S. Catak, M. Tezcan, M. Waroquier, V. Van Speybroeck, M. D'Hooghe and N. De Kimpe, *J. Org. Chem.*, 2012, **77**, 3181–3190.
43 V. Barone and M. Cossi, *J. Phys. Chem. A*, 1998, **102**, 1995–2001.
44 B. Mennucci, *Wiley Interdiscip. Rev.: Comput. Mol. Sci.*, 2012, **2**, 386–404.
45 A. Klamt, C. Moya and J. Palomar, *J. Chem. Theory Comput.*, 2015, **11**, 4220–4225.
46 Y. Takano and K. N. Houk, *J. Chem. Theory Comput.*, 2005, **1**, 70–77.
47 S. Catak, M. Dhooghe, T. Verstraelen, K. Hemelsoet, A. Van Nieuwenhove, H. J. Ha, M. Waroquier, N. De Kimpe and V. Van Speybroeck, *J. Org. Chem.*, 2010, **75**, 4530–4541.
48 M. D'Hooghe, S. Catak, S. Stankovic, M. Waroquier, Y. Kim, H. J. Ha, V. Van Speybroeck and N. De Kimpe, *Eur. J. Org. Chem.*, 2010, 4920–4931.
49 S. Stanković, S. Catak, M. D'Hooghe, H. Goossens, K. Abbaspour Tehrani, P. Bogaert, M. Waroquier, V. Van Speybroeck and N. De Kimpe, *J. Org. Chem.*, 2011, **76**, 2157–2167.
50 L. Hermosilla, S. Catak, V. Van Speybroeck, M. Waroquier, J. Vandenbergh, F. Motmans, P. Adriaensens, L. Lutsen, T. Cleij and D. Vanderzande, *Macromolecules*, 2010, **43**, 7424–7433.
51 C. P. Kelly, C. J. Cramer and D. G. Truhlar, *J. Phys. Chem. A*, 2006, **110**, 2493–2499.
52 J. R. Pliego and J. M. Riveros, *J. Phys. Chem. A*, 2001, **105**, 7241–7247.
53 E. F. Da Silva, H. F. Svendsen and K. M. Merz, *J. Phys. Chem. A*, 2009, **113**, 6404–6409.
54 W.-J. van Zeist and F. M. Bickelhaupt, *Org. Biomol. Chem.*, 2010, **8**, 3118.
55 I. Fernández and F. M. Bickelhaupt, *Chem. Soc. Rev.*, 2014, **43**, 4953–4967.
56 F. M. Bickelhaupt and K. N. Houk, *Angew. Chem., Int. Ed.*, 2017, **56**, 10070–10086.
57 S. Agopcan, N. Çelebi-Ölçüm, M. N. Üçışık, A. Sanyal and V. Aviyente, *Org. Biomol. Chem.*, 2011, **9**, 8079–8088.
58 A. G. Green, P. Liu, C. A. Merlic and K. N. Houk, *J. Am. Chem. Soc.*, 2014, **136**, 4575–4583.
59 S. M. Bronner, J. L. MacKey, K. N. Houk and N. K. Garg, *J. Am. Chem. Soc.*, 2012, **134**, 13966–13969.
60 F. Liu, R. S. Paton, S. Kim, Y. Liang and K. N. Houk, *J. Am. Chem. Soc.*, 2013, **135**, 15642–15649.
61 M. Walker, A. J. A. Harvey, A. Sen and C. E. H. Dessent, *J. Phys. Chem. A*, 2013, **117**, 12590–12600.
62 J. Dolfen, E. B. Boydas, V. Van Speybroeck, S. Catak, K. Van Hecke and M. D'hooghe, *J. Org. Chem.*, 2017, **82**, 10092–10109.
63 M. A. Van Bochove, M. Swart and F. M. Bickelhaupt, *ChemPhysChem*, 2007, **8**, 2452–2463.
64 A. P. Bento and F. M. Bickelhaupt, *J. Org. Chem.*, 2007, **72**, 2201–2207.
65 A. P. Bento and F. M. Bickelhaupt, *Chem. – Asian J.*, 2008, **3**, 1783–1792.

Figure A.1. Article 1. (cont.)

A.2. Probing Optical Properties of Thiophene Derivatives For Two Photon Absorption

A full-text version of the article regarding part II is given in this section.

Theor Chem Acc (2017) 136:67
DOI 10.1007/s00214-017-2094-y

REGULAR ARTICLE

Probing optical properties of thiophene derivatives for two-photon absorption

Ozlem Sengul[1] · Esma Birsen Boydas[1] · Mariachiara Pastore[2,3] · Walid Sharmouk[4] · Philippe C. Gros[5,6] · Saron Catak[1] · Antonio Monari[2,3]

Received: 25 January 2017 / Accepted: 18 April 2017 / Published online: 12 May 2017

Abstract We report a state-of-the-art characterization of the linear and nonlinear optical properties of two recent synthesized organic dyes based on the 2,5-dithienylpyrrole motifs. In particular after a careful conformational search was performed, the absorption spectra have been obtained at time-dependent density functional theory level taking into account vibrational and dynamical effects via a Wigner exploration of the potential energy surface. Furthermore, the excited state topology and electronic density reorganization have been characterized using natural transition orbitals and the charge transfer character quantified through recent developed descriptors, also allowing for the rationalization of the poor interfacial electron injection properties exhibited by the dyes when grafted on TiO_2 surfaces. Finally, two-photon absorption spectra have been calculated, extremely high cross sections have been obtained in the infrared region paving the way to the possible exploitation of the previous dyes for the development of photoactive smart materials or photodynamic therapy.

Keywords Two-photon absorption (TPA) · 2,5-Dithienylpyrrole (DTP) · Time-dependent density functional (TD-DFT) · Vibrational resolved spectra

1 Introduction

The impressive advancement in the control of light-induced function at the molecular level has triggered a spectacular development of light-active molecular materials covering a broad range of applications. As a non-exhaustive example, one can cite molecular photocatalysis [1–3], or smart materials based on light-triggered optical switch leading to molecular machines [4–6]. The latter development has most notably been awarded the Nobel Prize in Chemistry in 2016 [7]. Optically active compounds and dyes have also found successful applications in the field of solar energy conversion as light harvesting components in the dye-sensitized

Published as part of the special collection of articles derived from the 10th Congress on Electronic Structure: Principles and Applications (ESPA-2016).

Ozlem Sengul and Esma Birsen Boydas have contributed equally and have to be regarded as joint first authors.

Electronic supplementary material The online version of this article (doi:10.1007/s00214-017-2094-y) contains supplementary material, which is available to authorized users.

✉ Saron Catak
saron.catak@boun.edu.tr

✉ Antonio Monari
antonio.monari@univ-lorraine.fr

[1] Department of Chemistry, Bogazici University, Bebek, Istanbul 34342, Turkey

[2] Théorie-Modélisation-Simulation, SRSMC, Université de Lorraine – Nancy, Boulevard Des Aiguillettes, Vandoeuvre-lès-Nancy, Nancy, France

[3] Théorie-Modélisation-Simulation, SRSMC, CNRS, Boulevard Des Aiguillettes, Vandoeuvre-Lès-Nancy, Nancy, France

[4] Department of Inorganic Chemistry, National Research Centre, Dokki, Giza 12622, Egypt

[5] Hecrin SRSMC, Université de Lorraine – Nancy, Boulevard des Aiguillettes, Vandoeuvre-Lès-Nancy, Nancy, France

[6] Hecrin SRSMC, CNRS, Boulevard des Aiguillettes, Vandoeuvre-Lès-Nancy, Nancy, France

Figure A.2. Article 2.

solar cells (DSSCs) [8], developed in 1991 by Grätzel and O'Regan [9] and recently arrived to full commercialization.

Furthermore, dyes absorbing in the visible or infrared are also exploited for therapeutic purposes such as for instance the photodynamic therapy [10–13] used in antiviral [14], antimicrobial [15] and anticancer [16, 17] treatments. This strategy notably allows a significant reduction in the drug side effects by its specific spatial activation achieved through irradiation.

In order to increase the efficiency and the applicability of light-active materials and compounds, one should seek high intensity absorption at long wavelengths. Indeed, red or infrared light is much more penetrating than the shorter wavelengths, especially in biological tissues. In order to allow the treatment of lesions located deeper than the epidermis layer absorption in the so-called therapeutic window (600–800 nm) [18] is needed. In addition with red light photons, being less energetic, the possibility of collateral photodamages is strongly reduced.

Different strategies have been developed to allow for efficient red light absorption such as extended π-conjugation or the combination of π-bridged donor acceptor molecules (D-π-A). A promising alternative consists in the exploitation of nonlinear optical properties and particular two-photon absorption (TPA) phenomena [19–21]. If we consider irradiation by a monochromatic laser source, the energy needed by the photon to resonate with the chromophore and induce electronic transition will be half the excitation energy, as a consequence absorption wavelength will be doubled. Furthermore since TPA is a nonlinear phenomenon, the absorption probability will depend on the square of the light source intensity, in contrast to the linear dependence of one-photon absorption. Hence, absorption, and light activation, will be restricted only to the focal region of the laser source allowing for an optimal spatial resolution definitively desired in medical, or high technology, applications.

Different empirical or theoretical rules have been developed in the last years to rationalize the relationship between chromophores structure and TPA intensity (cross section). For instance, centrosymmetric molecules such as donor-π-acceptor-π-donor (D-π-A-π-D) [22] give generally high cross section for the $S_0 \rightarrow S_2$ transition. Polythiophenes structures have also been recognized as efficient TPA absorber [23] as confirmed both experimentally [24] and computationally [25].

In the past, we reported the synthesis and the characterization of two poly-thiophene-based dyes 2,5-dithienylpyrrole: DTP1 and DTP2 (Scheme 1; Fig. 1) [26]. The two D-π-A chromophore were designed to provide reasonable light-induced charge transfer to be exploited as DSSC sensitizers. The all-organic devices were assembled by TiO_2 sensitization and their performance measured, despite of good absorption properties and surface coverage, the produced photocurrent was relatively low, suggesting non-optimal interfacial electron separation and injection [26].

Taken into account the good optical properties of the DTP dyes, we perform an extensive state-of-the-art modeling investigation of their linear and nonlinear optical spectroscopy. This includes the sampling of their conformational space taking into account the dynamic and vibrational effects on the optical properties. As recently shown in a number of diverse applications [27–30], dynamic effects can be crucial especially in the case of large-scale low-frequency vibration, such as out-of-plane bending of conjugated rings. Moreover, such effects can be efficiently included by semiclassical molecular dynamics or hessian-based (Wigner) sampling of the ground state potential energy surface [25, 31]. The topological analysis of the excited states density reorganization, also performed via the use of newly developed charge transfer descriptors [32–34], allows for rationalizing the rather poor interfacial charge separation. In addition to the one-photon absorption, we also report the calculated TPA spectra, which show remarkably high cross sections in the infrared region, thus making our two dyes good candidates for nonlinear optical applications.

2 Computational methodology

A conformational analysis was performed on both dyes in order to obtain the most stable geometries. Hybrid B3LYP [35] and meta-hybrid GGA M06-2X [36] functionals were used for ground state optimizations. Both ground and excited states were calculated using the Gaussian09 [37]

Scheme 1 Chemical formula of the DTP1 and DTP2 molecules

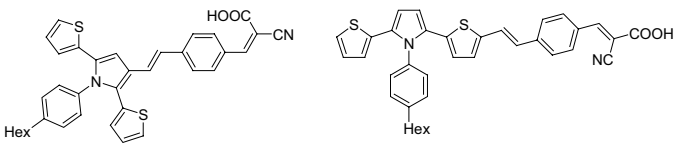

DTP1 DTP2

Figure A.2. Article 2. (cont.)

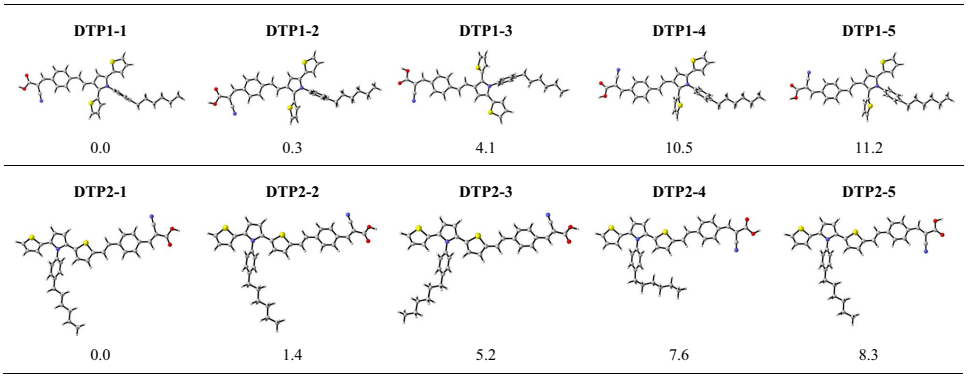

Fig. 1 Optimized structures (B3LYP/6-31G(d) with IEF-PCM in DCM) and relative Gibbs free energies (kJ/mol) for selected conformations of DTP1 and DTP2

software package. Long-range corrected hybrid functionals were used for vertical excitations, since they include the long-range exact Hartree–Fock [38] (HF) exchange which compensates for known limitations of DFT in the description of charge transfer states [39]. CAM-B3LYP [40] and ωB97XD [41] functionals and 6-31+G(d,p) basis set were used to model the excited states of the dyes. Solvent effects were taken into account using polarizable continuum method (IEF-PCM) [42, 43] in dichloromethane (DCM) both for conformation analysis and in the calculation of excitation energies.

To quantitatively characterize the charge transfer nature of the electronic excited states, the Φ_s index [32–34] is calculated for the target dyes. It mainly describes the overlap between the electron density in ground state and the rearranged electron density in excited state. When the value of Φs index is close to 1, a local transition can be postulated because of the high overlap between ground and excited state densities. On the other hand values close to 0, stem from a small overlap indicates a charge transfer character for the corresponding electronic transition. Φs and natural transition orbitals (NTO) [44] have been calculated with the Nancy_EX code [34].

To gain more insight into optical properties, dynamic and vibrational effects were included. A total of 20, 40 and 60 initial conditions were randomly sampled from the Wigner distribution [45] which is obtained as a quantum mechanical harmonic oscillator of the ground vibrational state, as implemented in the Newton-X [46] program. From all the chosen, Wigner conformation vertical transition energies were obtained using ωB97XD level of theory and 6-31+G(d,p) basis set. The initial conditions were generated using vibrational frequencies and normal mode vectors of the ground state optimized geometries (B3LYP/6-31G(d) level of theory) for absorption. To obtain a better representation of the spectrum, vertical transitions have been convoluted with Gaussian functions of fixed width at half length (FWHL) of 0.2 eV.

Two-photon absorption [47] (TPA) cross sections are calculated using the linear response formalism as implemented in DALTON2016 [48] program package. CAM-B3LYP/6-31G* level of theory is used. Cross section values are tabulated in Göppert-Mayer units (10^{-50} cm^4 photon^{-1}) in order to settle a direct comparison with the experiments. In addition, as for one-photon absorption dynamic effects on TPA have been estimated by Wigner distribution using 20 initial conditions.

3 Results and discussion

Structural and optical properties of two organic dyes, DTP1 and DTP2, were investigated to gain insight into their charge induction capabilities for use in dye-sensitized solar cells as well as their potential for use in nonlinear optical processes such as two-photon absorption (TPA), which is known to be enhanced by the presence of thiophene groups.

3.1 Conformational analysis of the ground state

To accurately assess the optical properties for both organic dyes, their conformational spaces were thoroughly scanned. A selection of the lowest energy conformers—within a free energy range of ~10 kJ/mol—was chosen for further analysis. Both functionals point to the same set of the lowest energy conformers, albeit some

Figure A.2. Article 2. (cont.)

minor differences in their relative free energies are found. B3LYP-optimized structures and relative free energies for the selected conformers of DTP1 and DTP2 are depicted in Fig. 1. The complete set of conformers and their relative energies (B3LYP and M06-2X) are given in Table S1 (in supporting info).

Conformers of DTP1 mainly show structural differences with respect to the positions of their cyano and carboxylate functionalities. While the isoenergetic **DTP1-1** and **DTP1-2** have these two groups facing opposite directions, the other three have them facing the same side, possibly leading to electronic repulsion and increasing their relative energies. For the isoenergetic conformations, the main structural differences stem from the positions of the relative orientation of the thiophene rings, which results in a 0.3 kJ/mol difference between the two conformations.

With the exception of **DTP2-5** presenting a trans-orientation, all the others conformers of DTP2 have the same conformation with respect to the cyano and carboxylate groups aforementioned. The energy difference between **DTP2-1**, **DTP2-2** and **DTP2-3** is mainly originated from the positions of the thiophene rings and the alignment of hexyl. The effect of hexane, for the **DTP2-2** and **DTP2-3** conformers, result in a 3.8 kJ/mol differences. This effect also can be seen for conformers **DTP2-4** and **DTP2-5**. Compared to DTP1, the position of hexyl group has a remarkable effect on the energy of DTP2. Indeed, the effect of the hexyl chain may be seen as a competition between enthropic factors and dispersion-driven attraction with the latter aspect favoring more compact structures; the analysis of the free energy differences provided in Fig. 1 unambiguously points toward the prevalence of enthropic disorder that is also enhanced by the fact that the disordered structures allows for a better solvent accessibility and hence a larger solvation stabilization.

3.2 Static level of theory assessment: functional performance

Absorption spectra were calculated for all optimized conformations of DTP1 and DTP2 depicted in Fig. 1. Table 1 collects the ωB97X-D and CAM-B3LYP values of λ_{max} in both nm and eV.

For both dyes, CAM-B3LYP λ_{max} values are red-shifted compared to ωB97X-D. Both functionals account for the non-Coulomb part of exchange functionals, however, ωB97X-D functional also includes an empirical atom–atom dispersion correction [41] which may partially account for the different trends in the static results. Also, when only a small charge separation is present, CAM-B3LYP may experience important deviations in reproducing excitation energies [49, 50]. The differences in the vertical transition energies are in the order of 10^{-2} eV, which further reinforces the use of ωB97XD as a functional quite suitable for reproducing absorption properties of these molecules.

The outcome of the static results are promising as the experimental values [26] was reproduced for almost each conformer. When the structures of the two organic dyes are compared, the extended conjugation in DTP2 is seen to cause the extension of the absorption toward the low-energy region of the spectrum, both experimentally and theoretically.

3.3 Excited state topologies and NTO's

Vertical transitions from each ground state conformer to their respective first excited (S_1) and second excited states (S_2) have been taken into account to model the charge transfer character. The Φ_s index, which describes the overlap between the electron density removed from the ground state (detachment density) and rearranged in the excited state (attachment density), was calculated to obtain a

Table 1 Benchmark calculations and experimental results [26] for absorption of DTP1 and DTP2 conformers

	λ_{ab} for DTP1				λ_{ab} for DTP2		
	ωB97X-D[a]	CAM-B3LYP[a]	Expt.		ωB97X-D[a]	CAM-B3LYP[a]	Expt.
DTP1-1	414 (2.99) 306 (4.05)	431 (2.87) 311 (3.98)	415 (2.98) 334 (3.71)	**DTP2-1**	458 (2.70) 291 (4.26)	479 (2.58) 316 (3.92)	457 (2.71) 364 (3.40)
DTP1-2	414 (2.99) 306 (4.05)	431 (2.87) 311 (3.98)		**DTP2-2**	458 (2.70) 292 (4.24)		
DTP1-3	415 (2.98) 305 (4.07)	431 (2.87) 310 (3.99)		**DTP2-3**	458 (2.70) 290 (4.27)	479 (2.58) 318 (3.89)	
DTP1-4	405 (3.06) 287 (4.32)	418 (2.96) 290 (4.27)		**DTP2-4**	457 (2.71) 291 (4.26)	478 (2.59) 316 (3.92)	
DTP1-5	405 (3.06) 287 (4.32)	419 (2.95) 290 (4.27)		**DTP2-5**	455 (2.72) 290 (4.27)	477 (2.60) 315 (3.93)	

λ_{max} values are given in nm (eV in parentheses)

[a] All vertical excitations were calculated on B3LYP/6-31G(d)-optimized geometries using 6-31+G(d,p) basis set and IEFPCM in DCM

Figure A.2. Article 2. (cont.)

quantitative measure for the ease of charge transfer upon photon absorption and gives an indirect assessment of the potential for charge injection in DSSC's. Φ_s values for DTP1 and DTP2, illustrated in Fig. 2, are close to 1, indicating a high level of overlap between the two aforementioned densities; hence, a local charge transfer, which deems them ineffective for use in solar cells. This also explains the low level of efficiency previously observed experimentally [26]. Furthermore, occupied and virtual NTOs, describing vertical transitions for $S_0 \rightarrow S_1$ and $S_0 \rightarrow S_2$, are depicted in Fig. 2. Consistent with the high Φ_s values obtained for both dyes, visual inspection of oNTO and vNTO's for each transition show an almost localized charge transfer.

3.4 Dynamic and vibrational effects on optical properties

As mentioned earlier, due to the extended conjugation in the chromophore systems under study herein, the dynamic and vibrational effects are expected to be significant. Hence, the ground state conformational space is explored using a Wigner distribution obtained from vibrational frequencies that were calculated for each conformer. To include dynamic effects, the initial conditions of 20, 40 and 60 structures were generated by sampling from a Wigner distribution as implemented in the Newton-X program. The spectra obtained from this distribution were compared with static calculations and experimental results.

As reported in Table 2, for both dye molecules, deviations from the corresponding experimental values can be noticed and all molecules have shown their λ_{max} in visible and near-UV region for absorption. Almost all of the chosen conformations are red-shifted when dynamic effects are present. Having 40 initial conditions results in some improvement when compared to 20 initials.

Conformation **2** shows blue shift in its $\lambda_{ab\text{-}20}$ and $\lambda_{ab\text{-}60}$ values for **DTP1**, even though 40 different coordinates and momenta produces a very strong red shift. This indicates that there is no direct correlation between the number of the initial conditions present in the Wigner procedure and the vertical excitation energy.

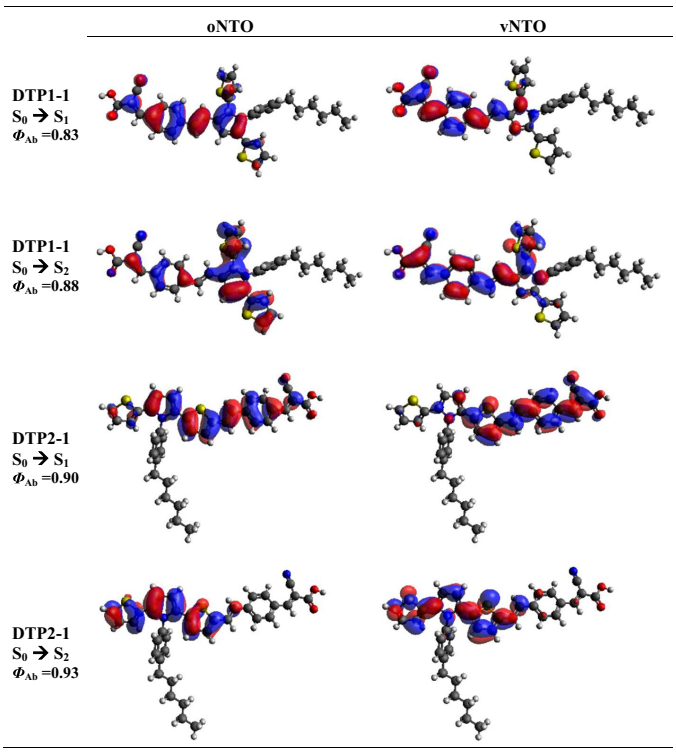

Fig. 2 Occupied and virtual NTO's for the lowest energy conformers of DTP1 and DTP2

Figure A.2. Article 2. (cont.)

Table 2 Wigner distribution results for absorption of DTP1 and DTP2 conformers, ωB97X-D/6-31+G(d,p)[a] calculated band maxima λ^{b}_{max} and experimental results

	$\lambda_{ab\text{-}20}$	$\lambda_{ab\text{-}40}$	$\lambda_{ab\text{-}60}$	λ^{c}_{ab}	$\lambda_{ab\text{-}Expt}$
DTP1-1	431 (2.87)	432 (2.87)	423 (2.93)	414 (2.99)	415 (2.98)
DTP1-2	406 (3.05)	448 (2.76)	408 (3.03)	414 (2.99)	
DTP1-3	443 (2.79)	445 (2.78)	425 (2.91)	415 (2.98)	
DTP1-4	385 (3.22)	420 (2.95)	421 (2.94)	405 (3.06)	
DTP1-5	392 (3.16)	423 (2.93)	427 (2.90)	405 (3.06)	
DTP2-1	446 (2.77)	483 (2.56)	476 (2.60)	458 (2.70)	457 (2.71)
DTP2-2	452 (2.74)	456 (2.71)	466 (2.66)	458 (2.70)	
DTP2-3	449 (2.76)	459 (2.70)	463 (2.67)	458 (2.70)	
DTP2-4	467 (2.65)	470 (2.63)	501 (2.47)	457 (2.71)	
DTP2-5	466 (2.66)	462 (2.68)	462 (2.68)	455 (2.72)	

[a] All vertical excitations were calculated on B3LYP/6-31G(d)-optimized geometries with IEFPCM in DCM

[b] λ_{max} values are given in nm (eV in parentheses)

[c] Static results from Table 1

When it comes to **DTP2**, one can immediately see that again most of the values are red-shifted. The lowest energy conformation **DTP2-1** gave absorption values within the 0.2 eV limit. For conformations **2, 3** and **4**, increasing number of the initial conditions extended the absorption toward the lower energy region, but a very large deviation is seen for conformation **4** in its $\lambda_{ab\text{-}60}$ value. When compared to the static TD-DFT calculations, a significant improvement cannot be observed in terms of λ_{max} values in the Wigner distribution results.

The final dynamic resolved spectra are obtained by convoluting the vertical excitations calculated for each snapshot. Figure 3 depicts the absorption spectra for the lowest energy conformers of DTP1 and DTP2 and nicely illustrate the convergence of the spectra. Absorption spectra for all conformers of DTP1 and DTP2 are given in SI.

To better reproduce the experimentally resolved band shape, 60 vertical transitions obtained from Wigner distribution for each conformer have been Boltzmann-weighted and subsequently convoluted with Gaussian functions.

Figure 4 shows Boltzmann-weighted Wigner distribution calculations for absorption spectra of DTP1 and DTP2, while the obtained absorption maxima are reported in Table 3. The value of the λ maxima compares quite well with the experimental ones [26] with differences of only 0.04 and 0.07 eV for DTP1 and DTP2, respectively. Also the general band shape, and in particular the evident shoulder in the case of DTP1, is nicely recovered evidencing the need of considering both conformational sampling and a proper treatment of vibrational effects.

3.5 Two-photon absorption

TPA is the result of simultaneous absorption of two photons of identical frequencies, since the total energy absorbed is doubled, the photons will populate electronic excited states having higher energy than in the case of one-photon absorption. Hence, TPA spectra will appear at much longer wavelengths, lower energy regions than conventional one-photon absorption.

Two-photon absorption cross sections are shown in Table 4 and Fig. 5 obtained from a Wigner distribution of the most stable conformer of the two molecules, respectively. Static TPA calculation for all the conformers are reported in supplementary information, notice that the difference in absorption maximum wavelengths

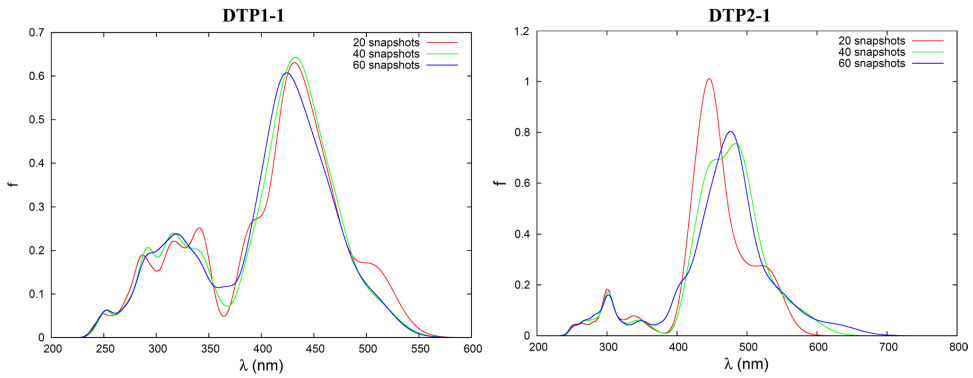

Fig. 3 Wigner distribution calculations for absorption spectra of the lowest energy conformations of DTP1 and DTP2

Figure A.2. Article 2. (cont.)

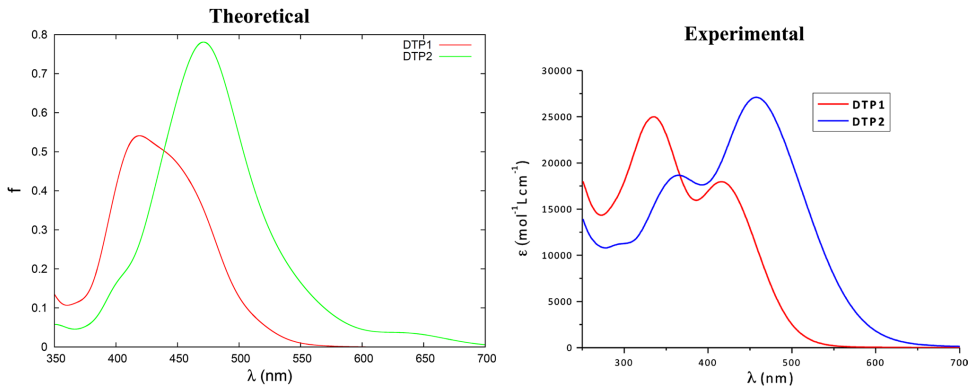

Fig. 4 Boltzmann-weighted Wigner distribution calculations for absorption spectra of DTP1 and DTP2 (*left panel*) and the corresponding experimental spectra (*right panel*)

Table 3 Absorption maxima from Boltzmann-weighted for DTP1 and DTP2

DTP1		DTP2	
λ_{ab} (nm)	Expt.	λ_{ab} (nm)	Expt.
418 (2.96)	415 (2.98)	470 (2.63)	457 (2.71)

Table 4 Calculated two-photon absorption cross sections and wavelengths via snapshots from Wigner distribution of DTP1 and DTP2 conformers

	DTP1			DTP2	
	λ_{Max} (nm)	Φ (GM)		λ_{Max} (nm)	Φ (GM)
DTP1-1	820	442.0	DTP2-1	870	742
	566	1243.6		624	6977.7

between the conformers never exceed 5 nm. As expected, both DTP1 and DTP2 absorb in the red to near infrared region, making them ideal candidates for optical applications requiring long wavelength excitations, in particular both DTP1 and DTP2 covers efficiently the therapeutic window allowing penetration in deep human tissues. As shown in Fig. 5, the $S_0 \rightarrow S_1$ absorption happens around 850 nm and gives rise to a broad symmetric band. Cross sections are of the order of 450 Göppert-Mayer (GM) for DTP1 while the larger conjugation of the polythiophene motifs in DTP2 increases the cross section up to 740 GM. The $S_0 \rightarrow S_2$ transition is also characterized by high TPA with maximum absorption at 566 nm for DTP1 and 624 nm for DTP2. Cross sections are extremely high exceeding 1000 GM for DTP1 and reaching the impressive value of 7000 GM for DTP2. The band relative to the second excited state is also more asymmetric and presents a wide tail extending to the red and infrared part of the spectrum. This is particularly significative for DTP1 since even if its $S_0 \rightarrow S_2$ absorption maximum falls outside the therapeutic windows cross section of the order of 400 GM can still be reached between 600 and 700 nm.

4 Conclusion

We report a state-of-the-art computational modeling study of the linear and nonlinear optical properties of two polythiophene organic dyes, DTP1 and DTP2. By performing a combination of conformational search and potential energy sampling through Wigner distribution, we have calculated the one-photon absorption spectra taking into account vibrational and conformational flexibility. Furthermore, we have analyzed the nature of the lowest lying excited states with a particular emphasis of their charge transfer nature. The photoinduced charge separation is quite modest as confirmed by the almost unitary value of the overlap between ground and excited state density matrices (Φ_s). This aspect can explain the previously observed moderate performance as DSSC sensitizers exhibited by the two dyes. On the contrary, remarkably high TPA cross section has been observed for DTP1 and especially DTP2, with absorption wavelengths in the red and infrared region of the spectrum both for $S_0 \rightarrow S_1$ and $S_0 \rightarrow S_2$ transitions. Hence, both dyes have to be regarded as extremely promising candidates for TPA sensitization in material science or biological and medical application.

Figure A.2. Article 2. (cont.)

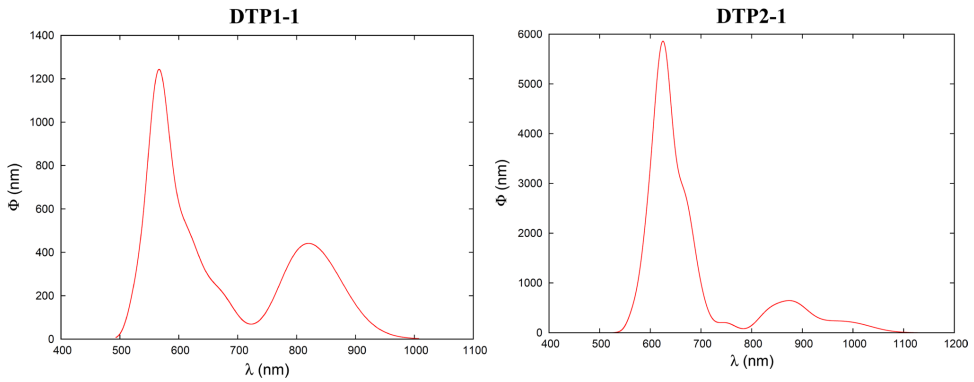

Fig. 5 Calculated TPA spectra using Wigner distribution for DTP1 and DTP2 chromophores

In the future, we plan to extend the study of the photophysical properties of both dyes in particular concerning the exploration of their singlet and triplet manifold both from a static point of view and via non-adiabatic state hopping dynamics to describe the time evolution of the different excited states.

Acknowledgements Support from the University of Lorraine and French CNRS is gratefully acknowledged. AM thanks Campus France for support under the bilateral "Bosphorus" 35649PL PHC program covering students mobility. SC acknowledges TUBITAK-PIA (Project No: 115Z863) for financial support.

References

1. Schultz DM, Yoon TP (2014) Solar synthesis: prospects in visible light photocatalysis. Science 343:1239176-1–1239176-8
2. Berardi S, Drouet S, Francàs L et al (2014) Molecular artificial photosynthesis. Chem Soc Rev 43:7501–7519
3. Frischmann PD, Mahata K, Würthner F et al (2013) Powering the future of molecular artificial photosynthesis with light-harvesting metallosupramolecular dye assemblies. Chem Soc Rev 42:1847–1870
4. Colasson B, Credi A, Ragazzon G (2016) Light-driven molecular machines based on ruthenium (II) polypyridine complexes: strategies and recent advances. Coord Chem Rev 325:125–134
5. Browne WR, Feringa BL (2006) Making molecular machines work. Nat Nanotechnol 1:25–35
6. Astumian RD, Mukherjee S, Warshel A (2016) The physics and physical chemistry of molecular machines. Chemphyschem 17:1719–1741
7. Le Bailly B (2016) Nobel prize in chemistry: welcome to the machine. Nat Nanotechnol 11:923
8. Hagfeldt A, Boschloo G, Sun L et al (2010) Dye-sensitized solar cells. Chem Rev 110:6595–6663
9. O'Regan B, Grätzel M (1991) A low-cost, high-efficiency solar cell based on dye-sensitized colloidal TiO_2 films. Nature 353:737–740
10. Bonnett R (1995) Photosensitizers of the porphyrin and phthalocyanine series for photodynamic therapy. Chem Soc Rev 24:19–33
11. Pandey RK (2000) Recent advances in photodynamic therapy. J Porphyr Phthalocyanines 4:368–373
12. Yuan Q, Wu Y, Wang J et al (2013) Targeted bioimaging and photodynamic therapy nanoplatform using an aptamer-guided G-quadruplex DNA carrier and near-infrared light. Angew Chem Int Ed 52:13965–13969
13. Babilas P, Landthaler M, Szeimies R-M (2006) Photodynamic therapy in dermatology. Eur J Dermatol 16:340–348
14. Winkler K, Simon C, Finke M et al (2016) Photodynamic inactivation of multidrug-resistant *Staphylococcus aureus* by chlorin e6 and red light ($\lambda = 670$ nm). J Photochem Photobiol B Biol 162:340–347
15. Koshi E, Mohan A, Rajesh S, Philip K (2011) Antimicrobial photodynamic therapy: an overview. J Indian Soc Periodontol 15:323
16. Allison RR, Moghissi K (2013) Oncologic photodynamic therapy: clinical strategies that modulate mechanisms of action. Photodiagnosis Photodyn Ther 10:331–341
17. Allison RR, Sibata CH (2010) Oncologic photodynamic therapy photosensitizers: a clinical review. Photodiagnosis Photodyn Ther 7:61–75
18. Tsai C-L, Chen J-C, Wang W-J (2001) Near-infrared absorption property of biological soft tissue constituents. J Med Biol Eng 21:7–14
19. Zhou H, Zhou F, Tang S et al (2012) Two-photon absorption dyes with thiophene as π electron bridge: synthesis, photophysical properties and optical data storage. Dye Pigment 92:633–641
20. Zou Q, Zhao H, Zhao Y et al (2015) Effective two-photon excited photodynamic therapy of xenograft tumors sensitized by water-soluble bis(arylidene) cycloalkanone photosensitizers. J Med Chem 58:7949–7958
21. Zheng Y-C, Zheng M-L, Li K et al (2015) Novel carbazole-based two-photon photosensitizer for efficient DNA photocleavage in anaerobic condition using near-infrared light. RSC Adv 5:770–774
22. Abbotto A, Beverina L, Bozio R et al (2002) Novel heterocycle-based two-photon absorbing dyes. Org Lett 4(9):1495–1498

Figure A.2. Article 2. (cont.)

23. Soos ZG, Galvao DS (1994) One- and two-photon excitations of polythiophene: role of nonconjugated heteroatoms. J Phys Chem 98:1029–1033
24. Huang P-H, Shen J-Y, Pu S-C et al (2006) Synthesis and characterization of new fluorescent two-photon absorption chromophores. J Mater Chem 16:850–857
25. Turan HT, Eken Y, Marazzi M et al (2016) Assessing one- and two-photon optical properties of boron containing arenes. J Phys Chem C 120:17916–17926
26. Sharmoukh W, Attanzio A, Busatto E et al (2015) 2,5-Dithienylpyrrole (DTP) as a donor component in DTP-π-A organic sensitizers: photophysical and photovoltaic properties. RSC Adv 5:4041–4050
27. Chantzis A, Very T, Monari A, Assfeld X (2012) Improved treatment of surrounding effects: UV/Vis absorption properties of a solvated Ru(II) complex. J Chem Theory Comput 8:1536–1541
28. Etienne T, Very T, Perpète EA et al (2013) A QM/MM study of the absorption spectrum of harmane in water solution and interacting with DNA: the crucial role of dynamic effects. J Phys Chem B 117:4973–4980
29. Gattuso H, Dumont E, Marazzi M, Monari A (2016) Two-photon-absorption DNA sensitization via solvated electrons production: unraveling the photochemical pathways by molecular modeling and simulation. Phys Chem Chem Phys 18:18598–18606
30. Gattuso H, Assfeld X, Monari A (2015) Modeling DNA electronic circular dichroism by QM/MM methods and Frenkel Hamiltonian. Theor Chem Acc 134:225–232
31. Marazzi M, Gattuso H, Monari A (2016) Nile blue and Nile red optical properties predicted by TD-DFT and CASPT2 methods: static and dynamic solvent effects. Theor Chem Acc 135:57
32. Etienne T (2015) Probing the locality of excited states with linear algebra. J Chem Theory Comput 11:1692–1699. doi:10.1021/ct501163b
33. Etienne T, Assfeld X, Monari A (2014) New insight into the topology of excited states through detachment/attachment density matrices-based centroids of charge. J Chem Theory Comput 10:3906–3914
34. Etienne T, Assfeld X, Monari A (2014) Toward a quantitative assessment of electronic transitions charge-transfer character. J Chem Theory Comput 10:3896–3905
35. Becke A (1993) B3LYP. J Chem Phys 98:5648–5652
36. Zhao Y, Truhlar DG (2008) The M06 suite of density functionals for main group thermochemistry, thermochemical kinetics, noncovalent interactions, excited states, and transition elements: two new functionals and systematic testing of four M06-class functionals and 12 other function. Theor Chem Acc 120:215–241
37. Frisch MJ, Trucks GW, Schlegel HB, Scuseria GE, Robb MA, Cheeseman JR, Scalmani G, Barone V, Mennucci B, Petersson GA, Nakatsuji H, Caricato M, Li X, Hratchian HP, Izmaylov AF, Bloino J, Zheng G, Sonnenber DJ (2009) Gaussian 09. Revision D.01, Inc, Wallingford CT
38. Slater JC (1951) A simplification of the Hartree-Fock method. Phys Rev 81:385–390
39. Chai JD, Head-Gordon M (2008) Systematic optimization of long-range corrected hybrid density functionals. J Chem Phys 128(8):084106-1–084106-15
40. Yanai T, Tew DP, Handy NC (2004) A new hybrid exchange-correlation functional using the Coulomb-attenuating method (CAM-B3LYP). Chem Phys Lett 393:51–57
41. Chai J-D, Head-Gordon M (2008) Long-range corrected hybrid density functionals with damped atom–atom dispersion corrections. Phys Chem Chem Phys 10:6615
42. Mennucci B (2012) Polarizable continuum model. Wiley Interdiscip Rev Comput Mol Sci 2:386–404
43. Tomasi J, Mennucci B, Cancès E (1999) The IEF version of the PCM solvation method: an overview of a new method addressed to study molecular solutes at the QM ab initio level. J Mol Struct 464:211–226
44. Martin RL (2003) Natural transition orbitals. J Chem Phys 118:4775–4777
45. Dahl JP, Springborg M (1988) The Morse oscillator in position space, momentum space, and phase space. J Chem Phys 88:4535
46. Barbatti M, Ruckenbauer M, Plasser F et al (2014) Newton-X: a surface-hopping program for nonadiabatic molecular dynamics. Wiley Interdiscip Rev Comput Mol Sci 4:26–33
47. Pawlicki M, Collins HA, Denning RG, Anderson HL (2009) Two-photon absorption and the design of two-photon dyes. Angew Chemie-Int Ed 48:3244–3266
48. Aidas K, Angeli C, Bak KL et al (2014) The Dalton quantum chemistry program system. Wiley Interdiscip Rev Comput Mol Sci 4:269–284
49. Peach MJG, Benfield P, Helgaker T, Tozer DJ (2008) Excitation energies in density functional theory: an evaluation and a diagnostic test. J Chem Phys 128:044118–(1–8)
50. Jacquemin D, Wathelet V, Perpète EA, Adamo C (2009) Extensive TD-DFT benchmark: singlet-excited states of organic molecules. J Chem Theory Comput 5:2420–2435

Figure A.2. Article 2. (cont.)

APPENDIX B: PROJECTED DENSITY OF STATES

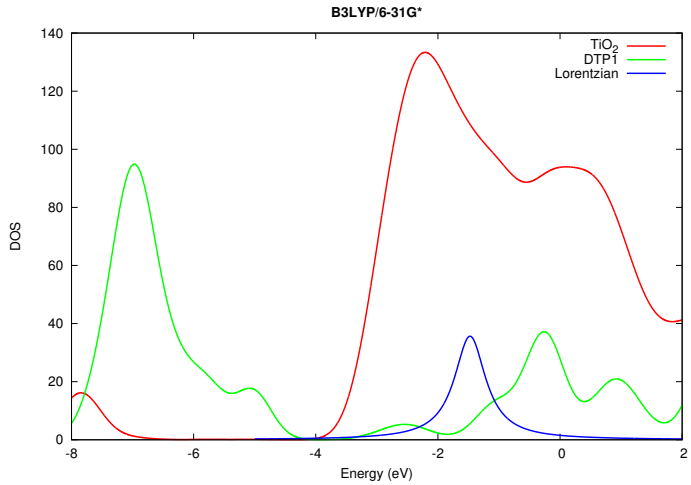

Figure B.1. Projected Density of States plot for DTP1, optimized in gas phase. (Mulliken orbitals were extracted at B3LYP/6-31G* level of theory and IEF-PCM in dichloromethane.)

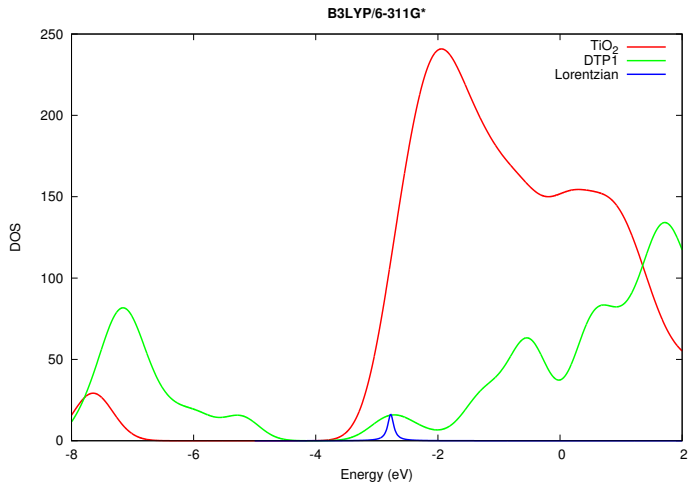

Figure B.2. Projected Density of States plot for DTP1, optimized in gas phase. (Mulliken orbitals were extracted at B3LYP/6-311G* level of theory and IEF-PCM in dichloromethane.

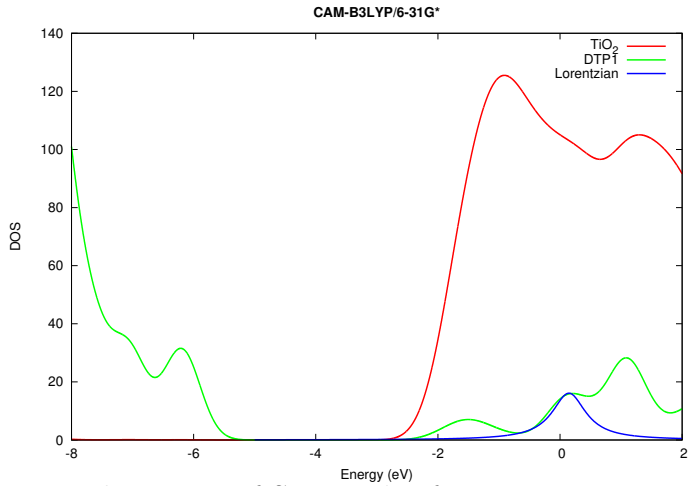

Figure B.3. Projected Density of States plot for DTP1, optimized in gas phase. (Mulliken orbitals were extracted at CAM-B3LYP/6-31G* level of theory and IEF-PCM in dichloromethane.

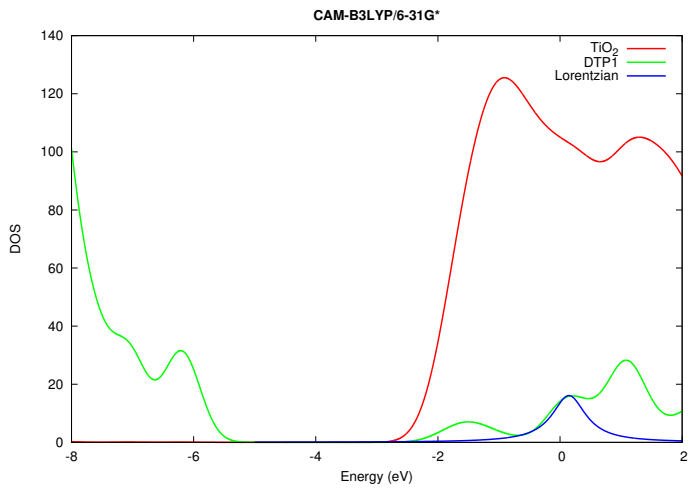

Figure B.4. Projected Density of States plot for DTP1, optimized in gas phase. (Mulliken orbitals were extracted at CAM-B3LYP/6-311G* level of theory and IEF-PCM in dichloromethane.

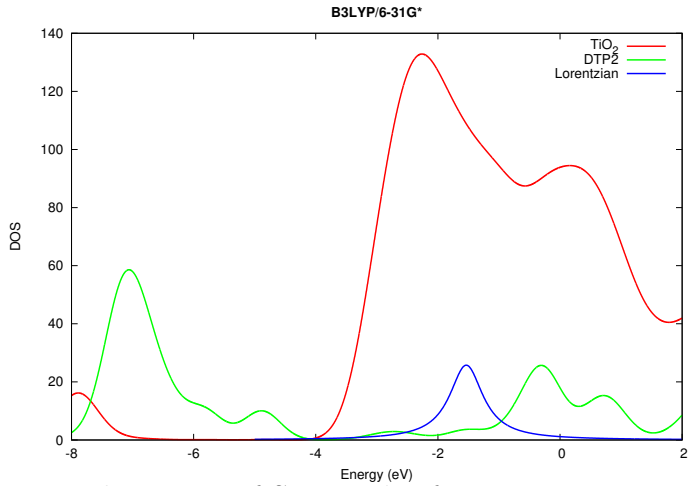

Figure B.5. Projected Density of States plot for DTP2, optimized in gas phase. (Mulliken orbitals were extracted at B3LYP/6-31G* level of theory and IEF-PCM in dichloromethane.

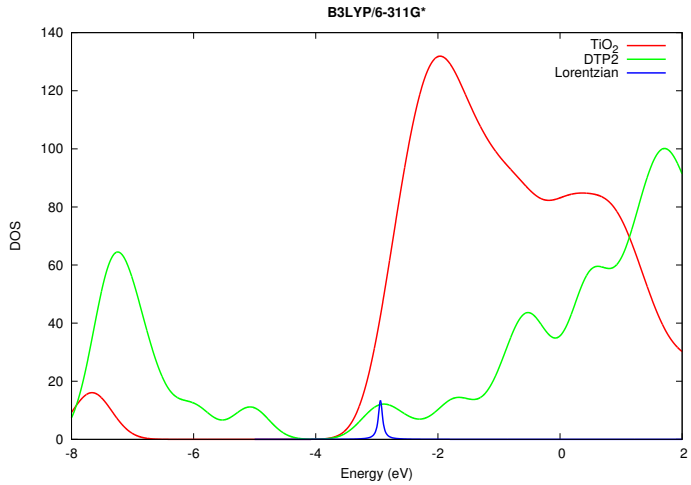

Figure B.6. Projected Density of States plot for DTP2, optimized in gas phase. (Mulliken orbitals were extracted at B3LYP/6-311G* level of theory and IEF-PCM in dichloromethane.

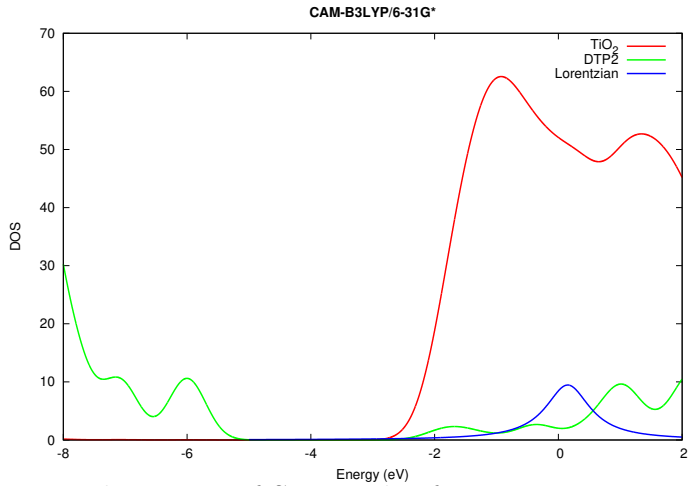

Figure B.7. Projected Density of States plot for DTP2, optimized in gas phase. (Mulliken orbitals were extracted at CAM-B3LYP/6-31G* level of theory and IEF-PCM in dichloromethane.

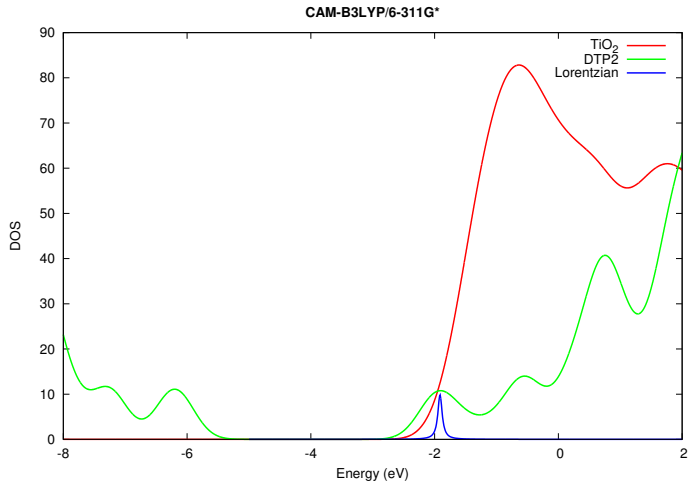

Figure B.8. Projected Density of States plot for DTP2, optimized in gas phase. (Mulliken orbitals were extracted at CAM-B3LYP/6-311G* level of theory and IEF-PCM in dichloromethane.

APPENDIX C: ISODENSITY SURFACE PLOTS

Table C.1. Isodensity surface plots of Mulliken HOMO and LUMO orbitals of standalone dyes and dye@semiconductor interfaces.(Optimizations were held in PBE-D3/DZP in gas phase, Mulliken orbitals were extracted at B3LYP/**6-31G*** level of theory, IEF-PCM in dichloromethane)

	$\mathbf{Dye_{HOMO}}$	$\mathbf{Dye@SC_{HOMO}}$	$\mathbf{Dye_{LUMO}}$	$\mathbf{Dye@SC_{LUMO}}$
DTP1	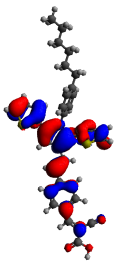	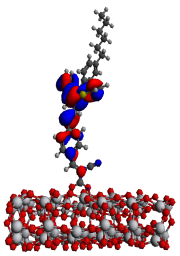	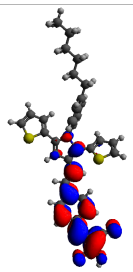	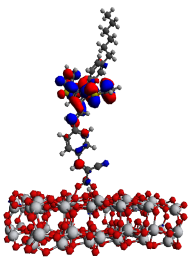
DTP2	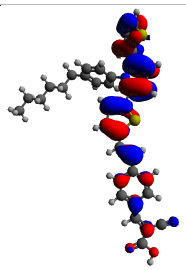	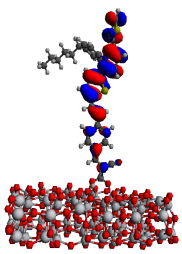	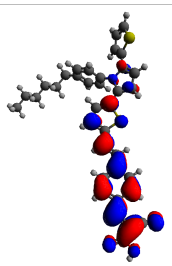	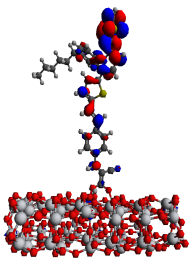

APPENDIX D: DFT VERSUS DFT-D3

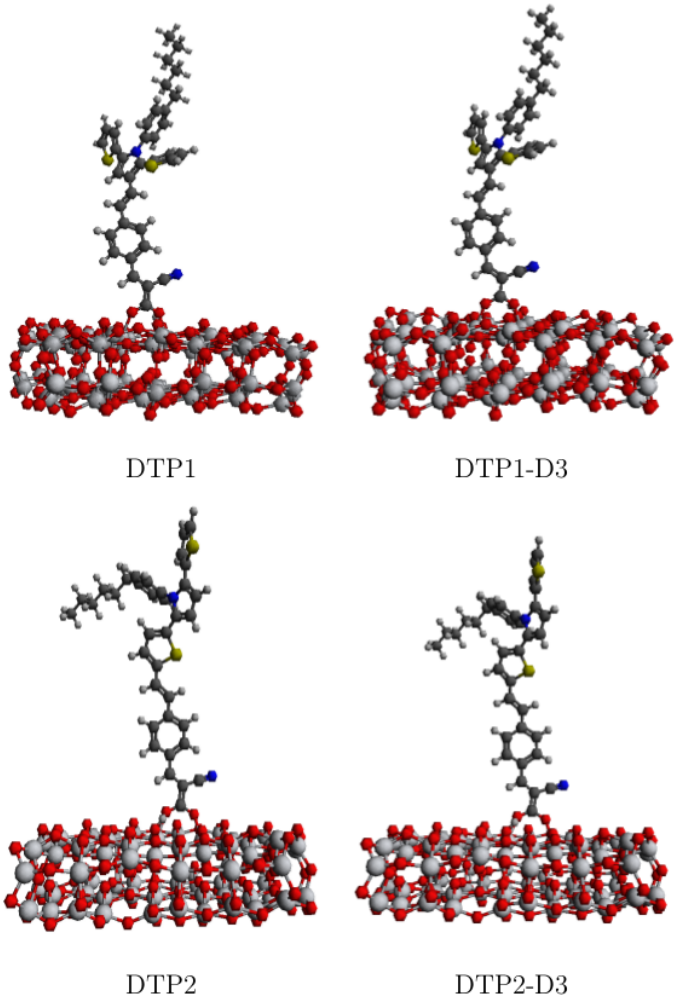

Figure D.1. Gas phase adsorption geometries of DTP1 and DTP2 with and without inclusion of DFT-D3 dispersion corrections.